Bioimpedance Sensors: A Tutorial

Panagiotis Kassanos, *Senior Member, IEEE*

***Abstract*—Electrical bioimpedance entails the measurement of the electrical properties of tissues as a function of frequency. It is thus a spectroscopic technique. It has been applied in a plethora of biomedical applications for diagnostic and monitoring purposes. In this tutorial, the basics of electrical bioimpedance sensor design will be discussed. The electrode/electrolyte interface is thoroughly described, as well as methods for its modelling with equivalent circuits and computational tools. The design optimization and modelling of bipolar and tetrapolar bioimpedance sensors is presented in detail, based on the sensitivity theorem. Analytical and numerical modelling approaches for electric field simulations based on conformal mapping, point electrode approximations and the finite element method (FEM) are also elaborated. Finally, current trends on bioimpedance sensors are discussed followed by an overview of instrumentation methods for bioimpedance measurements, covering aspects of voltage signal excitations, current sources, voltage measurement front-end topologies and methods for computing the electrical impedance.**

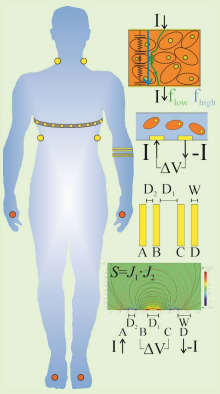

***Index Terms*—Bipolar impedance sensor, electrical bioimpedance, instrumentation, tetrapolar impedance sensor, tissue impedance.**

I. Introduction

ELECTRICAL bioimpedance is a technique that has been applied in a wide range of biomedical applications for detection of pathologies and adverse physiological events and for the monitoring of physiological processes and tissue dynamics. Bioimpedance is used to evaluate skin hydration [1], [2], to differentiate healthy from cancerous tissue [3], to assess heart and lung function [4], for detecting tissue ischemia [5]–[7], in full body or segment composition analysis [8], for imaging different parts of the body [9], [10], for monitoring wound healing and oedema [11] and for the assessment of muscle health in neuromuscular diseases [12]–[14]. Bioimpedance sensors can also be integrated into catheters for *in situ* tissue analysis during surgical procedures and have thus great potential in (soft) robotic surgical tools and surgery [15]–[17]. At the smaller scale it is used for measuring, analyzing, and imaging individual cells, cell cultures and suspensions [18]–[20], as well as in electroporation studies [21]. This is only an indicative list of popular applications for bioimpedance. Detailed discussions of these and other applications can be found in the supplementary information (SI) of this paper.

Bioimpedance is increasingly used in the bioengineering field, with the bioimpedance community continuously growing and with many commercial products appearing in the market in recent years. At a first glance, it seems as a relatively simple method, as in its essence, it is a purely electrical technique. After all, bioimpedance is Ohm's law. As it will be discussed in more detail in subsequent sections, bioimpedance involves the measurement of the electrical properties of tissues and cell populations from a few Hz to a few MHz. One or more frequencies may be of interest depending on the application. Based on whether dynamic properties are studied, the bioimpedance can be measured sequentially one frequency at a time, or in a multifrequency approach to measure all frequencies of interest simultaneously. Since impedance is measured at a range of frequencies, it is a spectroscopic technique, giving rise to the term bioimpedance spectroscopy.

To measure bioimpedance, a known signal must be applied to the tissue, as opposed to electrophysiological signals that only require voltage recordings. Consequently, the instrumentation required is somewhat more complicated

Manuscript received August 14, 2021; accepted August 20, 2021. Date of publication September 3, 2021; date of current version October 18, 2021. This work was supported by the U.K. Engineering and Physical Science Research Council (EPSRC), in part by the Micro-Robotics for Surgery Project under Grant EP/P012779/1, and in part by the Future AI and Robotics Hub for Space (FAIR-SPACE) Project under Grant EP/R026092/1. The associate editor coordinating the review of this article and approving it for publication was Dr. Marios Sophocleous.

The author is with The Hamlyn Centre, Institute of Global Health Innovation, Imperial College London, London SW7 2AZ, U.K. (e-mail: p.kassanos@imperial.ac.uk).

This article has supplementary downloadable material available at https://doi.org/10.1109/JSEN.2021.3110283, provided by the authors.

Digital Object Identifier 10.1109/JSEN.2021.3110283

as a signal needs to be generated to excite the biosample to then obtain its required electrical properties as a function of applied signal frequency. This signal needs to be known and, in most cases, it is kept constant, such that there is only one measurand needed to calculate the impedance using Ohm's law. Otherwise, both the voltage and current need to be measured. Similarly to obtaining electrophysiological signals, simple electrodes can be used to provide an electrical contact to tissues. Thus, as opposed to electrochemical sensors, there is no need for specialized membranes, enzymes, antibodies or other molecules to be deposited on electrode surfaces. In fact, in many bioimpedance applications, electrocardiography electrodes are often used. Nevertheless, in many applications it is important to optimize the electrode design to control the impedimetric properties of the electrode system employed. In addition, various materials can be deposited on the electrode surface to improve its interfacial impedance properties.

This tutorial paper provides holistic discussions on all matters necessary for the design of bioimpedance sensors and an overview of bioimpedance instrumentation. First the electrical properties of tissues, the electrode interface impedance, its modelling and electrode characterization are discussed, followed by an overview of methods for reducing electrode interface impedance. Two- (bipolar) and four-electrode (tetrapolar) systems for the measurement of bioimpedance are discussed, elaborating on the electric field properties of coplanar parallel electrode systems, their optimization and modelling. Electrodes only provide the interface to the biosamples and instrumentation considerations, are also discussed for completeness. A conclusion ends the paper. An overview of popular bioimpedance applications and the derivation and detailed discussion of various theorems and equations can be found in the SI.

II. Electrical Properties of Biological Matter

It is important first to understand the fundamentals of the electrical properties of biosamples. According to Ohm's law, impedance (Z) is frequency dependent and equal to the complex ratio of the ac voltage (V) over the current (I):

$$Z(f) = \frac{1}{Y(f)} = \frac{V_o sin(2\pi f t + \varphi)}{I_o sin(2\pi f t)} = Re(Z) + jIm(Z)$$
$$= R + jX = |Z| e^{jarg(Z)} = |Z| e^{jartan\left(\frac{Im(Z)}{Re(Z)}\right)}. \quad (1)$$

I_o and V_o are the injected current and recorded voltage signal amplitudes, respectively, t is time, φ is the phase difference between current and voltage (positive or negative, depending if an inductive or capacitive, respectively, behavior dominates), Y is the admittance, Re(Z) is the real part of the impedance, which is the resistance (R) and Im(Z) is the imaginary part of the impedance, known as the reactance (X), $|Z|$ is the magnitude of the impedance, arg(Z) gives φ, and the angular frequency is $\omega = 2\pi f$. As is obvious, impedance can be described either by a magnitude and phase or equivalently by the real and imaginary parts of the impedance. These are illustrated in Fig. 1(a) and (b).

Every material can be characterized by a conductivity, σ, and a relative permittivity, ε_r (Fig. 1(c)). Thus, they can be

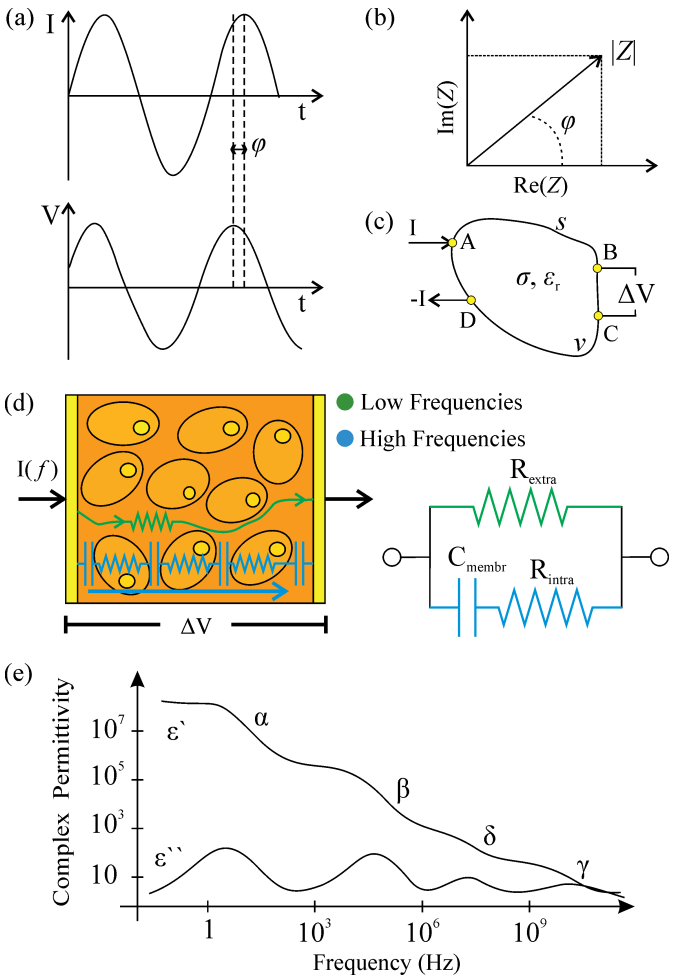

Fig. 1. (a) The injected current sine wave and the resultant measured voltage waveform, phase delayed due to the impedance. (b) Phasor diagram representation of the impedance. (c) Injection of a known current through electrodes A and D into a volume conductor with electrical conductivity σ and relative permittivity ε_r, and measurement of the resultant potential across electrodes B and C in a four-point (tetrapolar) measurement arrangement. In a two-point (bipolar) measurement, points A and D coincide with B and C. (d) The cell membrane acts as a capacitor (C_{membr}) and thus at low frequencies the current flows through the extracellular medium, which acts as a resistor (R_{extra}). With an increasing excitation frequency, the impedance of the capacitor gradually diminishes and current starts flowing through the cell membrane and the intracellular medium (R_{intra}) [24]. (e) The different dispersion regions. Adapted from [26].

characterized by a frequency dependent complex conductivity, $\sigma(\omega)$, or complex permittivity, $\varepsilon(\omega)$, based upon whether a material can be predominantly considered as a conductor with capacitive properties (accounting for displacement currents) or a lossy insulator with conductive properties, respectively. These are defined as [22]:

$$\sigma(\omega) = \sigma' + j\sigma'' \quad (2)$$

and

$$\varepsilon(\omega) = \varepsilon' - j\varepsilon'' = \left(\varepsilon_r' - j\varepsilon_r''\right)\varepsilon_o, \quad (3)$$

where

$$\sigma'' = \omega\varepsilon' \quad (4)$$

and

$$\varepsilon'' = \frac{\sigma'}{\omega}, \tag{5}$$

where ε_o is the permittivity of free space (8.85×10^{12} F/m). For example, for saline $\sigma = 1.6$ S/m and $\varepsilon_r = 80$. Below 250 MHz it behaves mainly as a conductor, but above that, as an insulator [22]. With regards to tissues, the epidermis, for example, acts more as a dielectric with some conductive properties, while muscle tissue acts primarily as a conductor with some dielectric properties [22].

Intracellular and extracellular fluids are ionic, composed of cations and anions that will migrate under the influence of an electric field. Charge carriers are thus largely ions (rather than electrons) that define the conductance of the material. Extracellularly, conductance is mainly defined by Na^+ and Cl^- ions. Free proteins in plasma are negatively charged also contributing to the conductance. Extracellular and intracellular fluids are thus primarily resistive in nature (R_{extra}, R_{intra}). On the other hand, cellular membranes act as barriers to current flow at low frequencies, demonstrating a capacitive behavior (C_{membr}). Thus, at low frequencies the extracellular space is probed (R_{extra}) [23], [24]. With an increasing frequency, membrane capacitive impedance is progressively diminished and increasingly more current flows through the membrane and into the intracellular space (R_{intra}). Low frequencies thus probe the extracellular space and high frequencies both intra- and extracellular spaces and intermediate frequencies interrogate cell membrane properties. This is illustrated in Fig. 1(d).

Tissues are highly anisotropic and inhomogeneous and demonstrate a high dielectric constant (10^6-10^7) below 100 Hz [25]. With increasing frequency, this is reduced in distinct steps in identifiable regions in the spectral characteristics, known as dispersion regions. There are four generally defined dispersion regions, α, β, γ and δ, as illustrated in Fig, 1(e) [22], [23], [26], [27]. The median value between two adjacent dispersion regions, i.e., between α and β, is called the characteristic frequency. The characteristic frequency of the α and β-dispersion regions can vary significantly between samples and tissues, but that of the γ-dispersion is relatively constant. The α-dispersion region is between mHz-kHz and is related with ionic diffusion, gated cell membrane channels and cell membrane effects. The β-dispersion region is between 0.1-100 MHz and is related to cell membrane polarization relaxations. The γ-dispersion region is between 0.1-100 GHz and is associated primarily with dipolar polarization mechanisms in polar media and the abundant tissue water. Between the β and γ regions, the δ region is related with protein molecules and other organic macromolecules, as well as intracellular structures, such as organelle membranes (e.g., mitochondria) [22], [23], [26], [27].

III. Bioimpedance Sensors

To measure bioimpedance, electrodes are needed as the interface between the electronic instrumentation and the biological matter. At the electrode contact with the biomaterial there is an interface impedance. In addition, there can be many different electrode arrangements that can be used to measure impedance. These are discussed in the following sections. Discussions are complemented with finite element method (FEM) simulations performed using Comsol Multiphysics (Stockholm, Sweden). Details about the FEM modeling process used can be found in the SI.

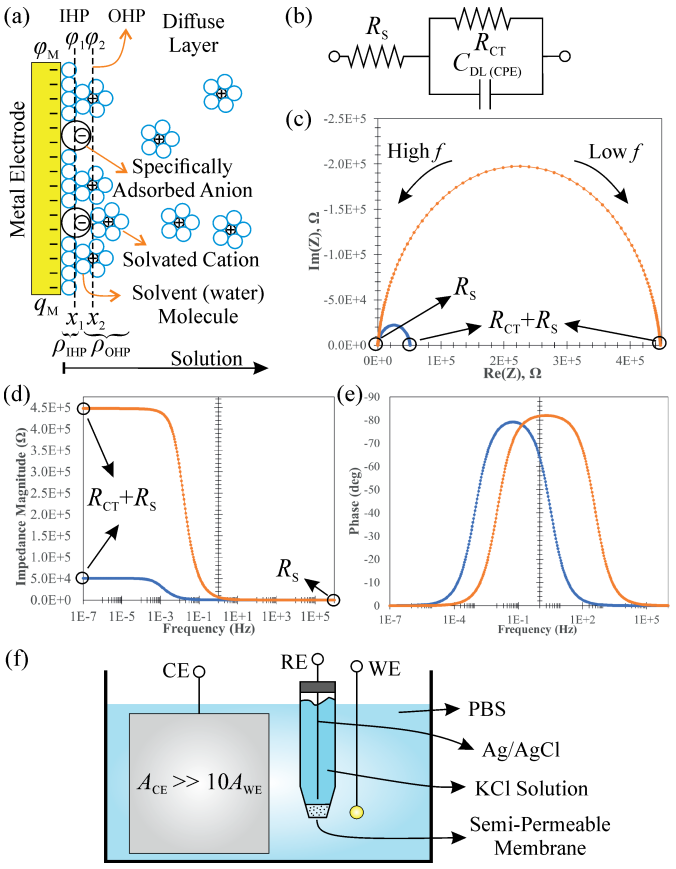

Fig. 2. (a) The double layer formed at the interface between a metal electrode and an electrolytic solution. Adapted from [33]. (b) A simple lumped equivalent circuit for the interfacial impedance. (c) Cole complex impedance plot for a Pt (orange curve) and Pt black covered Pt (blue curve) electrode and the corresponding (d) magnitude and (e) phase Bode plots, using the values from [30]. (f) A three-electrode electrochemical cell for electrode interfacial impedance measurements.

A. Electrode Interface Impedance

Before discussing electrode systems, the electrode/solution interface impedance must be understood. There have been a number of models to describe this interface, starting with the simple Helmholtz model. This was followed by the Gouy-Chapman diffuse model, which was succeeded by the dominant double-layer Stern model that combines the previous two into the compact Helmholtz layer and a subsequent diffuse layer. This was then modified by Grahame and others into a triple-layer model, by separating the Helmholtz layer into an inner and an outer part. The latter subsequently evolved into the water-dipole model by Bockhs-Devanathan-Muller, which considered the effect of the solvent (e.g. H_2O) dipole sheath on electrode surfaces and ions [28]. The double layer interface is illustrated in Fig. 2(a). On the electrode side of the interface, the charge carriers are electrons, while on the solution side of the interface, the charge carriers are ions, i.e., charged matter.

This fundamental difference in charge carriers leads to the formation of the double layer, which occurs instantly through the interaction between the two charge carriers. The metal will have many free electrons that are negatively charged. For an applied potential φ_M, there will be an accumulation of q_M charges in a very thin layer of the metal at the interface (<0.1 Å). For an electrode area A, the charge density is $\rho_M = q_M/A$, with units of C/m^2. On the biomaterial side at the interface, there will be a redistribution of ions in the solution; co-ions are repelled and there is an accumulation of counterions (positively charged ions) to counterbalance the charges on the electrode to achieve net charge neutrality ($q_M = -q_S$). Water is polar and thus contributes to the potential drop across the interface. Due to the strong interaction between the charged electrode surface and water dipoles, there is a strongly attached and oriented layer of water molecules hydrating the electrode. There can also be (depending on the medium composition) some dehydrated or partially hydrated specifically adsorbed species strongly attached on the electrode surface. Specific adsorption takes place due to electrical interactions between ions and electrode materials, leading to physical adsorption or chemisorption, depending on ion size and its hydration and relative force strengths. These form the inner Helmholtz plane (IHP), also known as the compact or Stern layer with a charge density of ρ_{IHP}. The outer Helmholtz plane (OHP) is composed of hydrated ions of the electrolyte with a ρ_{OHP}. Ions can approach at a distance limited to their radius (d/2), which controls the minimum distance of the IHP from the electrode (x_{IHP}) and the OHP from the IHP (x_{OHP}), together with their hydration sheath. There is a steep linear potential drop between the electrode and the IHP, with a small increase between IHP and OHP. Beyond the compact Helmholtz layers there is the diffuse (Gouy-Chapman) layer, within which electrostatic interactions are in competition with Brownian motion [29]. Here the potential decreases semi-exponentially with distance. This charge separation between the two sides of the interface resembles a parallel plate capacitor. The electrode interface model and its different layers are illustrated in Fig. 2(a). The total capacitance of the interface based on this model is then equal to [30]

$$\frac{1}{C_{DL}} = \frac{1}{C_{IHP}} + \frac{1}{C_{OHP}} + \frac{1}{C_{GC}} = \frac{1}{C_H} + \frac{1}{C_{GC}} = \frac{d_H}{\varepsilon_o \varepsilon_{r-H}} + \frac{L_D}{\varepsilon_o \varepsilon_{r-GC} cosh\left(\frac{z_c \varphi_M}{2U_t}\right)}, \quad (6)$$

where C_{IHP}, C_{OHP} and C_{GC} are the IHP, OHP and Gouy-Chapman capacitances, respectively, which are in series and $1/C_H = 1/C_{IHP} + 1/C_{OCP}$. Depending on how dilute or concentrated the electrolyte is and other factors, different parts dominate the overall capacitance, although recent reports suggest that the C_H always dominates the C_{DL}, with a Gouy−Chapman-like diffuse layer in an aqueous electrolyte established above a certain minimum ion concentration of around 1 mM [31]. ε_{r-H} is the permittivity of the Helmholtz layer, z_c is the ion charge (4 for O_2 reduction reaction), φ_M is the potential applied to the electrode, $U_t = RT/F = k_B T/q$ is the thermal voltage (∼26 mV), R = 8.314 J (K·mol)$^{-1}$ is the universal gas constant, F = 96,485 C mol^{-1} is the Faraday constant, k_B is the Boltzmann constant (1.380649 × 10^{-23} J·K^{-1}) and T is the temperature, which is 298 K at room temperature. d_H is the thickness of the Helmholtz layer, which is ∼3-10 Å. This is the closest distance of a hydrated ion to the electrode surface, since the radius of hydrated Na^+ and Cl^- ions is 3−4 Å and the diameter of a water molecule is ∼3 Å [31]. The Debye length L_D can be found by

$$L_D = \sqrt{\frac{\varepsilon_o \varepsilon_{r-GC} U_t}{2 n^0 z_c^2 q}}, \quad (7)$$

where q is the charge (1.602 × 10^{-19} C) and n^0 is the bulk number concentration of ions in the solution (9.3 × 10^{25} ions/m^3). The permittivity of the entire double layer is considered to be constant and equal to the bulk electrolyte. However, the high electric field within the Helmholtz layer reduces that from 78 to 4-14 [31]. These lead to a C_H of 12 μF/cm^2 [31]. Contrary to a standard capacitor, the capacitance is a function of the applied electrode potential, among other factors. Since C_{DL} does not behave like a perfect electronic capacitor, an empirical relationship has been derived to model it. This is known as the constant phase element (CPE), that is defined as

$$Z_{CPE}(\omega) = \frac{1}{(j\omega)^\alpha Q}, \quad (8)$$

where Q is referred to as the CPE parameter, which has no real physical meaning and has units of S·s$^\alpha$, where $s = j\omega$, and α is a constant ($0 \leq \alpha \leq 1$), referred to as the CPE exponent. When $\alpha = 1$, Z_{CPE} behaves like a perfect capacitor, when $\alpha = 0$ it behaves like a perfect resistor and when $\alpha = 1/2$ it represents an impedance with a 45° constant phase independent of frequency, known as the Warburg element used to model diffusion-limited processes. The Warburg diffusion element magnitude is, however, inversely proportional to the square root of the frequency. More information about the Warburg element can be found in [32], [33]. Thus, depending on α, the phase delay of the CPE is constant with a value of $-90° \cdot \alpha$. Care must be taken as in some sources, Q is within the brackets in (8).

Electrode materials can be categorized into two main groups. Electrodes that do not allow the passage of charge carriers through the interface are termed as polarizable or non-faradaic electrodes. This means that there are no faradaic reactions (reduction or oxidation) taking place on the electrode and thus have a strong capacitive behavior restricting charge transfer through the interface [34]. They also have a high charge transfer resistance, R_{CT}, and consequently, these electrodes lead to a very high interface impedance at low frequencies. With such electrodes there is thus no actual charge flow at the interface when applying a voltage, but rather a change of charge distribution associated with a displacement current [35]. Noble metal electrodes, such as Au and Pt are the closest to an ideal polarizable electrode. As discussed in [30], for Pt, charge transfer arises from the electrolysis of H_2O and the reduction of O_2 according to $2H_2O \leftrightarrow O_2 + 4H^+ + 4e^-$. At equilibrium, the potential of the electrode can be found

according to the Nernst equation at room temperature by

$$E_M = E^o + 2.303\frac{RT}{nF} \times pH = E^o - 0.05916 \times pH, \quad (9)$$

where E° depends on the reference electrode used and for a standard calomel electrode (SCE) this is $E_o = 0.987$ V, while for a standard Ag/AgCl electrode $E_o = 0.577$ V, and n is the number of electrons involved in the reaction, which is assumed to be equal to one. The 2.303 factor arises from the conversion of the natural logarithm into the decimal logarithm in terms of how the pH is defined. This dc potential is often symbolized as a battery in series with the equivalent RC circuit, and is referred to as the polarization potential, half-cell potential or the battery effect [35]. This can be a relatively large potential, with respect to voltages being measured and can thus saturate an amplifier with a high gain, while the dissimilarity of this voltage between ideally identical electrodes, leads to common-mode voltage errors in differential amplifier measurements [35].

Electrode materials that are easier to oxidize, allow relatively freely the passage of current through the interface and are termed as non-polarizable or faradaic electrodes, allowing reduction and oxidation (redox) processes to take place. These allow electrons in the conductor and ions in the electrolyte, to interact and pass on the net charge [34]. Such electrodes demonstrate a low R_{CT}. The Ag/AgCl electrode is the closest to an ideal non-polarizable electrode, where the AgCl layer acts as buffer for direct charge transfer through redox-based one-to-one exchange of electrons on the electrode and chloride ions in the electrolyte [36]. Ag/AgCl electrodes are good for skin measurements as disposable electrodes and not suitable for implantation and long-term use, due to the rapid dissolution of silver, while they can also be toxic. R_{CT} is defined as

$$R_{CT} = \frac{RT}{nFi_o}, \quad (10)$$

where n is the number of electrons involved in the electrode reaction and i_o is the exchange current density [30], [37]. From the above it is obvious that electrode interface impedance is inversely proportional to the area of the electrode, thus, its contribution to the measured impedance increases with decreasing electrode size.

When measuring the interface impedance, unavoidably the solution resistance, R_S will also be measured. The value of this depends on the solution conductivity, which for physiological saline solution is $\sigma = \sim$14 mS/cm, and the electrode geometry. For round electrodes with a radius r, this is [30]

$$R_S = \frac{1}{4\sigma r}, \quad (11)$$

and for square electrodes with a side length of l, this is

$$R_s = \frac{ln4}{\sigma \pi l}. \quad (12)$$

The simple lumped equivalent circuit for the interface impedance is shown in Fig. 2(b) and is thus comprised of R_S in series with the parallel combination of R_{CT} with C_{DL}. At low frequencies, the impedance of the capacitance is infinitely high and the current flows through R_S and R_{CT}, as C_{DL} acts as an open circuit, while at high frequencies the impedance of the capacitor is infinitely small and it is thus essentially a short circuit and the current flows only through R_S. Through knowledge of R_S one can then obtain R_{CT} and these can then be used as initial values for the fitting of the data to an equivalent circuit using dedicated software. One option is the freeware EIS analyzer by Bondarenko and Ragoisha [38] and the older LEVMW software by Macdonald [39], while ZView from Scribner Associates, USA is another popular commercial option. The Cole and Bode plots of Fig. 2(c)-(e) were obtained with the former option using the values for Pt and Pt black from [30], showing how one can obtain the R_S and R_{CT} values. This is further corroborated in the phase bode plot of Fig. 2(e) were at low and high frequencies the phase is zero, demonstrating a purely resistive behavior. It is important to note that in a Cole plot (Fig. 2(c)), low frequencies are at the right-hand side of the plot and high frequencies at the left-hand side.

In non-polarizable electrodes with a very low value of R_{CT} and a high equilibrium exchange current through the interface the processes taking place at the interface are diffusion-limited, and a Warburg element is placed in series with the R_{CT} to better model it. C_{DL} for Pt electrodes has been reported to be in the range of 0.545 F/m^2, while R_{CT} to be in the region of 300 kΩ or greater [30]. A value in the range of $\sim$30 Ω·cm^2 is often reported [30]. Other values reported include an R_{CT} between 40 and 290 Ω·cm^2 and C_{DL} between 12 and 47 μF/cm^2 for PtIr electrodes [40] and 192 F/m^2 for Pt electrodes [41].

1) Electrode Cleaning: The electrode fabrication method, impurities, adsorption of species on the electrode surface and the cleanliness of the electrode surface play an important role and will affect electrode interfacial properties [30], [42]. Electrodes should thus be cleaned prior to use or characterization, either chemically or electrochemically. Chemical cleaning of Au of Pt electrodes typically involves the use of piranha solution (H_2SO_4:H_2O_2 3:1) and rinsing with DI water to remove organic residues and ultrasonication in isopropyl alcohol (IPA) and deionized water for 15 - 20 min, followed by drying with nitrogen. Electrochemical cleaning by cyclic voltammetry (CV) of Pt electrodes involves cycling between -1.5 V and $+1.5$ V for 10 or more scans at a rate of 0.1 V/s in a 0.1 nM KCl solution. Cycling between –0.2 V and $+1.0$ V in 1 M H_2SO_4 can also be used. With Au electrodes cycling between -1.0 V and $+1.3$ V is used for 12 cycles or more at a scan rate of 0.1 V/s in 0.05 M H_2SO_4. Such electrochemical cycling processes lead to surface atom reorientation and/or changes of the metal-solution interface, that alter the electrode electrochemical behavior. More discussions can be found in [43].

B. Measurement of the Electrode Interface Impedance

Characterization and measurement of the electrode interface impedance can be predominately done using impedance measurements is a phosphate buffered saline solution (PBS). Tablets, such as product P4417 from Sigma-Aldrich, USA, in every 200 mL of deionized water can be used to obtain PBS. One way to measure interface impedance is by bipolar

measurements, where one electrode is the electrode that the interfacial impedance of which needs to be characterized, i.e., the working electrode (WE). The second electrode, known as the counter electrode (CE), needs in this case to be significantly larger in area than the WE to ensure that its interface impedance is negligible compare to that of the WE. Stainless steel and Pt sheets are often used as CEs [44], [45]. Apart from the interface impedance of the CE being part of the measurement, another issue with this is that it does not allow a stable electrode polarization to be quickly achieved. This is experimentally seen as a varying electrode interface impedance being measured as a function of time, which eventually becomes stabilized, at which point it can be used for measurement. Both issues are overcome with three electrode measurements, as in Fig. 2(f). An alternative is to use the same electrode as the WE for the CE. The electrode impedance will then be half the measured impedance after deducting the solution resistance. The disadvantage of that is that two electrodes will never be exactly the same, due to nanoscale defects altering their real surface area. In the three-electrode cell, the third electrode is the reference electrode (RE), a Ag/AgCl non-polarizable electrode, that measures the solution bias potential, which is used with feedback to ensure it is stable by supplying the appropriate current through the CE. This is a classic three-electrode system used with a potentiostat and provides the most accurate and stable measurements for probing electrode interface phenomena (Fig. 2(f)). The RE needs to be close to the WE to minimize ohmic potential drops. The CE area still requires to be larger than that of the WE ($A_{CE} = \sim 10\ A_{WE}$). Interfacial properties can also be probed using methods such as CV and other approaches and variants (e.g. using redox species) [46]–[48], but impedance spectroscopy in PBS is typically sufficient for bioimpedance sensor characterization, particularly since small excitation signals are used and thus a linear relationship between voltage and current can be assumed [31], [49].

C. Simulating the Electrode Interface Impedance in FEM Tools

Numerical simulations using finite element method (FEM) modelling have been used to model the electrode interface impedance. Many different approaches have been applied to do this, some of which are quite complex and covering them in detail within this paper is not possible. We will thus discuss them at a high level to provide an overview and pinpoint the interested reader to the relevant sources.

In one approach, Poisson, Nernst-Plank and Butler-Volmer equations are solved without applying electroneutrality and Boltzmann distributions, as in [50] and [51] for simulating the cyclic voltammetry response of nanoscaled electrodes. The surrounding electrolyte was separated into two domains, one representing the compact layer and the second for the diffuse layer. The compact layer was separated into the IHP and OHP. The plane of closest approach (PCA) for all the ions is the OHP and is the position of electron transfer (PETr). Adsorption and electrode roughness are ignored. Within the compact layer there is thus no ionic flow and transport and the Poisson equation is sufficient to model the electrostatic problem within this layer for a charge density of zero ($\rho = 0$)

$$\nabla \left(\varepsilon_o \varepsilon_r \nabla V\right) = -\rho. \tag{13}$$

Within the compact layer, ε_r varies progressively. A smooth and continuous profile for ε_r within the compact layer can be achieved by using a hyperbolic function within the IHP and a cosine function within the OHP, followed by a constant value within the bulk electrolyte and the diffuse layer [50], [51]. If the electrode is circular with a radius of r_o, the IHP extends up to $r_o + l_1$ and the OHP up to $r_o + l_1 + l_2$, then

$$\varepsilon_r = \begin{cases} \varepsilon_1 \cosh^2\left[S_1\left(r - r_o\right)\right], & r_o \le r \le r_o + l_1 \\ \varepsilon_2 \cos^2\left[S_2\left(l_1 + l_2 + r_o - r\right)\right], & \\ & r_o + l_1 \le r \le r_o + l_1 + l_2 \\ \varepsilon_2, & r_o + l_1 + l_2 \le r, \end{cases} \tag{14}$$

where ε_1 is the permittivity of the electrode material, ε_2 of the solution and S_1 and S_2 are constants ensuring continuity between the IHP and OHP at l_1. The values used for these variables in [50] are $\varepsilon_1 = 6$, $\varepsilon_2 = 78$, $S_1 = 3.6$, $S_2 = 3.05$, $l_1 = 0.4$ nm, $l_2 = 0.3$ nm. Beyond the OHP within the electrolytic domain, both electrostatics (using the Poisson equation above) and electrokinetic flow need to be considered as both electron transfer and ion transport are involved. To achieve this, a ρ that is determined by the concentration (c_i) of ionic species (i) and charge valence of ions in solution (z_i) is considered: $\rho = \sum_i z_i c_i$. As discussed in [50], due to both the electric field and the concentration gradient, ionic mass transport is governed by both diffusion and electromigration (convection is ignored), described by the Nernst-Plank equation

$$\frac{\partial c_i}{\partial t} = D_i \nabla^2 c_i + \frac{z_i F}{RT} D_i c_i \nabla V, \tag{15}$$

where D_i is the diffusivity of species i and t is the time. These are solved by considering a solution with an electroactive reactant species (thus reduction and oxidation and a faradaic current are considered), a pair of excess electroinactive cation (A^+) and anion (B^-) which constitute the supporting electrolyte, and a counter ion (Ct, that can either be positive or negative with a concentration 1 to 3 times the reactant ion, O^z, at a concentration 100 times that of the reactant). The diffusivity and concentrations of these considered in [50] were $D_O = D_R = 1 \times 10^{-9}$ m^2/s, $D_A = 1.33 \times 10^{-9}$ m^2/s, $D_B = 2.03 \times 10^{-9}$ m^2/s, $D_{Ct} = 1 \times 10^{-9}$ m^2/s, $c_A^b = c_B^b = 500$ mol/m3, $c_O^b = 5$ mol/m3, $c_R^b = 0$ mol/m^3 and $c_{Ct}^b = |z|\, c_O^b$ for z = {−3, −2, −1, 1, 2, 3}. At the PETr, the redox event for the reactant ion is described by the following generalized reaction

$$O^z + e^- \underset{k_b}{\overset{k_f}{\leftrightarrow}} R^{z-1}, \tag{16}$$

where O^z is the reactant species in its oxidized form, R^{z-1} is the reduced species, k_f is the reduction and k_b the oxidation rate constants. The rate constants according to Butler-Volmer

kinetics are calculated according to

$$k_f = k_0 exp\left[-\frac{\alpha F\left(E_t - V - E^{0'}\right)}{RT}\right] \quad (17)$$

$$k_b = k_0 exp\left[\frac{(1-\alpha)\, F\left(E_t - V - E^{0'}\right)}{RT}\right], \quad (18)$$

where k_0 is the standard electron transfer rate, α_o is the charge transfer coefficient, E_t is the electrode potential, V is the potential at the PETr and $E^{0'}$ is the redox couple standard potential. The values used as constant in [50] were $E^{0'} = 0$ V, $k_0 = 10$ m/s and $\alpha_o = 0.5$. The dynamic current flux at the PETr is defined by

$$j_f = -j_b = k_0 exp\left[-\frac{\alpha F\left(E_t - V - E^{0'}\right)}{RT}\right] \times c_O - k_0 exp\left[\frac{(1-\alpha_o)\, F\left(E_t - V - E^{0'}\right)}{RT}\right] c_R. \quad (19)$$

A similar approach where the individual layers of the interface are modelled by applying the appropriate boundary conditions at different distances from the electrode surface (at 0.3 nm for the Helmholtz layer and further away for the Gouy-Chapman layer), was followed in [52]. A detailed modeling approach for the double layer was described in [53], which is however beyond the scope of this paper.

To model the double layer the following Robin boundary condition was applied in [41], which is a linear combination of Dirichlet and a Neumann boundaries. This contact impedance boundary condition is used as the electrode is much larger than the double layer and it is thus a simpler means (computationally) to model the interface, rather than defining domains that are much smaller and thus require significantly smaller mesh elements. This is defined as

$$J_0^* = -\sigma^* \nabla V_0^* = (j\omega)^{\alpha}\, Q_{DL} \Delta V_{DL}^*, \quad (20)$$

where α and Q_{DL} have the same definition as in (8), $V_{DL}^* = V_E^* - V^*$ is the potential across the double layer, V_E^* the applied electrode potential and V^* the potential at the double layer bulk interface. This formulation, thus, takes into account the CPE characteristics of the interface. This is a thin-layer approximation. This approach can nowadays be easily implemented in Comsol Multiphysics through the contact impedance boundary conditions as a thin layer (entering the properties of the material together with the layer thickness) or as a surface impedance (entering the impedance properties of the thin layer directly). A similar approach has been used by approximating the double-layer to be 1 nm thick in total and with uniform thickness and electrical properties in [54]. Another approach involves the modelling of the interface as a lumped RC equivalent circuit based on experimental values and incorporating this into the FEM model. In [55], this was modelled as a 192 pF (0.271 F/m^2) capacitor.

Modelling the interface impedance is important when modelling in FEM tools a part of the body and there is a need

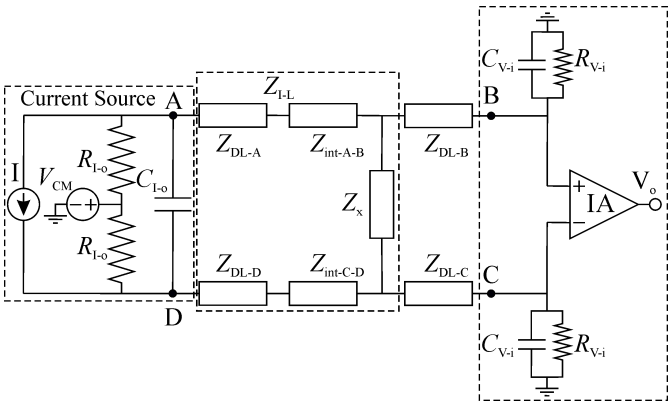

Fig. 3. Simplified equivalent circuit of a tetrapolar measurement arrangement. For a bipolar measurement points B and C are moved to points A and D and there are no $Z_{\mathrm{DL\text{-}B}}$ and $Z_{\mathrm{DL\text{-}C}}$, while $Z_{\mathrm{int\text{-}A\text{-}B}}$ and $Z_{\mathrm{int\text{-}C\text{-}D}}$ are parts of Z_{x}. V_{CM} is the common-mode voltage. Adapted from [9], [18], [56], [57].

to incorporate all aspects of the measurement, the different tissues etc., to model the impedance response being measured, to evaluate the voltage across the current injection electrodes and the potential across the voltage measurement electrodes, as a means of understanding what is being measured and to obtain rough estimates of the design specifications for the electronics. The double layer impedance is not typically implemented in models targeting the optimization of the electrodes, in terms of their geometry, which is most often performed in homogeneous and isotropic volume conductors for simplicity. In fact, it is assumed that the double layer will not affect the current density profile significantly within the volume conductor and it can thus be ignored in this type of simulations.

D. Reduction of Electrode Interface Impedance

1) The Need for Lower Interfacial Impedance: Reducing electrode contact impedance is of paramount importance. Fig. 3 illustrates the equivalent circuit of tetrapolar measurements [9], [18], [56], [57]. Ideally, all double layer impedances (Z_{DL}) should be equal if all electrodes are of the same geometry, but this is not the case leading to common-mode errors. Z_{int} is the impedance seen between an injecting and a measuring electrode (A-B and C-D, see Fig. 3 and 4) within the volume conductor. In bipolar electrode systems, interface impedance reduction reduces the contributions of the electrode interfacial impedance ($Z_{\mathrm{DL-A}}$ and $Z_{\mathrm{DL-D}}$ in Fig. 3) to the total measured impedance and thus lower frequency impedance measurements can be accommodated. In tetrapolar impedance measurements, as discussed, the interface impedance is not measured. However, in all cases, whether the impedance is contributing to the measured impedance or not, it will always be part of the entire measurement system, as shown in Fig. 3. The ac current source that injects the current into the system will see both in bipolar and tetrapolar measurements, the interface impedance ($Z_{\mathrm{DL-A}}$ and $Z_{\mathrm{DL-D}}$ in Fig. 3, corresponding to the circuit of Fig. 2(b)) at the two electrodes between which the current is injected. This forms a big part of the current source load impedance. The value of the load impedance ($Z_{\mathrm{I-L}} = Z_{\mathrm{DL-A}} + Z_{\mathrm{DL-D}} + Z_{\mathrm{int-A-B}} + Z_{\mathrm{int-C-D}} + Z_{\mathrm{x}}$) at the

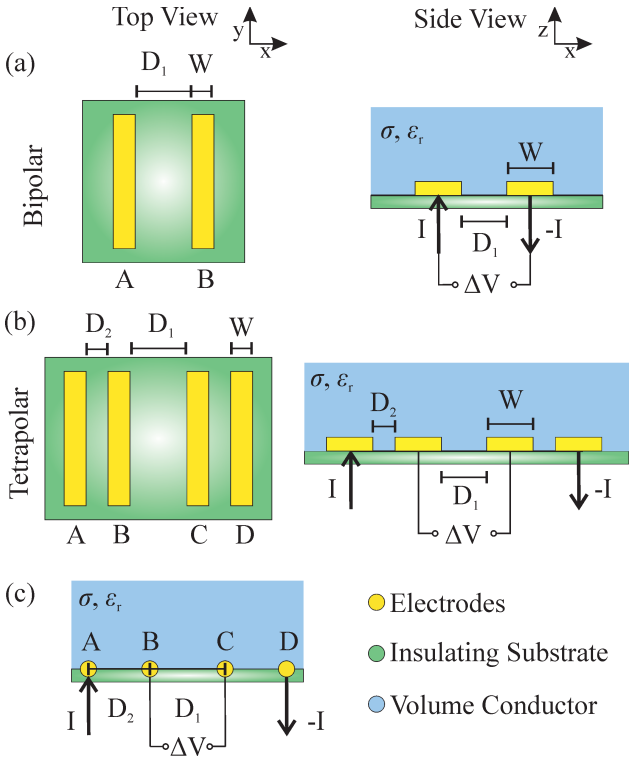

Fig. 4. Top (left) and side (right) views of coplanar electrode arrangement with parallel electrodes: (a) bipolar and (b) tetrapolar. (c) Point electrode approximation on a semi-infinite half plane.

lowest frequency of interest (because this is where the interface impedance will be maximum), times the injected current (I), defines the minimum required voltage swing possible at the output nodes of the current source, i.e., the output voltage compliance. If this is not met, the output current will be distorted. This of course depends on the power supply of the current source, among other parameters. Consequently, keeping the interface impedance small, allows larger current injection for a set power supply and thus higher signal to noise ratio (SNR), or for a set current amplitude, a lower power supply, and thus lower power consumption. In order for the current source to deliver the required current, its output impedance ($R_{I-o}//C_{I-o}$) needs to be significantly greater than the load impedance throughout the bandwidth of interest. As the Z_{DL}'s form the biggest part of Z_{I-L}, reducing them will allow greater accuracy in the injected current and relaxes the design specifications for the current source. In addition, across the injecting electrode interface impedance, there will be a potential drop. The greater the interface impedance, the greater the potential drop, thus limiting the voltage signals across Z_x and thus imposing constraints with regards to SNR, amplification and bandwidth to the front-end voltage recording amplifier. The potential difference of course will be the same for a set current and load being measured, but the individual signals at each amplifier terminal will be smaller. Ideally the input impedance ($R_{V-i}//C_{V-i}$) of the instrumentation amplifier (IA) measuring the potential difference of the voltage measuring electrodes needs to be infinite across the bandwidth, to ensure no current flows through these electrodes. In reality this may not be the case, leading to measurement errors and thus a potential drop across the interface impedance of the voltage measurement electrodes. The smaller their interface impedance, the smaller this error will be if there is a current flow, further ensuring that the amplifier input impedance is sufficiently high. The large voltage drop across the interface impedance further facilitates undesirable electrochemical reactions at the interface that can be harmful to biology [30], [58].

2) Noise: Large electrode impedance is also associated with higher electrode noise, further reducing SNR [58]–[60]. Stochastic fluctuations in ion transport led to thermal noise. At the electrode, the square magnitude of the thermal voltage noise ($\overline{v_n^2}$) is proportional to temperature (T), electrode impedance magnitude ($|Z|$), and spectral bandwidth (Δf) according to [36]

$$\overline{v_n^2} = 4kT\,|Z|\,\Delta f. \tag{21}$$

The random fluctuations in mass transport at the electrical double layer, lead also to 1/f noise [36].

3) Motion Artefacts: Electrode movement relative to its original location is translated into a measurable potential change across the interface [61]. This is due to the induced changes in the interfacial properties between electrodes and tissue, that change the electrode half-cell potential and interface impedance. Between electrode pairs, as the effect of the mechanical perturbation can be different, this will lead to a differential voltage signal appearing that will lead to common-mode errors. These are termed as motion artefacts. Polarizable electrodes, due to the higher interface impedance, are more susceptible to them in addition to higher noise levels [35]. The frequency components of motion artefacts are typically below 20 Hz, which is well below the frequencies typically used in bioimpedance applications and can thus be easily filtered out [35]. Removal of motion artefacts can be accomplished with time averaging and frequency analysis based on filter banks or wavelet transforms or other methods such as blind source separation or adaptive filtering [62]. Impedance measurements can be used as a means of monitoring and filtering out motion artefacts [62]. It was found in [62] that wet electrodes (lower interfacial impedance) achieve a higher correlation between measured impedance and motion artefacts than dry (higher impedance) electrodes despite achieving larger impedance changes. Wet electrodes demonstrated about half a decade smaller impedance variation due to induced motions than dry electrodes [62]. Consequently, keeping the electrode impedance small, relaxes the instrumentation design specifications and allows measurements at lower frequencies.

4) Methods for Interfacial Impedance Reduction: Many different approaches have been developed to reduce the interface impedance. The most popular approach involves the electrochemical deposition of Pt black. There are many Pt black deposition protocols described in the literature. Typically, a chloroplatinic acid solution (H_2PtCl_6) with either lead acetate trihydrate ($Pb(C_2H_3O_2)_2$) [63]–[65], or lead nitrate ($Pb(No_3)_2$) [66], or lead chloride ($PbCl_2$) [67] is used and electrochemical deposition is performed under ultrasonic agitation [63]–[66]. The latter serves the purpose of removing

weakly adhered Pt from the electrode surface, to obtain mechanically stable electrodeposited films. Current-controlled electroplating and a lead acetate solution is more common. In our group we have used a solution composed of 12.5 ml of chloroplatinic acid (8 wt. % in H_2O, Sigma-Aldrich Prod. No.: 262587), 2.5 μL hydrochloric acid (1 M, 1 N, Sigma-Aldrich Prod. No.: 1.09057), 5 mg lead acetate trihydrate (Sigma-Aldrich Prod. No.: 215902), which is then filled with deionized water to reach 100 ml. A three-electrode cell (Fig 2(f)) is used to deposit Pt black on the working electrode for 120 sec with a current of 28 mA/cm^2, allowing interfacial impedance reduction from $\sim$1 MΩ to $\sim$1 kΩ, i.e. three orders of magnitude [49]. The Cole and Bode plots of Fig. 2(c)-(e) simulated using the experimental values reported in [30] demonstrate the difference in impedance achieved with Pt black deposition. Others have used larger deposition current and shorter or longer times (300 mA/cm^2 for 10 s. -5 μA for 9 s) [5], [30], [65]. Potentiostatic deposition is also used (-200 mV vs. Ag/AgCl for 100 s) [68], as is pulsed current deposition (duty ratio of 5 ms:500 ms, peak current density of 4.5 A/cm^2, 480 cycles) [63].

Electropolymerizing poly (3,4-ethylenedioxthiophene) with polystyrenesulfonate dopant (PEDOT:PSS), a conducting polymer, directly on electrodes is another approach. PEDOT is electrochemically stable and decreases electrode interfacial impedances up to about two orders of magnitude [69], due to an increase in surface area and the high ionic conductivity of PEDOT. Galvanostatic rather than potentiostatic deposition has been found to lead to more stable and uniform films [69]. A current density of 0.64 mA/cm^2 with a deposition time in the region of 300 s to 500 s was found to be ideal, as longer times lead to overexpansion of the deposited film and unstable films [69]. In [70], a current density of 100 μA/mm^2 for 120 s was applied for the deposition of PEDOT:PSS, achieving a reduction of electrode impedance greater than 2 orders of magnitude; 8 μA/mm^2 for 300 s was used in [68]. Nevertheless, Pt black can achieve smaller interface impedances [68]. Electrochemical cleaning of the electrodes is recommended prior to plating, e.g. by injecting 500 μA for 60 s in deionized water as in [5], or 750 μA for 5 s [71].

A third method involves the use of carbon nanotubes (CNT). In [64], a CNT suspension was dropped on platinum electrodes. These demonstrated reduced electrode interfacial impedances when compared to Pt black-modified electrodes. Alternatively, CNT suspensions can be deposited on conductive electrodes via electrophoresis [72]. Single-walled (SWCNT) and multi-walled CNT (MWCNT) suspensions with an appropriate surfactant can be electrophoretically deposited on electrodes using a two-electrode cell with applied dc voltages between 5 V to 600 V, deposition times between 0.5 min to 20 min and electrode separation between 1 mm to 50 mm, as reported in [72]. In [73] the electrode impedance at 0.2 Hz became $\sim$2.7 times smaller following electrophoretic deposition of MWCNTs on stainless steel electrodes. It was reported in [74] that higher concentration suspensions and larger voltages lead to more homogeneous films, with uniform film thickness and higher film quality achieved with 10 μm final film thicknesses.

Finally, the combination of CNTs and PEDOT:PSS has also been proposed. Such composite coatings have been found to outperform PEDOT, achieving greater reductions in impedance, and greater surface area, conductivity and mechanical stability [75]. PEDOT-CNT films achieved 1.29 times lower impedance than just PEDOT films in [76], with the former achieving 25% thicker coating for the same deposition parameters. In [75], PEDOT-CNT achieved four orders of magnitude lower impedance than unmodified gold electrodes. According to [77], PEDOT-CNT composite coatings are more stable than PEDOT. Au electrodes with a 1 kHz impedance of $\sim$8 MΩ achieved an impedance of $\sim$97 kΩ with a PEDOT:PSS coating and a $\sim$90 kΩ impedance with PEDOT-CNT coating [77]. The mechanical adhesion strength of the CNTs on electrodes can be weak. In [78], this was improved by using a thin coating of polypyrrole (PPy), another conducting polymer.

Before moving onto the subsequent discussions, it is also important to note that the pressure applied on the electrode and tissue will also affect the interface properties, as well as the measured impedance [79]. It is important thus to ensure that the applied pressure is constant throughout the measurement and that when comparing spectra between different samples and conditions, the same pressure is applied. Ideally minimal pressure should be applied (below 20 kPa) and monitored with pressure sensors, to avoid the migration of extracellular fluid and the decrease of tissue thickness due to compression [79].

E. Reciprocity and Sensitivity in Electrode Systems

In a four-port system consisting of four electrodes placed on points A, B, C, and D on the surface s of an isotropic arbitrary volume v, with a permittivity, ε_r, and conductivity, σ (see Fig. 1 and Fig. S3 in the SI and Fig. 4(b)-(c)), reciprocity applies, according to which injecting and measuring leads can be interchanged without a change in measured impedance. As derived in the SI, sensitivity (S) is defined as the dot product of the current density distributions resulting from the two reciprocal current injections, normalized by the product of the two currents.

$$S = \frac{J_1 \cdot J_2}{I_1 I_2}, \tag{22}$$

with units of 1/m^4. S defines the contribution of each infinitesimal point within the volume conductor to the total measured impedance. Within the context of bioimpedance it was first derived by [80] and was followed by the derivation and generalization of [81], [82]. S is a vectorial dot product. Consequently, it can have positive, negative and zero values, based upon the orientation of the field lines resulting from the two reciprocal solutions of the problem in each point within the volume conductor. If the two vectors (J_1 and J_2) are perpendicular to each other, then $S = 0$ and if there is an impedance change within this region, no change in measured impedance will be registered. If the vectors are at an angle less than 90°, S is positive and an increase in impedance in that region will be indeed measured as an impedance increase. This is not the case, however, when the angle between the two vectors is more than 90°, which leads to a negative S. Within

such areas, if there is an impedance increase, it will be detected as a decrease in impedance and vice versa. The magnitude of the sensitivity indicates how much each point contributes to the total measured impedance. It is thus essentially a gain factor. The S distribution of an electrode arrangement should thus be known to be able to interpret measurements for a particular application. In addition, it can be used as a means of optimizing the electrode system to achieve high sensitivity to regions within the volume conductor, where detection is to take place. Ideally, negative sensitivity regions should be minimized, as they can lead to erroneous interpretation of results and can even shadow events of interest. Bipolar electrode systems have only two electrodes; points A and D coincide with points B and C and thus the two electrode pairs are reduced to one, as in Fig. 4(a). Consequently, the dot product in S is the square of the resultant current density, which will always be positive.

$$S_{bipolar} = \frac{J_x^2 + J_y^2}{I^2}. \tag{23}$$

It is important to note that the integral of S is what is known as the geometrical cell constant (CC).

In the following discussion we will primarily deal with microscale electrodes fabricated on a common substrate, that are coplanar and parallel to each other. The arrangements studied here are thus suitable for regional small volume impedance measurements more relevant to implantable and wearable applications. Nevertheless, the methods and analysis used are applicable to any electrode arrangement.

F. Depth of Investigation

The sensitivity theorem has been extensively applied in the field of dc resistivity imaging for geophysical prospecting. Significant work was done to obtain and optimize the depth of investigation of electrode arrays, defined as the distance over the plane of the electrodes up to which the electrode is sensitive or most sensitive. In bipolar electrodes this has been defined as the depth where most of the current is confined. This has been exploited in [83] for the optimization of interdigital electrodes for bacterial detection, by confining 90% of total electric field strength below a distance of 5 μm from the sensor surface using FEM simulations. The same approach was followed in the nanoscaled interdigitated electrode array for biochemical sensing of [84] and in [85], [86] using an 80% threshold and conformal mapping (CM) simulations. As it was shown in [85], [86], the field confinement over the middle of the electrode array saturates fast as the electrode width increases demonstrating that W does not influence as much the field confinement. This is not the case with the separation between the electrodes, that demonstrates a linear relationship with depth of field confinement. Similarly to E, the bipolar S can also be used. The two approaches have been compared in [87], indicating the former approach results in a more strict condition for the depth of investigation, leading to electrodes with a smaller electrode distance.

In tetrapolar arrangements, this has been defined as the depth over the electrode plane at which an infinitely thin and long obstacle, provides a maximum measurement of impedance. If S is integrated along x, S with increasing z distance from the electrode plane gradually increases, reaching a peak value and it then gradually decreases towards zero [19], [85], [87]–[90]. Consequently, the peak value can be used to indicate the depth of investigation [85], [87]–[89]. Another definition involves the median depth of investigation, defined as the depth containing 50% of the total S. A more strict condition is a 90% confinement as in [6]. The percentage of the sensitivity to the total as a function of distance from the electrode surface can be found by [18], [19]

$$z_{median} = \frac{\int_{z=0}^{z=z_{median}} \int_{x=-\infty}^{x=\infty} S.dxdz}{\int_{z=0}^{z=\infty} \int_{x=-\infty}^{x=\infty} S.dxdy} 100. \tag{24}$$

A similar approach has followed in [91] to establish the sensitivity over specific volumes of interest and the contribution of different tissues to the total measured impedance as a function of frequency.

G. Bipolar Impedance Sensors

The simplest way to measure electrical impedance is to use two electrodes, as in Fig. 4(a). One of the electrodes can be used as a ground electrode or preferably, the ac signal applied to that second electrode should be 180° out of phase of the one applied at the other electrode. Thus, this involves a differential excitation. The dc voltage on each electrode should be the same, to apply a zero net dc signal to the biomaterial under study (BUS).

The geometry and arrangement of the electrodes dictates the distribution of the electric field and thus which areas of the BUS are contributing to the measured impedance. The scenario of two electrodes facing each other with the BUS between them is well known, as it resembles a parallel plate capacitor with a largely homogeneous electric field around the central part of the electrodes and fringing field at the electrode edges. Such a scenario would be of interest for example when using large electrodes to measure bulk tissue properties and it has been used in impedance cell cytometry.

What is of particular interest is the electric field properties of coplanar electrodes. Most often these electrodes are sub-mm and are of interest for wearable and implantable applications, but also for biosensing. The electric field penetration above the electrode plane and within the volume conductor greatly depends on the separation of the electrodes [22], [85], [86]. The dependence of the electric field distribution on the electrode width is weaker. The length will influence how much BUS within the BUS depth defined by the electrode separation is interrogated. This has been studied with both numerical and analytical methods. FEM modelling is a powerful numerical approach for electromagnetic simulations, nevertheless, if the problem is simple enough, analytical approaches can be used to study them and to provide equations that can allow a greater insight into the problem, as by just reading the equation or simply solving it by varying just one parameter, one can see how each parameter influences the electric field.

1) Point-Electrode Approximation: This has been approached largely by two methods in the literature. Both are for 2D modelling of the problem. One involves considering the electrodes as simple point sources. This is a simple and insightful

approach, but since it does not consider the full electrode geometry, in particular the electrode width, it is problematic when optimizing the separation between electrodes [5], [18], [92]. The point-electrode approximation is thus useful, when the electrodes are small and the separation between electrodes is to be kept relatively large to interrogate large portions of the BUS. This will be discussed in more detail in subsequent sections and in the SI.

2) Conformal Mapping: Another approach involves the use of conformal mapping (CM), where a complex problem is mapped into a geometry that is much easier to characterize mathematically and to solve the equations of interest [84]–[86], [93]–[98]. Its use is predominantly limited to 2D homogenous and isotropic half- spaces. The solution can then be back transformed to the original geometry allowing thus analytical mathematical expressions to be obtained for further numerical optimization. This can be useful when the distance between electrodes is to be kept small and small regions of the BUS are of interest. Under CM, Laplace's equation remains invariant, while the orthogonality between potential and flux lines remains. The Schwarz-Christoffel transformation for polygonal boundaries is often used. Derivations and detailed discussions on the equations and use of the transform are elaborated in the SI and discussed in summary below. Let us consider two coplanar electrodes, parallel to each other in a semi-infinite Cartesian half-space, with the x-axis extending between $\pm\infty$ and the y-axis between 0 and $+\infty$. The length (L) of the electrodes is considered much larger relative to the electrode width (W) and separation (D), to consider the model in 2D, as in Fig. 5(a); the electrode thickness is considered negligible. To evaluate the electric field (E) and current density (J) and obtain analytical expressions for these, the half-space is mapped into the interior of a rectangle, as in Fig. 5(b). If in the original space, the electrode lied between $\pm D/2$ and $\pm(D/2 + W)$, by normalizing the place by $D/2$ it now lies between ± 1 and $\pm 1/k$, with $0 < k < 1$, where:

$$k = \frac{D}{D + 2W}. \tag{25}$$

The Schwarz-Christoffel transformation mapping the original half-space into the rectangle becomes [98]:

$$z(t) = \int_0^t \frac{dt}{\sqrt{\left(1 - t^2\right)\left(1 - k^2 t^2\right)}}. \tag{26}$$

This is an elliptic integral of the first kind [99]. In this way, the electric field distribution is mapped from a coplanar geometry (T-plane, Fig. 5(a)) to a parallel plate geometry (Z-plane, Fig. 5(b)), with the two electrodes mapped to the sidewalls of the rectangle and the entire semi-infinite half-space mapped within it. As shown in Fig. 5(b), there is a uniform electric field between the two electrodes, a problem that is well known with simple equations characterizing the electric field, allowing the simple calculation of the potential at any point. In the original plane the electric field is equal to the electric field in the transformed plane multiplied by the

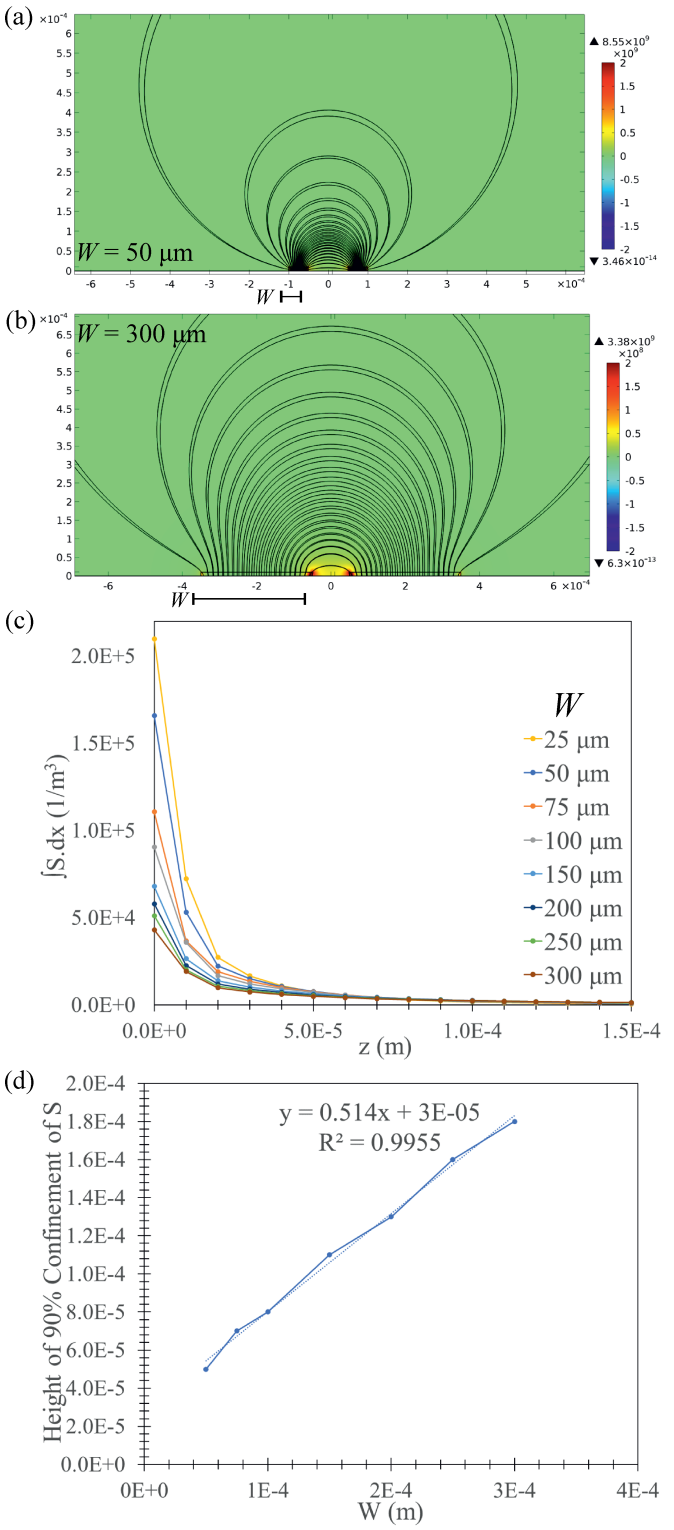

Fig. 5. (a) The original semi-infinite halfplane and (b) the transformed geometry. The flux and iso-potential lines in the transformed domain are also shown. The location of the electrodes in both planes is in yellow. Adapted from [87].

complex conjugate of the derivative of the mapping function:

$$E_t = \frac{1}{2K(k)} \cdot \frac{\bar{1}}{\sqrt{\left(1 - t^2\right)\left(1 - k^2 t^2\right)}}, \tag{27}$$

where $t = x + jy$. The real part of E_t gives the x-component and the imaginary part the y-component of the electric field.

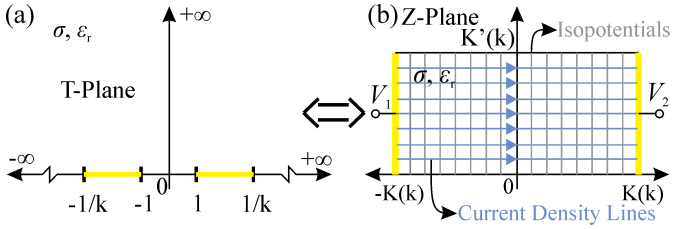

Fig. 6. Examples of the sensitivity distribution (colour map) and field lines for (a) W = 50 μm and (b) W = 300 μm. Variation of W and its effect to (c) the integrated bipolar S (with respect to x) and (d) 90% percentage confinement of S.

In the T-plane, at $x = 0$, the field lines achieve maximum volume penetration. At this point, the y-component of the electric field is zero and if the potential at one electrode is set to 1 V and to the other at 0 V, the x-component is equal to:

$$E_{tx} = Re\,(E_t)_{x=0} = \frac{1}{2K\,(k)\sqrt{1 + y^2 + k^2\left(y^4 + y^2\right)}}. \quad (28)$$

It is clear from this equation, that through k, the electric field is directly related to W and D. The resistance and capacitance between the two parallel facing electrodes can very easily be calculated. Ohm's law allows then the calculation of the current, I, that can be used to calculate the sensitivity, S. In the bipolar system, the two current densities in (22) are equal $J_1 = J_2$ and thus, the sensitivity of the bipolar system can be very easily obtained, and it is always positive, as shown in (23). Electrode thickness can be accounted for by an equivalent effective electrode width (W_e) approximation [93]:

$$W_e = W + \left(\frac{t}{\pi}\right)\left[1 + ln\left(\frac{4\pi W}{t}\right)\right] \quad (29)$$

In this way the effect of the electrode width and separation can be investigated using analytical mathematical expressions. Comparison with FEM simulations verify the accuracy of the above expressions [85]–[87].

3) FEM: Of course, FEM simulations are more powerful and can provide very accurate solutions. There has been a tremendous advancement over the last 20 years in commercial FEM tools and together with advancements in computation, their use is simple, and is ideal for complex models and problems that cannot be reduced and approximated in 2D. Using FEM, the results of Fig. 6-7 were obtained by varying W between 25 μm and 300 μm (Fig. 6) and D between 100 μm and 1 mm (Fig. 7). The peak sensitivity is at $z = 0$ and increasing W decreases it. Within the values considered in these models, with increasing W, there is a linear increase in the 90% confinement height as defined by (24) (Fig. 6(c-d)). For an increasing D, as evident from the inset of Fig. 7(c), S increases and the 90% confinement height varies linearly (Fig. 7(c-d)). This approach can be used to design any bipolar impedance sensor, including interdigital sensors, with the appropriate model in place of course.

A disadvantage of bipolar impedance measurements, particularly when measuring small impedances as is the case of tissues, is that the impedance of anything between the voltage measurement amplifier connected at the two electrodes, and the sample contributes to the total measured impedance. This will thus include, PCB/instrument parasitics, the impedance of the leads/interconnects connecting the instrumentation to

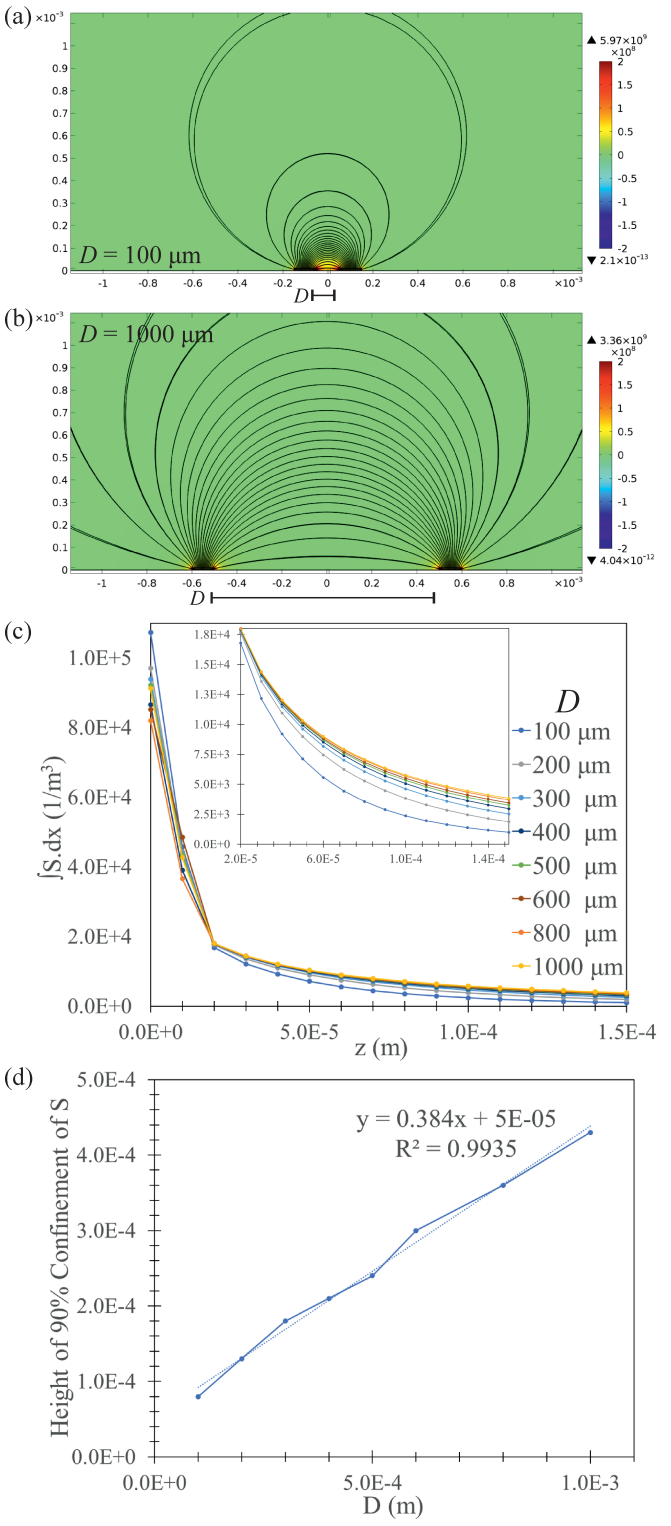

Fig. 7. Examples of the sensitivity distribution (colour map) and field lines for (a) D = 100 μm and (b) D = 1000 μm. Variation of the distance, D, between electrodes for a constant W of 100 μm and its effect on W (c) the integrated bipolar S (with respect to x) and (d) the 90% confinement height of S as a function of z.

the electrodes and the electrode/BUS interface impedance. The latter is the greatest contributor especially when the electrodes are small and at low frequencies. The middle box in Fig. 3 represents a simplified equivalent circuit model of a bipolar impedance measurement.

H. Tetrapolar Impedance Sensors

At low frequencies, tissue impedance is relatively small (Ω to kΩ range) and is thus many orders of magnitude smaller than electrode contact impedance (MΩ range). Due to the significant difference in impedance, small changes in tissue impedance may be impossible to be distinguished in bipolar measurements. Thus, if tissue needs to be measured at low frequencies, if the phenomenon being monitored is in the bulk of the volume conductor and there is no interest on electrode interface phenomena and if the absolute value of tissue impedance needs to be obtained, tetrapolar measurements are preferred. In a tetrapolar system there are four electrodes, as in Fig. 4(b). Two are used for current injection and two for voltage measurement. For the latter, a high input impedance amplifier is used and thus there is (ideally) no current flow through these electrodes and no voltage drop across the electrode interface impedance. Consequently, as opposed to bipolar measurements, the electrode interfacial impedance is not being measured together with the tissue impedance. As discussed in Section II.D1 and shown in Fig. 3, although the interface impedance is no longer measured, it is still part of the measurement system and creates challenges for the instrumentation [44], [45].

Typically for classical bioimpedance measurements electrodes are arranged on the body at specific locations based on the application (see e.g., discussions on impedance cardiography in the SI and Fig. S1). Nevertheless, in miniaturized electrode arrangements, electrodes are in the same substrate and are thus coplanar, in close proximity and often arranged either in the corners of a square [3], [100], or more often parallel to each other [12], [15], [45], [49], [91], [101], [102], although circular arrangements are also common [7], [103]–[105], as well as electrodes placed on the sides of a cube [106] and other arrangements [107].

When parallel to each other, a number of different current injection and voltage measurement arrangements can be identified. These have been investigated primarily in the field of geophysical prospecting and dc resistivity imaging and the naming used below stems from this field. The standard approach involves the injection between the outer two electrodes (A and D and in Fig. 4(b)-(c)) and measurement between the inner two (B and C). We will identify this as the Wenner/Schlumberger arrangement, although, strictly speaking these names are used for specific electrode distances, e.g., Wenner when the distance between electrodes is equal (as in the simulation in Fig. 8(a)). Alternatively, injection can take place between electrodes A and C and measurement between electrodes B and D, in what is known as the Cross arrangement, as shown in Fig. 8(b) [88]. Injection can also be performed between adjacent electrodes A and B and measurement between C and D, as shown in Fig. 8(c) [88]. This is known as the Dipole-Dipole arrangement. Choice on the arrangement and its optimization must be done based upon application requirements. Sensitivity simulations and comparison between the three arrangements have indicated

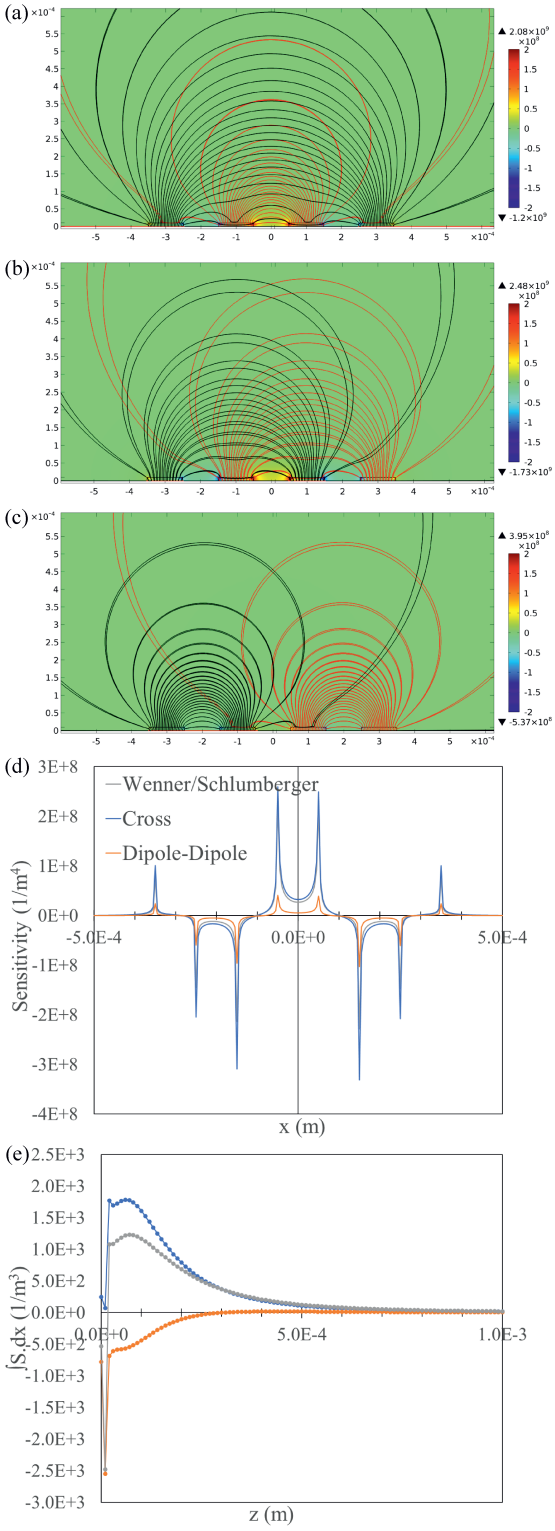

Fig. 8. Different tetrapolar injection/measurement methods stemming from the field of geophysical prospecting, when all electrodes are coplanar and parallel to each other. (a) The most common approach, known as the Wenner/Schlumberger arrangement. (b) The Cross arrangement. (c) The dipole-dipole arrangement. (d) Sensitivity along the x-axis over the plane on the top surface of the electrodes (i.e., at z = T, where T is the thickness of the electrodes, which in this example is set equal to 10 μm. (e) The integrated sensitivity with respect to x, as a function of z.

that all arrangements have positive sensitivity regions between electrodes B-C and negative between A-B and C-D, as shown in Fig. 8(d). The integrated sensitivity with respect to x as a function of z is shown in Fig. 8(e). According to these simulations, the Wenner arrangement achieves the highest sensitivity, with the steepest decrease along z. With the Wenner, the peak sensitivity is located at 60 μm and with the cross at 70 μm. The Dipole-Dipole has a negative sensitivity profile up to a depth of 300 μm. Of course, the sensitivity plot over specific points along x presents different characteristics so depending on the application a careful examination of the sensitivity over specific areas within the volume conductor should be examined [88].

1) Point Electrode Approximation: If the electrode width is much smaller than the electrode separation, thus interrogating large volumes of tissue, the electrodes can be considered as points, as in Fig. 4(c). The larger the electrode width and the smaller their separations, the less accurate this approach will be, but at least it allows an analytic mathematical expression to be obtained providing insights into the effect of electrode separation. This approach has been followed in [5], [18], [19], [108], [109]. It can be shown (see the SI for derivations) that if all four electrodes are next to each other and on the edge of a semi-infinite homogeneous conductive volume of conductivity σ, the potential difference between the two voltage measurement electrodes is equal to

$$\begin{aligned}\Delta V &= V_B - V_C = \frac{I}{2\pi\sigma} \\ &\quad \times \left(\frac{1}{D_2} - \frac{1}{D_1 + D_2} - \frac{1}{D_1 + D_2} + \frac{1}{D_2}\right) \\ &= \frac{I}{\pi\sigma}\frac{D_1}{D_2\,(D_1 + D_2)} \end{aligned} \tag{30}$$

As it can be seen from the above equation, the larger D_2 is and the smaller D_1, the greater the potential difference between the voltage measurement electrodes and thus the higher the SNR. The same approach was followed in [18], [19]. The point electrode approximation was used to establish an analytic equation for the depth of investigation. As discussed in Section III.F, this can be defined either as the depth were the sensitivity function peaks, at the median depth (50% of the total S) or higher (e.g., 80-90% of the total S). The integral of S along the x-direction can be found to be equal to [18], [19], (31), as shown at the bottom of the next page. The median depth of investigation is then [18], [19]

$$z_{median} = \frac{1}{2}\sqrt{\left|\left(\frac{D_1}{2} + D_2\right)^2 - \left(\frac{D_1}{2}\right)^2\right|}. \tag{32}$$

The first bracket is half the distance between the injecting electrodes A and D, and the second bracket is half the distance between the voltage measurement electrodes B and C. According to this simple equation, increasing the A-D separation leads to an increased depth of investigation, which is further increased by decreasing the measuring electrode separation.

2) Conformal Mapping-Based Approximation: Conformal mapping can be used as an approach to take into consideration the width of the electrodes and generate an analytic expression for the tetrapolar S. The two sets of electrodes in the tetrapolar system can each be modelled using the conformal mapping approach described earlier and in Fig. 5 for two different values of k, k_1 and k_2 as defined in (25). In this way the two reciprocal current density distributions can be obtained and through these S can be evaluated by obtaining an analytic equation for it. This is however an approximation, as the effect of the conductive electrodes of the second pair in the current density distribution and current flow is ignored. The effect of the second pair of electrodes to the current density can be seen in the streamline plots of Fig. 8(a)-(c). As the current travels close to the electrode plain and over the second pair of electrodes, their conductivity will attract the current density lines and distort the field. This effect will not be modelled by this approach, leading to deviations to E, J and S close to the electrode plain. Nevertheless, obtaining this expression allows us to gain insights into the dependence of S to the geometry of the tetrapolar coplanar and parallel electrode arrangement. This was examined in [85], [87] and the obtained equations can be found in the SI.

3) FEM: These analytic equations are useful to provide a designer insight on how the various design variables will influence the sensor response, but ultimately the FEM is the way forward to properly model all phenomena and complex geometries, which would be impossible to consider with such analytic approaches. This can be done without considering the sensitivity theorem and by simply varying the electrode geometry or arrangement and investigating the effect of frequency and conductivity/permittivity changes (e.g. of specific volumes representing specific tissue sections/types or organs based on anatomically accurate models) to the total simulated measured impedance [6], [13], [14], [107]. Nevertheless simulations of S allows us to obtain the contributions of specific volumes to the total measured impedance and provide further insights into the design of the electrode arrangement and into the interpretation of experimental results and to optimize the design of the electrode arrangement to provide higher sensitivity within tissues and volumes of interest [6], [12], [91], [102], [110], [111]. It has been found that in electrodes placed at the corners of a square, the negative sensitivity regions extend to a distance over the electrode plane equal to half the electrode distance, that S achieves a maximum value equal to 1/3 of the electrode separation and that the average sensitivity over the electrode plane is zero [90], [112]. These findings explain why tetrapolar measurements are insensitive to electrode polarization and more sensitive to tissue impedance. One approach to simplify the design process that has been followed with FEM simulations, is to keep the distance between injecting and measuring electrode constant and to a minimum allowed by the fabrication process. As the injecting and measuring electrode separation D_2 is reduced, the system approaches the characteristics of a bipolar electrode arrangement, with negative sensitivity regions gradually diminishing. This is advantageous as it reduces the effect of negative sensitivity regions that can perplex measurements and detection. By defining as a depth of investigation the 90% confinement of the total S and by keeping the separation between injecting and measuring

electrodes (D_2) constant, the depth of investigation (90%) was found in [6] to vary linearly as a function of the measuring electrode separation (D_1), with a slope of ~0.65.

As an example, here we will consider the implementation of a tetrapolar electrode system of coplanar and parallel to each other long electrodes. The electrode length is considered much larger than the electrode width and separation and the system is modelled in 2D. We set specific limits in the technology that this fictional electrode array is to be implemented with. The electrode thickness T_{elec} is set to 10 μm, and the minimum metal width and separation between different metal features is set to 100 μm. To limit negative sensitivity regions, we set $D_2 = 100$ μm, which is the minimum allowed by the resolution of this fictional fabrication technology. W is set to the minimum, 100 μm, to have a small overall device, and since W does not affect the field distribution as much as D. The only free parameter is thus $D_1 \geq 100$ μm, which is varied up to 1.4 mm. The sensitivity is calculated in Comsol and data are extracted in steps of $1e^{-5}$ m in the x and z axes for numerical integration. This is performed first with respect to x and then with respect to z per $1e^{-5}$ m to evaluate the cumulative total S as a function z and to calculate from that the percentage to the total S and thus extract the median depth of investigation and the 90% S confinement, as defined in (24). These are shown in Fig. 9. As it can be seen from Fig 9(a), with increasing D_1 the sensitivity increases in magnitude and the curve becomes wider. The peak (Fig. 9(a)) gradually moves further away from the electrode plane, as do the median (Fig. 9(b)) and 90% (Fig. 9(b)) depths. The data in Fig. 9(b)-(c) are the approximate values, as they were obtained from simulated data extracted at a relatively large step size of e^{-5} m due to the large volume of data. Comparing these with the bipolar sensitivity plots (Fig. 6(b) and Fig. 7(b)) it is clear that the S profiles of bipolar and tetrapolar arrays are significantly different. Bipolar S continuously decreases, (indicating a high sensitivity to interface phenomena), while tetrapolar S increases reaching a peak value and then it gradually decreases to zero. Depending on the application, one can thus choose a value of D_1 based on how far away from the electrode plane detection of a physiological event is to be performed. It has to be noted, that the strong sensitivities seen in the plots of Fig. 8(e) and Fig. 9(a) close to $z = 0$ are due to the effect to the current density of the first pair of electrodes from the second pair of electrodes, as due to their high conductivity they will distort the current path. These could have important implications for a particular application and point electrode approximations ignoring the thickness and material properties of the electrodes will not reveal these. It should also be highlighted, that the sensitivity plot shown here *vs* z, are integrated with respect to x. The sensitivity plots over the x-axis and at different depth are quite complex and it is recommended that these are thoroughly examined first. It should also be noted that in all sensitivity color maps the range of values displayed have been manipulated to improve the visualization of the sensitivity.

I. Focused Impedance Measurements (FIM)

Another technique that lies between four electrode measurements and electrical impedance tomography (EIT) is what is known as focused impedance measurements (FIM). The various FIM configuration proposed in the literature are summarized in Fig. 10. It was first proposed in [113] as two tetrapolar electrode arrays perpendicular to each other over a central point. The individual impedance measured by the two electrode sets for the same value of injected current are averaged to obtain a single value of impedance. FIM allows focusing and enhanced sensitivity over the central point. To calculate the S of a FIM array, the S values of the two arrays are summed. To some extent the positive S of one of the electrode arrays cancels the negative S of the second [114]. Nevertheless the two sets of voltage measurement electrodes (4 electrodes) can be replaced by two electrodes placed on equipotentials common to both arrangements, thus reducing the total electrode count to six [113], [115]. Current of the same amplitude, phase and frequency is differentially injected into the two pairs of current injecting electrodes through isolated current sources and the voltage is measured by the two voltage measurement electrodes. FIM has also been demonstrated with four electrodes located at the corner of a square, where the second group of four electrodes is obtained by shifting the connections by 90° [112], [116]. It has been found that in eight, six and four FIM systems, the peak sensitivity is located at a distance over the electrode plane of about $D_2/3$, where D_2 is the distance between injecting and measuring electrodes. Eight and six electrode FIM arrays achieve a negative sensitivity region until about $D_2/2$, while the four electrode system up to $D_2/3$ [112]. As discussed previously, as injecting and measuring electrode separation is reduced, the negative S regions are reduced as well, since the electrode arrangement approximates a bipolar arrangement. The peak sensitivity was closer to the surface for the four-electrode system followed by the eight electrode system and then by the six electrode system [112]. Increasing the injecting-measuring electrode separation demonstrated a linear relationship for all three FIM arrays for the depth location of the peak sensitivity [112]. The six-electrode FIM produces the most complex sensitivity distribution profile between these three FIM arrangements, that is also not symmetrical, making challenging the interpretation of data collected from volume conductors with complex regional variations in electrical properties [112], [117]. A different variation of FIM was discussed in [117], where eight electrodes where used, six as in the

$$\int_{-\infty}^{\infty} S.dx = \frac{32\left(\frac{D_1}{2}+D_2\right)\left(\frac{D_1}{2}\right)}{\pi\left(\left(\frac{D_1}{2}+D_2\right)^4 - 2\left(\frac{D_1}{2}+D_2\right)^2\left(\left(\frac{D_1}{2}\right)^2 - 4y^2\right) + \left(\left(\frac{D_1}{2}\right)^2 + 4y^2\right)^2\right)} \tag{31}$$

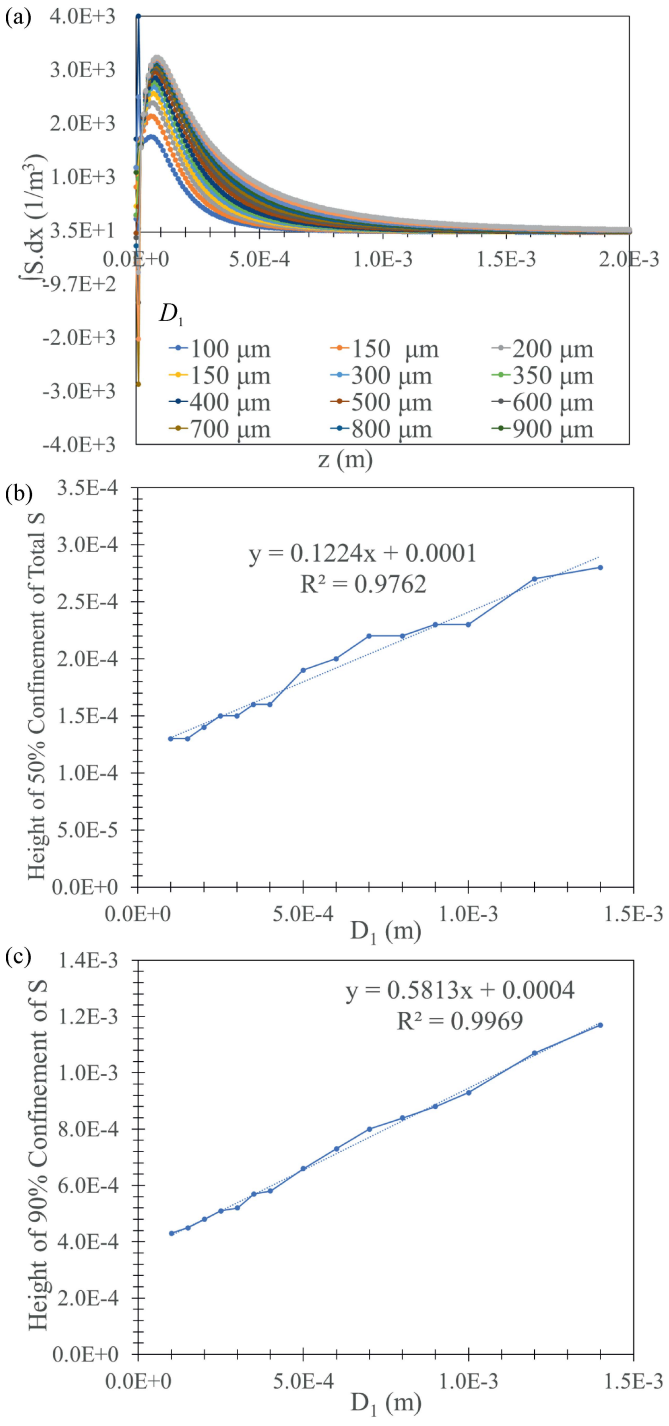

Fig. 9. In this example, the distance between injecting and measuring electrodes (D_2) is set constant and equal to 100 μm and only D_1 is varied between 100 – 1400 μm. (a) Sensitivity integrated with respect to x as a function of z. (b) Calculation of the percentage of $\int$S.dx at different heights with respect to the total sensitivity, $\int\int$S.dxdy.

six-electrode FIM, plus two more mirroring the position of the voltage measurement electrodes to balance the electrode arrangement and provide a more symmetric focused zone. In addition, the current injections between the two pairs of injecting electrodes are simultaneous and not sequential as in the other FIM arrangements, with a change in the orientation of current being injected and using a different

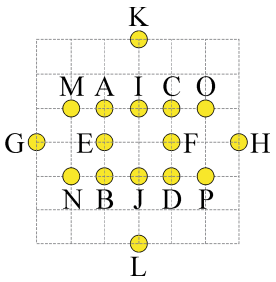

Fig. 10. Different types of FIM electrode arrangements. Adapted from [112].

TABLE I
DIFFERENT TYPES OF FIM ELECTRODE ARRANGEMENTS

Number of Electrodes	Measurement 1	Measurement 2	References
8	Inj: G H Meas: E F	Inj: K L Meas: I J	[112-114], [116]
6	Inj: G H Meas: A D	Inj: K L Meas: A D	[112], [114], [116]
4	Inj: A B Meas: C D	Inj: B D Meas: A C	[115], [116]
8	Inj: GH & KL Meas: A D	Inj: HG & KL Meas: C B	[114], [117]
6	Inj: M P Meas: E F	Inj: N O Meas: E F	[111]
5	Inj: G I Meas: E F	Inj: G J Meas: E F	[111]

set of the two potential measuring electrode sets. Both [112] and [117] found the four-electrode FIM being advantageous in terms of its sensitivity characteristics, which is further supported by the fact that it requires less electrodes than the other FIM arrangements. Various five-electrode FIMs were proposed in [111], which achieved a reduced sensitivity to motion artefacts. It has to be highlighted that the early works presented in [90], [112], [114] were obtained using the point electrode approximation and care must be taken in translating these results into other applications. The above discussions summarize the key points of FIM electrode arrays. More detailed discussions can be found in [115].

J. A Useful Tip for Simulation Verification

When doing simulations, it is always important to ensure the FEM or CM solutions and modelling approach are correct and sufficiently accurate. For example, a mesh density analysis should always be performed in FEM simulations. The mesh should be optimized to a point where changes in its density do not change significantly the solution. FEM models should be used to verify solutions obtained from simplified analytical methods (CM or point electrode approximations). The sensitivity theorem and reciprocity are useful tools to establish accuracy in tetrapolar electrode FEM simulations. The impedance value obtained by dividing the voltage difference between the two measuring electrodes and the current injected between the second electrode pair should be the same in the two reciprocal FEM solutions. These should also match the volume integral (or surface in 2D models) of the sensitivity multiplied by $1/(\sigma + j\omega\varepsilon)$ according to (S12) that also gives

the impedance, if the volume conductor is homogeneous, or with the addition of the Z's calculated with the volume (or surface in 2D models) integrals of S using (S12) in domains with different materials. Ensuring reciprocity holds in the models ensures model and solution quality with regards to mesh density and boundary conditions.

K. Electrode Recessing

It has been observed that patients undergoing electrosurgery suffered burns along the perimeter of skin-surface electrosurgical electrodes [118], [119]. Early investigations demonstrated that the current density along the surface of electrodes is highly non-uniform. It is enhanced strongly at the electrode edges, while the inner area of the electrode, towards the middle, collects significantly smaller portions of the total current [118]. In fact, 50% of the total current is collected by the outer 15% of the disk electrode [120]. This issue has also been highlighted within the field of chronic electrical stimulation in neuroprosthetics (e.g. cochlear implants) [121], [122]. In addition to tissue damage, corrosion of metal electrodes has been reported due to electrochemical reactions taking place, particularly at electrode edges, due to the higher current densities, which push the metal over its corrosion limit [121]. This also leads to cutaneous pain, erythema, and skin burns in external cardiac pacing and defibrillation, due to large temperature gradients formed at the electrode edges [121].

Of course, the above are not relevant to typical bioimpedance measurements, as small sinusoidal perturbations are used. However, they could be important in the field of affinity-based impedimetric biosensors at very low frequencies. These issues led to investigations over methods for creating more uniform current density distributions over electrode surfaces [118], [120]–[125]. It was found that by recessing the electrodes, current density uniformity along the electrode surface improved and that the greater the depth of the recess, the greater the achieved uniformity [87], [120]–[125]. Even a small recess depth of even 1/10 of the electrode diameter significantly improve the current density distribution [124], as the theoretical singularity at the electrode edge is eliminated. There is a limit to the recess depth beyond which no significant improvement can be achieved. With circular electrodes, this is approximately one third of the electrode radius [121]. Nevertheless, at the top of the recess, the current density does not remain uniform, and some peaking is present at the edges [122]. This becomes weaker with increasing recess and is similar to electrodes without a recess, but the current density is significantly reduced to safer levels. These are verified by the FEM simulations shown in Fig. 11. Indeed, as shown in Fig. 11(e) there are no significant changes in the current density profile across the electrode surface beyond recess depths of 30-40 μm for a 100 μm electrode. While current density uniformity is achieved along the electrode surface with increasing recess depth (Fig. 11(e)), at the top of the recess, current density remains non-uniform (Fig. 11(d)) and recess depths beyond 10 μm do not seem to affect it much.

To address this issue, various geometries for the sidewall of the recess (that is the geometry of the insulating material

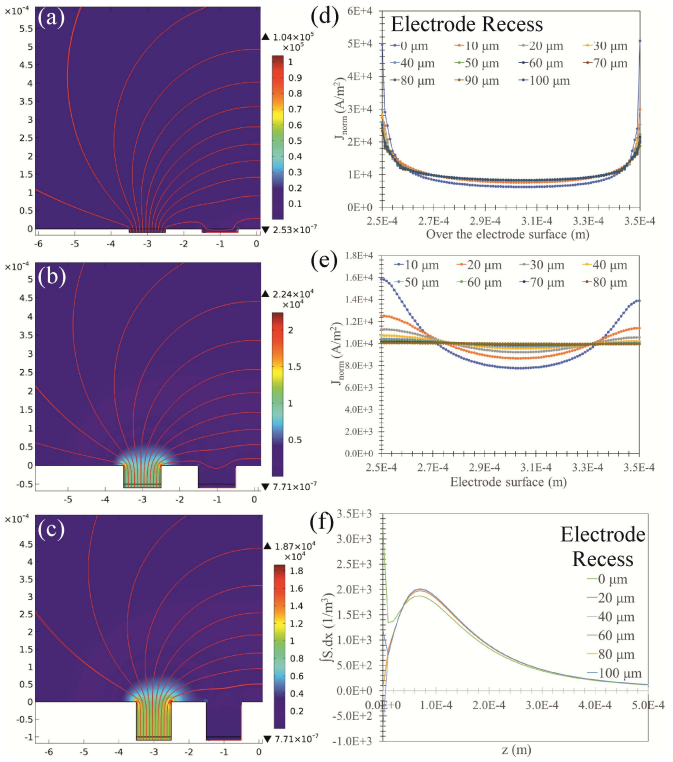

Fig. 11. Electrode recessing for more uniform current patters along electrode surfaces for stimulation electrodes. The normal component of the current density (J_{norm}) of: (a) Zero recess. Only the top part of the electrodes is in contact with the solution. (b) 50 μm recess and (c) 100 μm recess. (d) J_{norm} on the top of the recess. (e) J_{norm} along the electrode surface at the recess depth. (f) The integrated sensitivity with respect to x as a function of z for recess depth of 0 - 100 μm.

surrounding the electrode) were also examined to produce a radially varying recess. These included exponential, conical and stepwise approximation to conical recessing methodologies [122], [125]. All three allow a uniform current density profile across the electrode surface, however they generate different profiles along the top of the recess (i.e., the aperture). In the exponential recess, the current density peaks at the middle of the electrode and is minimum at the edge of the aperture. On the other hand, conically recessed electrodes allow a uniform current density at the aperture. The stepwise approximation to a conical recess leads to a complex profile approximating that of the conical recess due to the sharp edges present in the geometry, leading to a fluctuation between low and higher current densities along the aperture. A three-step recess approximates well a conical recess.

Electrode recessing is also beneficial in electrochemical sensors, allowing reduced bio-fouling due to bovine serum albumin and an extended linear range above the saturation limit of the enzyme in glucose sensors, while it also protects from mechanical damage the sensitive biosensing membranes deposited on electrodes [126]. As reported in early developments of tissue oxygen sensors, sensor performance depends on geometry and when an electrode is recessed the diffusion field is restricted to the recess [127]. Electrode recess to electrode diameter ratios of 1 or 2 can improve oxygen sensor performance and sensitivity, with ratios of 10 being a limit

to sensor improvement [128], while also improving sensor stability and reducing sensitivity to motion artefacts [129]. Another advantage of electrode recessing and the more uniform current density along the electrode surface is that more uniform electrochemical deposition will take place leading to more uniform films of e.g., Pt black, PEDOT:PSS or other materials electrochemically deposited on electrodes to e.g., reduce electrode impedance.

The disadvantage of electrode recessing is that there will be additional voltage drops through the volume conductor along the recess in all electrodes, as the electrode "access" resistance is increased [125], thus reducing the potential at the measuring electrodes and increasing the load seen by the current source, further reducing the potential sensed at the voltage measuring electrodes. To improve SNR, a greater injected current is thus needed, provided safety limits are respected, leading to higher power consumption [125]. The greater the recess the greater the "access" resistance, however, a 90° sidewall results in a greater increase of "access" resistance than a 45° sidewall [125]. In tissue applications, deeply recessed electrodes (e.g., Fig. 11(c)) make difficult for electrodes to achieve an ohmic contact with the tissue, unless a conductive medium, like a gel or solution is added. Trapped air within the recess during practical use of the electrodes will also create measurement errors. Nevertheless, as mentioned earlier, the recess depth is limited to a fraction of the electrode area, and these issues are thus not very limiting. Finally, it must be noted that manufacturing recessed electrodes, especially with an exponential recess, can be somewhat more challenging.

As discussed in the SI, in many neuroprosthetic and other applications, bioimpedance measurements are increasingly used in combination with electrical stimulation, to assess tissue damage due to chronic stimulation, electrode contact with tissue, or electrode positioning and distance to tissue, as is the case e.g. of cochlear implants [130]–[132]. It is also used to monitor the electrode-tissue contact, scar tissue and biocapsule formation around the implanted electrode array as these may limit the efficacy of the stimulation and bioimpedance monitoring allows optimization of the stimulus. Changing the current density distribution over the electrode surface, will change it also within the volume conductor, that in turn could change the sensitivity distribution. Nevertheless, according to the simulations shown in Fig. 11(f) regular electrode recess (Fig. 11(a)-(c)) does not significantly alter the sensitivity distribution in the equidistant coplanar electrode arrangement examined here. Consequently, electrode recessing could be applied to limit the previously mentioned issues related with stimulation, without altering the sensitivity distribution and the electrode array's impedimetric properties. More work is required to assess the effect of other recessing strategies discussed (radial, exponential, conical etc.) together with electrode separation and width to the sensitivity distribution.

L. The Issue of Selectivity

In impedimetric biosensors, to detect a specific biomolecule, biorecognition elements are used. Typically, antibodies, aptamers, DNA fragments or synthetic imprinted polymer-based binding sites are used, depending on the application. Thus, if methods to reduce non-specific binding have been applied, changes in measured impedance can only be due to the target molecule. This bond is highly specific, strong and largely irreversible. Consequently, these sensors are commonly disposable sensors for one-off measurements, as replenishing binding sites is challenging. The opposite is true for bioimpedance sensors. They can be used for continuous measurement and to investigate transient responses and dynamics of tissue properties and evolution, however, the measured impedance change cannot be easily contributed to a specific source. Bulk, e.g., tissue properties, are measured and variations of any of its constituents can contribute to measured impedance changes. Consequently, to pinpoint measured impedance change to variations of a specific constituent, well controlled conditions are required, where only one constituent changes. Cell cytometry is one such example, where the impedance is either that of a well-controlled solution or of cells. Alternatively, if this is not the case or possible, additional sensors must be used to corroborate impedance measurements. One example is tissue ischemia measurements where measurement of tissue pH, Na^+, K^+, lactate and glucose, as well as near infrared spectroscopy (NIRS) can be used in conjunction with bioimpedance measurements [133]–[135]. These are all non-specific indirect markers or ischemia, but together they provide a holistic analysis of tissue dynamics.

M. Recent Advancements in Bioimpedance Sensor Realization

Standard thin-film microfabrication techniques can be applied to pattern metals and polymers to create intricate sensing systems that include bioimpedance sensors that are stretchable and skin conformable [1], [16], [136]. High-resolution and high-quality devices that adhere to the skin with Van der Waals forces have been achieved [137]–[139]. However, they require complex fabrication protocols and high-cost infrastructure. Consequently, there has been a drive towards, additive, clean room-free manufacturing approaches.

Additive manufacturing approaches and unconventional novel electrode materials play a crucial role in bioimpedance sensor realization. Ink and paste formulations based on nanoparticles, nanowires, conducting polymers (e.g. PEDOT:PSS, polyaniline, polypyrrole), as well as custom conductive composites using elastomers, such as thermoplastic polyurethane (TPU) and polydimethylsiloxane (PDMS) mixed with conducting particles such as graphite, acetylene carbon black [140], [141], CNTs, liquid metals [142], silver nanowires [143] and microparticles [144], [145] can be used to print electrodes, interconnects and circuits on flexible and stretchable substrates. TPU, polyimide (PI) and polyethylene terephthalate (PET) are common substrate materials [11], as are temporary tattoo films and standard commercial transparent medical dressing films (e.g. Tegaderm, 3M, USA). With regards to elastomers, there is a wide range of options available commercially that can be exploited based on the target device characteristics, such as PDMS (Sylgard 184, Dow Corning, USA), Elastosil (Wacker Chemie AG, Germany) and Ecoflex (Smooth-On, USA). Some common examples have been compared in [146]. Such elastomers can be modified or synthesized

to demonstrate self-healing properties or good skin adhesion [147], [148]. Printing methods commonly used include inkjet [149], [150], screen [151], stencil, molding [140], [141] and extrusion-based (that we have been exploring in our Centre due to their simplicity) [152]–[154] and other 3D printing technologies [155], [156], as well as roll-to-roll contact printing approaches, such as gravure, flexographic printing [11] and transfer printing methods. Another interesting and very promising approach that we have been exploring is laser-induced graphitization of polyimide films and the transfer of the conductive structures on elastomers [157]–[159]. Laser and blade cutters/plotters (a subtractive process) can also be used to create electrode and sensor arrangements using metal, polymer and elastomer films using spring-like serpentine/horseshoe interconnect designs for stretchability [160], [161].

Hydrogels are another family of materials that are becoming increasingly important for biomedical applications with adhesive and self-healing characteristics and extreme stretchabilities and that can have insulating or conductive properties [162]. Transient materials that are bioresorbable, are another class of materials that can be used to create bioimpedance and other sensors [163]. These materials can be used to create implantable sensors that after a pre-programmed amount of time, they dissolve and are absorbed by the human body leaving no traces and causing no harm. The transience is programmed passively by material properties, such as crystallinity or material thickness for example, or actively and remotely by inducing biocompatible temperature gradients that may accelerate the process.

The use of commercial printed circuit board and flexible printed circuit technologies is another approach that has attracted interests, both for wearable sensors and point-of-care analytical devices (Lab-on-PCB) [2], [133], [134], [164]–[166]. The advantage of this technology is that an established process extensively exploiting economies of scale and scope for industrial level mass manufacturing using established design rules, materials and processes can be used to realize sensors that can be co-integrated with off-the-shelf general purpose commercially available electronic components. This allows the co-integration of sensors, electronics, and microfluidics. The choice of materials for electrodes is limited to Cu, Ag, C, and different types of Au (immersion/electroless Au, hard Au and soft Au) based upon the purity of the Au layer, its thickness and deposition method [133]. Consequently, bioimpedance sensors have been realized using this approach [6], [44], [133], as well as with emergent commercial stretchable printed circuit technologies on TPU substrates [49].

Textile electrodes for physiological monitoring is a natural evolution of clothing and thus have attracted interests. Conductive yearns, e.g. stainless steel yarn, silver-coated nylon, copper and polyamide/elastomer composites have been used to realized wearable electrodes [8], [167]. Plating, dip-coating, physical vapor deposition, polymerization of conducting polymers, knitting, weaving and embroidery, inkjet, screen, and stencil printing are used [168]–[171]. Roll-to-roll electrochemical fabrication of Ag/AgCl coated nylon yearns has been demonstrated [172], and screen and stencil printing and blade coating have been combined for wearable EIT electrode arrays on polyester fabrics [173]. Along with silver, PEDOT:PSS (with additional crosslinkers for improved properties) is playing a prominent role with textile electrodes as well [171], [174]. Of course, with textile electrode integrated into clothing, the ability of the printed electrodes to withstand multiple washing cycles for reusability is an important factor [175]. Carbonization via pyrolysis is another approach recently demonstrated with modal textiles [176].

IV. Bioimpedance Instrumentation

Of primary importance is initially a good understanding of the phenomena being studied, which then allows proper design of the bioimpedance sensor to be used. Having designed the sensor and properly characterized to obtain electrode interface impedances and range of BUS impedances to be measured, then allows the development of the necessary instrumentation, as only then are the full design specifications available for the electronics, unless these can be obtained from previous studies available in the literature. The subject of bioimpedance instrumentation is extensive and impossible to cover in a tutorial together with sensor design and electrodes. There have been a few reviews on general instrumentation, discrete and CMOS current sources, front-end design and signal processing methods that the interested reader is referred to for more detailed discussions [23], [27], [177]–[181]. Bioimpedance instrumentation can thus be made wearable, portable and implantable, while also allowing integration into flexible embodiments [4], [182]–[184].

A bioimpedance system is typically composed of a voltage signal excitation (Fig. 12(c)-(f)), a voltage to current converter that connects to the current injection electrodes of the bioimpedance sensor (Fig. 14), a voltage measurement front-end connected to the relevant electrodes of the sensor (Fig. 15), followed by back-end processing of the recorded signal, in the analog or digital domains. Instrumentation can be developed using individual blocks using commercially available chips, but there are also complete impedimetric commercial chip solutions. Alternative, full-custom CMOS chip design can be exploited to create optimized and miniaturized application-specific solutions.

A. Voltage Excitation

Depending on the application and the dynamics of the tissue or phenomenon under investigation, single frequency (Fig. 12(c)), swept frequency or simultaneous multifrequency excitations (Fig. 12(d)-(f)) can be used. Most common is the swept frequency measurements, useful for applications where the time to complete the measurements serially within the bandwidth of interest is not an issue. Frequencies linearly or logarithmically distributed with a constant amplitude are used. Benchtop signal generators [185], data acquisition cards with analog outputs [2], microcontrollers, field programmable analog arrays (FPGA) [186], direct digital synthesis (DDS) [6] chips and phased-locked loops [183] can be used. High-speed analog-to-digital (DAC) converters are needed, additional filtering, a large memory and control circuits to implement digital solutions. Digital approaches may require lookup tables,

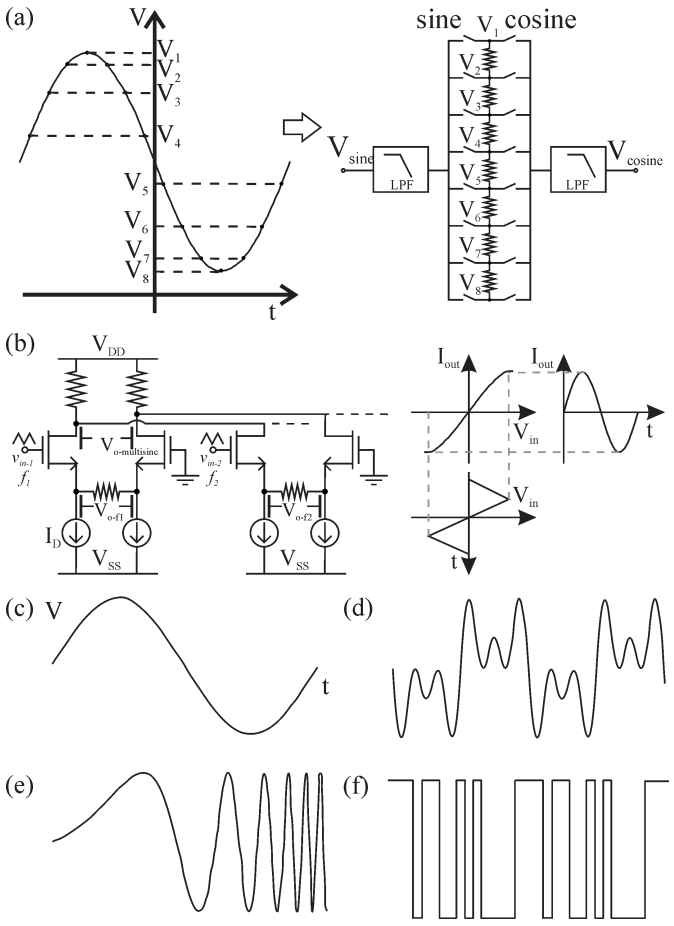

Fig. 12. (a) Tapped resistor chain for sine wave approximation and the generation of quadrature signals. Adapted from [190]. (b) Exploiting the non-linear transfer function of a differential pair in weak inversion and the conversion of a triangular wave into a sine wave, as illustrated also by the plots on the right. Current-mode addition of the output currents of multiple transconductors driver by different frequency signal to create a multisine. Adapted from [192]. (c)-(f) Different types of voltage excitations for driving the VCCS (V vs. t). (c) Sine wave for single frequency at a time measurement. (d)-(f) Multifrequency excitations: (d) Multisine of 3 frequencies. Adapted from [192] (e) Chirp. Adapted from [185] (f) Pseudo-random binary sequence.

polynomial methods, interpolation, recursive oscillators and infinite/finite impulse response filters [187]–[189]. Alternatively, an unevenly tapped resistor chain can be used to approximate a sinusoidal waveform by switching between taps. With appropriate switching, quadrature signals can be generated for synchronous demodulation front-ends (described in Section V.C) [190]. This is illustrated in Fig. 12(a). A tunable low-pass filter (LPF) is required tuned to the required output frequency to filter the signal. On the other hand, analog implementations using programmable sinewave oscillators [191] or wave-shaping circuits that use non-sinewave oscillators and non-linear circuits [178], [192] (e.g. Fig. 12(b)) or filtering [193], [194] can often lead to lower-power consumption and smaller footprint solutions.

For multifrequency signal generation, useful in applications where the dynamic transience of the phenomenon being monitored is important (e.g., flow cytometry, heart and lung monitoring), the overall multifrequency signal amplitude needs to be within safety limits, while ensuring a satisfactory SNR and a low crest factor (CR). CR is defined as the ratio of the signal's peak value and its root mean square (RMS). Multi-sine (Fig. 12(d)), chirp (essentially a swept sine excitation, Fig. 12(e)), pseudo-random binary sequences (Fig. 12(f)) such as maximum length binary sequence (MLBS) and discrete interval binary sequence (DIBS) and Walsh functions have been proposed as multifrequency excitation signals [185], [195]. MLBS can be very easy to generate, but the amplitude of each frequency component decreases with increasing frequency and thus also the SNR, while also containing frequency components that may not be of interest. DIBS allows most of the energy to be distributed within the frequency range of interest. Multi-sine signals can achieve the greatest flexibility and lead to the highest SNR, when compared to chirp and MLBS, and together with DIBS lead to the most accurate measurements, according to [185]. Nevertheless, multisine signals can be more challenging to generate. One approach, suitable for CMOS realization is illustrated in Fig. 12(b). This circuit exploits the non-linearities of CMOS differential pairs operating in weak inversion to convert a triangular wave into a sine wave. Using multiple such circuits, sinewaves of different frequencies can be generated. The output currents of these transconductors can be summed at a common node to create a multisine signal, while the voltage across the source degeneration resistor provides a single frequency signal.

B. AC Current Sources

The maximum allowable current amplitude injected into tissue is a function of frequency and has been defined as 100 μA from 0.1 Hz to 1 kHz, 100f μA from 1 to 100 kHz, and 10 mA for frequencies greater than 100 kHz, where f is the frequency in kHz, [10]. A voltage controlled current source (VCCS) is commonly used, which ideally has an infinite (i) output voltage compliance and (ii) output impedance throughout the bandwidth and (iii) no non-linearities. If (i) is not high enough for the required current and the given tissue impedance at that frequency, a distorted signal will be injected into the tissue. If (ii) is not high enough relevant to the tissue impedance, the amplitude of the injected current will not be what was intended. This is also true for (i). (i) and (ii) will lead to additional harmonic content that can include frequencies of interest, leading to erroneous estimation of the impedance. The output current, provided that the output impedance of the current source is sufficiently high, will be defined by the transconductance of the VCCS and the input voltage signal amplitude. Consequently, tunning of the output current (e.g., via feedback to ensure constant current amplitude into the tissue irrespective of load and output impedance) can be accomplished by tuning (or regulating in closed-loop) either of these. An output impedance significantly greater than the load impedance (electrode contact impedance plus tissue impedance and parasitics) at each frequency should be maintained within the bandwidth of interest. This ensures that the amplitude of the injected current has the intended value and that it is known. This removes the need for measuring the current.

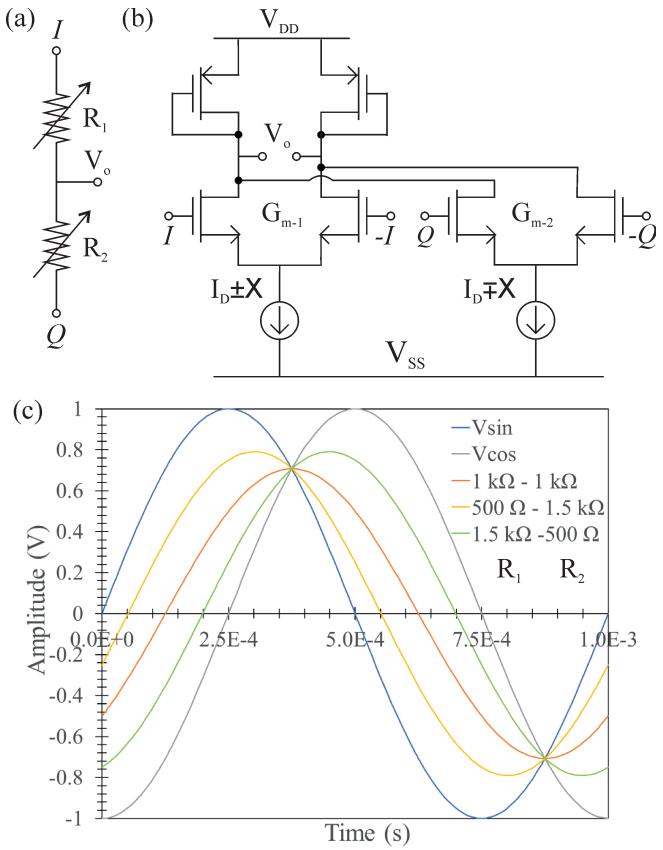

Fig. 13. (a) A voltage divider with quadrature waveforms (I and Q) applied across its terminals. (b) The capacitorless programmable phase delay circuit proposed in [198] based on (a), that uses two quadrature input signals and two transconductors to emulate a potential divider. (c) Simulated waveforms using (a) and LTSpice for different resistor ratios.

The phase relationship between measured and injected signal can be important for impedance calculation (e.g. in synchronous detection front-ends, see Section V.C below) and thus the phase delay of the VCCS can lead to impedance computation errors [196]. This phase delay can either be compensated within the VCCS [197] or at the voltage front-end electronics performing the computations, if the phase delay at a particular frequency is known [192], [198]. This will indeed be the case and a circuit such as the programmable capacitorless phase delay circuit of Fig. 13 can be used. This circuit is formed by two transconductors with their output currents summed at a common node. Each transconductor is a programmable resistor and the two are connected in series, emulating two potentiostats, as in Fig. 13(a). Application of two quadrature sinewave signals, which will typically be available in a synchronous detection front-end (as discussed in Section IV.C below), at each transconductor and increasing and decreasing the transconductance of each by the same amount leads to the tunning of the output sinewave phase and a reduction in amplitude, as shown in the LTSpice simulations of Fig. 13(c) using the circuit of Fig. 13(a). The latter is not an issue, as for demodulation at the front-end, square waves are typically used, obtained by comparators. Tunning is achieved through the tail currents of the two transconductors. The input

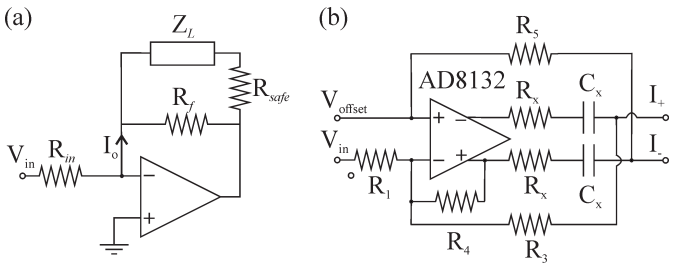

Fig. 14. (a) Load-in-the-loop VCCS [199]. (b) The enhanced Howland differential VCCS proposed in [195].

differential pairs can be designed to operate in weak inversion to allow a linear relationship between transconductance and current. The VCCS phase delay increases with frequency and thus the high frequency performance of the phase delay circuit is important, so as to not introduce additional phase delays.

Measurement of the current through sense resistors at the output of the current source is an approach to ensure the injected current amplitude is known and that the appropriate reference signal is used for impedance (phase) calculations. Differential current sources are preferred when possible, to minimize the common-mode voltage across the load and thus improve the instrumentation's overall common-mode rejection ratio (CMRR) [6], [195]. Decoupling capacitors (C_X = 1-10 μF, see Fig. 14(b)) are used for safety purposes at the VCCS outputs to block dc current into the tissue. The differential dc voltage across the current source terminal should be zero. Load-in-the-loop [199] and differential Howland current sources [6], [180], [195], [200] are the most common approaches when using discrete components, while for integrated realizations, operational transconductance amplifiers (OTA) with feedback through current sense resistors to regulate the injected current are often used [177], [201], [202]. In the load-in-the-loop configuration, the tissue (Z_L) is connected to the amplifier output through a small resistor R_{safe} and the virtual ground of the inverting terminal, as shown in Fig. 14(a). The load is thus floating. As opposed to the Howland circuit, the output impedance of the circuit is not based on resistor matching. R_f, R_{safe} and R_{in} contribute to the output impedance of the circuit, as defined in [199]. The injected current is defined by the ratio of the input voltage, V_{in}, and R_{in}. Another VCCS circuit known as the enhanced Howland current source, implemented with a fully differential amplifier, is shown in Fig. 14(b). The following relationships must be satisfied: $R_4 = R_x + R_3$ and $R_3 = R_5$. The output current is then set by [195]

$$I_O = \frac{(R_4 + 2R_1)\, V_{offset} - R_4 V_{in}}{R_1 R_x}. \tag{33}$$

An interesting observation from the previous discussions and the electrode arrangements examined, is that as electrode separation increases in bipolar arrangements, the volume being probed and also the impedance being measured increase. Since reciprocity applies, measurements can be performed using the outer pair and injection using the inner pair of electrodes to relax instrumentation requirements. This is since the load seen by the current driver between the inner pair of electrodes will

be smaller. This is beneficial for the current source and its output impedance but also for the voltage compliance requirements. Depending on the contact impedances and electrode distances, these could have an appreciable impact.

C. Voltage Front-Ends

The current injected will create a potential difference across the voltage measurement electrodes. Electrodes are related to an open-circuit dc potential due to their interfacial double layer that can be large in value and can thus saturate the voltage amplifier at the front-end. Decoupling capacitors are thus often used, as in Fig. 15(c). The IA should have a CMRR above 90 dB within the bandwidth of interest, e.g. 1 MHz [56]. In integrated implementations computation of the impedance is often implemented in the analog domain.

1) Magnitude/Phase Measurement: As discussed previously impedance can be described as a magnitude and phase. The former can be simply calculated by measuring the recorded voltage amplitude (using a peak detector or rectification and low-pass filtering) and dividing this with the known injected current (Ohm's law). The latter can be calculated by comparing the phase delay between the measured and the injected (e.g., measured through a current sense resistor to avoid delays of the VCCS and thus measurement errors) signals with a phase detector. If these signals are square waves this can be implemented using an XOR gate, an SR-latch or a switch-based multiplier (chopper) [181], [203]. This is illustrated in Fig. 15(a). A disadvantage of this approach is that the two measurement channels are different, while the nature of the output signals is also different (the magnitude is a dc voltage, while the phase is given by a pulse width, necessitating additional processing). Significant work has been done towards digitizing and further processing the phase channel [204]–[206]. The AD8302 gain/phase chip (Analog Devices, USA) can be used with additional circuitry, as a magnitude/phase measurement front-end [207].

2) Synchronous Sampling: A time-based method based on sampling is synchronous sampling [24]. As the signal injected and its frequencies are known, a discrete Fourier transform is not necessary [24]. Sampling the measured signal at the time points were the injected signal is zero and maximum, allows the calculation of the real and imaginary parts of the impedance, respectively, using a single channel [24], [208]. Doing so at both half-cycles of the recorded signal and averaging the measurements allows elimination of the voltage offset in the measurement channel [24]. This is shown in Fig. 15(b). The high-pass filter (HPF) removes low-frequency noise and other interfering signals that may be detrimental for the subsequent sample and hold (S/H) step. In [24] this was extended to multifrequency signals. Sampling at accurate time-points and generating the signals to do so can be challenging, particularly at high frequencies.

3) Synchronous Demodulation: The most popular approach is known as synchronous demodulation where the recorded signal is multiplied by an in-phase and a quadrature copy of the injected signal to obtain the real and imaginary component following low-pass filtering, as shown in Fig. 15(c). The example waveforms shown are those obtain when the load is purely resistive, in which case, the filtered (averaged) output of the Im(Z) channel is equal to zero. The signal in this way is demodulated to dc. If this is performed before amplification, it relaxes the requirement of the IA with regards to CMRR and bandwidth, but requires the amplifier offsets to be compensated for. This can be done as in [196] by using chopping to modulate the dc offset of the amplifier at a frequency beyond the passband of the recording channel; as proposed in [209], chopping and demodulation signals can be combined in the first multiplication step. In addition, the filtering function can be part of the amplifier, resulting to a compact implementation. Demodulation and filtering essentially lead to a high-quality bandpass filter characteristic and thus frequency selection. When transient phenomena are studied, the settling time of the filters used may need to be considered. Multi-channel implementations allow simultaneous computation of real and imaginary components at multiple frequencies [196]. Nevertheless, system complexity, power consumption and size will increase. Accurate matching between the two channels is needed, however both channels are the same and thus the realization of this approach is simpler than others (e.g., magnitude/phase).

4) Oscillation-Based Test: Another instrumentation approach involves the use of the bioimpedance being measured as the impedance defining the oscillation frequency of an oscillator. This has been implemented both with discrete components [210], [211] and in custom CMOS [212], for the monitoring of cell cultures using two-point measurements. The frequency and amplitude of the generated signal depend on the bioimpedance [210], [211], while magnitude and phase information can also be extracted [212]. A bandpass filter, a comparator and a circuit interfacing with the bioimpedance (a current source [211], [212] or an operational amplifier, OA [210]) can be used, arranged in positive feedback, as in Fig. 15(d). R_{in} ensures the current flowing into the bioimpedance is in acceptable levels.

5) Bridge-Based Methods: Most benchtop instruments operate using the bridge-based method. This can be implemented with analog, digital and mixed signal approaches [213]–[215]. The basic operation relies on the half-bridge, comprised of the impedance being measured (Z_x) connected in series with a known impedance, typically a resistance (R_{kn}). A known signal (V_{kn}) is applied at the load to be measured and a second signal (V_{tune}) at the known load. If the currents flowing through the two loads are not equal, an imbalance voltage, V_e, appears at their common terminal. This signal can be used to adjust the voltage signal (amplitude and phase) applied to the known load (illustrated in Fig. 15(e) with an orange arrow). When $V_e = 0$ V, then $V_{kn}/Z_x = V_{tune}/R_{kn}$ [214]. Alternatively, V_e can be used to adjust the value of R_{kn} (e.g. a digital potentiostat) to force the error voltage to zero (illustrated in Fig. 15(e) with a red arrow), while in another approach, the error signal can be subtracted by a programmable signal set via feedback to force the output to zero [213], [215].

6) Amplitude-to-Time Conversion: An alternative measurement approach involves the use of amplitude-to-time conversion (Fig. 15(f)). In this way both magnitude and phase can

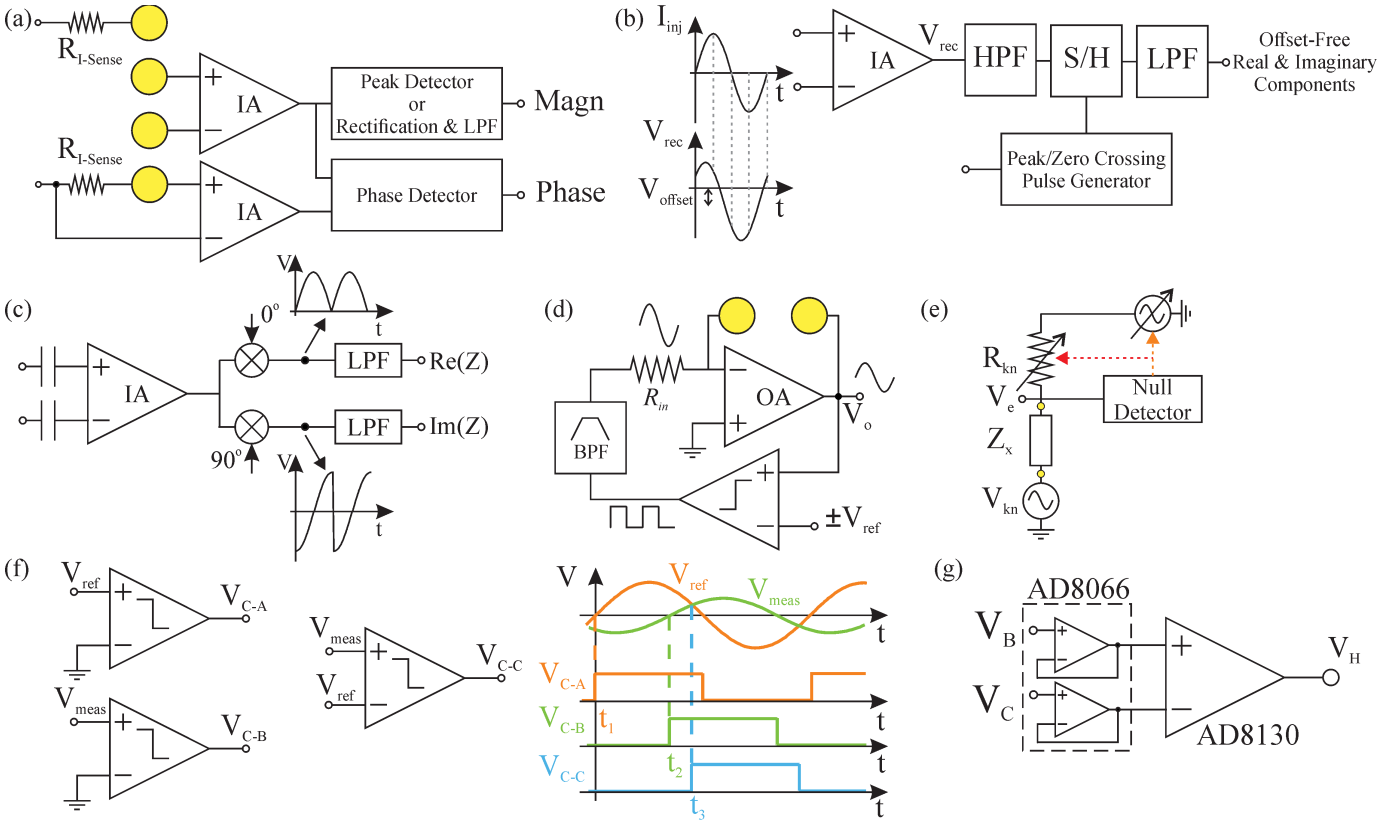

Fig. 15. Front-end architectures: (a) Magnitude/phase measurement front-end [181]. (b) Synchronous sampling [24]. (c) Synchronous demodulation for the calculation of Re(Z) and Im(Z) [196]. (d) Oscillation-based topology [210]. (e) The half-bridge method [213]–[215]. (f) Amplitude-to-time conversion [216], [217]. (g) The front-end amplifier for tetrapolar impedance measurements with benchtop impedance analyzers proposed in [45].

be time signals [27], [216]. Signals of different amplitude intercept a reference signal of the same frequency at different times. This time delay can be computed by comparators to realize a simple and low power front-end [216]. Comparator A and B convert the reference and the measured sinewaves into square waves, respectively. These two can then be compared as in Fig. 15(a) to obtain the phase, using e.g. a counter-based zero-crossing check and methods discussed in [217] to improve phase measurement accuracy. Comparator C detects the intercepts of the reference and measured waveforms. The time difference between comparator A and C output square waves is proportional to the amplitude of the measured voltage. More recently the same approach was implemented in [217].

7) Linear System Identification: In this approach, the measurement of the bioimpedance is treated as an optimization problem based on adaptive filtering, which is solved by finding the minimum of a cost function [218]. The cost function is defined as the least square error between the response of a model and the measured bioimpedance. Its minimum represents the optimal filter coefficients, which correspond to an equivalent bioimpedance transfer function [218].

8) Other Digital Approaches: In addition to the above, digitization following voltage measurement and amplification can be used to process the signal and obtain the impedance in the digital domain. Digital implementations of synchronous detection can be implemented, using e.g. microcontrollers [219], but most commonly, the Fourier transform is used, e.g. using undersampling [220]. Another approach is based on the Groetzel filter [221]–[223]. This essentially converts the discrete time Fourier transform (DTFT) equation into a recursive filter, that can be implemented by a second order infinite impulse response structure that is split into two parts [221]. The first is the recursive part with one real multiplication and the second a feedforward path with one complex multiplication. The latter is split into two real parts, requiring two multiplications. This allows computation of the Fourier coefficients simultaneously with sampling and thus no samples need to be stored and no delays are added [221]. When compared to digital synchronous detection, there is no need to store full sine and cosine cycles for the demodulation and only three coefficients per bin are needed (one for the recursive part and two for the feed-forward part, i.e., for the real and imaginary parts).

9) A Note on Impedance Analyzers: Impedance analyzers are powerful tools for the measurement and characterization of electronic components, such as resistors, capacitors and inductors, which are two terminal devices with infinitesimal contact impedances involved when being measured (metal to metal connections). Such instruments are typically available in electronics laboratories and can be essential for characterizing bioimpedance sensors, tissues and physiological phenomena and thus for obtaining design specifications for electronics development. When using commercial benchtop impedance analyzers, it is important to investigate, whether the instrument can perform accurate tetrapolar impedance measurements.

Instruments such as E4990A (Keysight, USA) 6500B (Wayne Kerr Electronics, UK) and 1260A (Solartron Analytical, USA) using the balancing bridge method for measurement, cannot achieve good measurement accuracy when there are large contact impedances, as is the case in bioimpedance applications. To circumvent this, additional front-end amplifiers can be used, and a few solutions have been proposed in the literature. These and other topologies, were recently proposed and compared in [45]. A gain of 1 V/V is typically used and the amplifier bandwidth, phase delay, noise and CMRR of the amplifier are essential to ensure low measurement error. The L_{cur} and L_{pot} terminals of the instrument are shorted together and the amplifier output is connected to the H_{pot} terminal. The solution proposed for this in [45], is shown in Fig. 15(g). Solartron Analytical have a commercially available solution to mitigate this issue, the 1294 Impedance Interface, which however limits the instruments bandwidth.

D. Commercial Single Chip Solutions

There are two main single chip solutions that can be used for bioimpedance measurements. One involves the use of AD5933 (Analog Devices, USA), which however requires additional circuitry (primarily a VCCS) and is limited to 100 kHz [224]–[226]. The other is the AFE4300 (Texas Instruments, USA), that may not need a VCCS but needs a number of passive components and is limited to 80 kHz as it is originally designed for bioimpedance analysis (BIA) weight scales [227], [228]. Both chips use a DDS. A third solution is the MAX30002 (Maxim Integrated, USA) that goes up to 130 kHz. Another single chip solution is the AD5940 and AD5941 that can be used both for impedimetric electrochemical sensing and bioimpedance measurements up to 200 kHz, but use a voltage excitation requiring thus a VCCS similarly to AD5933. Chips for electrocardiogram measurement that have the capability for respiration measurement, such as the ADAS1000 (Analog Devices, USA) perform the latter through bioimpedance measurements and can thus also be used. Another approach involves the magnitude and phase measurement chip AD8302 (Analog Devices, USA) with a bandwidth in the GHz range, that can be used as proposed in [207] for bioimpedance measurements.

V. Conclusion

Electrical bioimpedance is a powerful noninvasive technique for characterizing tissue and monitoring the evolution of their parameters over time. The technique has found application in a wide variety of biomedical applications. Bioimpedance sensor design must be optimized based on the requirements of the application. Typically, bipolar or preferably tetrapolar impedance measurements are used. The latter allows eliminating from the measured impedance contributions from the electrode/tissue interface impedances that dominate the measured impedance at low frequencies and when small electrodes are used. Proper electrode design entails the use of analytical or numerical simulations for the optimization of the geometry and arrangement of the electrode system used and consequently of the electric field distribution generated within the biosample. The sensitivity theorem plays an important role in this direction.

In contrast to other physiological monitoring techniques requiring the measurement of electrophysiological signals or dc measurements of voltage or current, instrumentation design is more complex as ac measurement are required over a wide frequency range. In addition, a known excitation signal needs to be generated and injected into the biosample. Impedance is a complex number, with magnitude and phase, or equivalently a real and an imaginary component and thus methods of computing these are also required. When the output signals are DC voltages, care must be taken to eliminate any voltage offsets.

A disadvantage of electrical bioimpedance is that many different processes in tissues or even the electrode contact (particularly for bipolar measurements), can contribute to the measured impedance. Simply put, it lacks specificity. Nevertheless, it has tremendous potential in the field of multiparametric physiological monitoring devices, particularly for wearable but also for implantable applications, where impedance measurements can corroborate other measurements, such as, e.g., in tissue ischemia detection, where other measurands (e.g., pH, Na^+, K^+, lactate, oxygen) can also indirectly indicate its onset and evolution.

Acknowledgment

The author would like to thank N. P. Agkyridou for language editing of the manuscript, S. M. Kassanou for the motivation, and A. Demosthenous and R. Bayford for introducing him to the field of electrical bioimpedance.

References

[1] X. Huang *et al.*, "Epidermal impedance sensing sheets for precision hydration assessment and spatial mapping," *IEEE Trans. Biomed. Eng.*, vol. 60, no. 10, pp. 2848–2857, Oct. 2013, doi: 10.1109/TBME.2013.2264879.

[2] A. I. Sunny *et al.*, "Feasibility experiments to detect skin hydration using a bio-impedance sensor," in *Proc. 41st Annu. Int. Conf. IEEE Eng. Med. Biol. Soc. (EMBC)*, Jul. 2019, pp. 6032–6035, doi: 10.1109/EMBC.2019.8857470.

[3] S. Abdul, B. H. Brown, P. Milnes, and J. A. Tidy, "The use of electrical impedance spectroscopy in the detection of cervical intraepithelial neoplasia," *Int. J. Gynecol. Cancer*, vol. 16, no. 5, pp. 1823–1832, 2006, doi: 10.1111/j.1525-1438.2006.00651.x.

[4] Y. Wu, D. Jiang, A. Bardill, S. de Gelidi, R. Bayford, and A. Demosthenous, "A high frame rate wearable EIT system using active electrode ASICs for lung respiration and heart rate monitoring," *IEEE Trans. Circuits Syst. I, Reg. Papers*, vol. 65, no. 11, pp. 3810–3820, Nov. 2018, doi: 10.1109/TCSI.2018.2858148.

[5] A. Ivorra *et al.*, "Minimally invasive silicon probe for electrical impedance measurements in small animals," *Biosens. Bioelectron.*, vol. 19, no. 4, pp. 391–399, Dec. 2003, doi: 10.1016/S0956-5663(03)00204-5.

[6] P. Kassanos, H. M. D. Ip, and G.-Z. Yang, "A tetrapolar bio-impedance sensing system for gastrointestinal tract monitoring," in *Proc. IEEE 12th Int. Conf. Wearable Implant. Body Sensor Netw. (BSN)*, Jun. 2015, pp. 1–6, doi: 10.1109/BSN.2015.7299403.

[7] J. Wtorek, L. Jozefiak, A. Polinski, and J. Siebert, "An averaging two-electrode probe for monitoring changes in myocardial conductivity evoked by ischemia," *IEEE Trans. Biomed. Eng.*, vol. 49, no. 3, pp. 240–246, Mar. 2002, doi: 10.1109/10.983458.

[8] J. Ferreira, I. Pau, K. Lindecrantz, and F. Seoane, "A handheld and textile-enabled bioimpedance system for ubiquitous body composition analysis. An initial functional validation," *IEEE J. Biomed. Health Informat.*, vol. 21, no. 5, pp. 1224–1232, Sep. 2017, doi: 10.1109/JBHI.2016.2628766.

[9] A. McEwan, G. Cusick, and D. S. Holder, "A review of errors in multi-frequency EIT instrumentation," *Physiological Meas.*, vol. 28, no. 7, pp. S197–S215, Jul. 2007, doi: 10.1088/0967-3334/28/7/S15.

[10] W. R. B. Lionheart, J. Kaipio, and C. N. McLeod, "Generalized optimal current patterns and electrical safety in EIT," *Physiol. Meas.*, vol. 22, no. 1, p. 85, 2001, doi: 10.1088/0967-3334/22/1/311.

[11] C. Mc Caffrey, J. Flak, K. Kiri, and P. Pursula, "Flexible bioimpedance spectroscopy system for wound care monitoring," in *Proc. IEEE Biomed. Circuits Syst. Conf. (BioCAS)*, Oct. 2019, pp. 1–4, doi: 10.1109/BIOCAS.2019.8919095.

[12] S. B. Rutkove, A. Pacheck, and B. Sanchez, "Sensitivity distribution simulations of surface electrode configurations for electrical impedance myography," *Muscle Nerve*, vol. 56, no. 5, pp. 887–895, Nov. 2017, doi: 10.1002/mus.25561.

[13] M. Jafarpoor, J. Li, J. K. White, and S. B. Rutkove, "Optimizing electrode configuration for electrical impedance measurements of muscle via the finite element method," *IEEE Trans. Biomed. Eng.*, vol. 60, no. 5, pp. 1446–1452, May 2013, doi: 10.1109/TBME.2012.2237030.

[14] L. L. Wang, M. Ahad, A. McEwan, J. Li, M. Jafarpoor, and S. B. Rutkove, "Assessment of alterations in the electrical impedance of muscle after experimental nerve injury via finite-element analysis," *IEEE Trans. Biomed. Eng.*, vol. 58, no. 6, pp. 1585–1591, Jun. 2011, doi: 10.1109/TBME.2011.2104957.

[15] T. Süselbeck *et al.*, "*In vivo* intravascular electric impedance spectroscopy using a new catheter with integrated microelectrodes," *Basic Res. Cardiol.*, vol. 100, no. 1, pp. 28–34, Nov. 2004, doi: 10.1007/s00395-004-0501-8.

[16] L. Klinker *et al.*, "Balloon catheters with integrated stretchable electronics for electrical stimulation, ablation and blood flow monitoring," *Extreme Mech. Lett.*, vol. 3, pp. 45–54, Jun. 2015, doi: 10.1016/j.eml.2015.02.005.

[17] P. Kassanos *et al.*, "Smart sensing for surgery: From tethered devices to wearables and implantables," *IEEE Syst., Man, Cybern. Mag.*, vol. 6, no. 3, pp. 39–48, Jul. 2020, doi: 10.1109/MSMC.2019.2963455.

[18] P. Linderholm, T. Braschler, J. Vannod, Y. Barrandon, M. Brouard, and P. Renaud, "Two-dimensional impedance imaging of cell migration and epithelial stratification," *Lab Chip*, vol. 6, no. 9, pp. 1155–1162, 2006, doi: 10.1039/B603856E.

[19] P. Linderholm, L. Marescot, M. H. Loke, and P. Renaud, "Cell culture imaging using microimpedance tomography," *IEEE Trans. Biomed. Eng.*, vol. 55, no. 1, pp. 138–146, Jan. 2008, doi: 10.1109/TBME.2007.910649.

[20] D. Holmes and H. Morgan, "Single cell impedance cytometry for identification and counting of CD4 T-cells in human blood using impedance labels," *Anal. Chem.*, vol. 82, no. 4, pp. 1455–1461, Feb. 2010, doi: 10.1021/ac902568p.

[21] A. Ivorra and B. Rubinsky, "*In vivo* electrical impedance measurements during and after electroporation of rat liver," *Bioelectrochemistry*, vol. 70, no. 2, pp. 287–295, May 2007, doi: 10.1016/j.bioelechem.2006.10.005.

[22] S. Grimnes and O. G. Martinsen, *Bioimpedance and Bioelectricity Basics*, 1st ed. Suffolk, U.K.: Academic, 2000.

[23] P. Kassanos, S. Anastasova, and G.-Z. Yang, "Electrical and physical sensors for biomedical implants," in *Implantable Sensors and Systems: From Theory to Practice*. Cambridge, U.K.: Springer, 2018, pp. 99–195, doi: 10.1007/978-3-319-69748-2_3.

[24] M. Min, T. Parve, A. Ronk, P. Annus, and T. Paavle, "Synchronous sampling and demodulation in an instrument for multifrequency bioimpedance measurement," *IEEE Trans. Instrum. Meas.*, vol. 56, no. 4, pp. 1365–1372, Aug. 2007, doi: 10.1109/TIM.2007.900163.

[25] C. Gabriel, S. Gabriel, and E. Corthout, "The dielectric properties of biological tissues: I. Literature survey," *Phys. Med. Biol.*, vol. 41, no. 11, p. 2231, 1996, doi: 10.1088/0031-9155/41/11/001.

[26] O. G. Martinsen, S. Grimnes, and H. P. Schwan, "Interface phenomena and dielectric properties of biological tissue," in *Encyclopedia of Surface and Colloid Science*. New York, NY, USA: Marcel Dekker, 2002, pp. 2643–2652.

[27] D. Naranjo-Hernández, J. Reina-Tosina, and M. Min, "Fundamentals, recent advances, and future challenges in bioimpedance devices for healthcare applications," *J. Sensors*, vol. 2019, pp. 1–42, Jul. 2019, doi: 10.1155/2019/9210258.

[28] S. Srinivasan, "Electrode/electrolyte interfaces: Structure and kinetics of charge transfer," in *Fuel Cells: From Fundamentals to Applications*, S. Srinivasan, Ed. Boston, MA, USA: Springer, 2006, pp. 27–92, doi: 10.1007/0-387-35402-6_2.

[29] P. Pham, M. Howorth, A. Planat-Chrétien, and S. Tardu. (2007). *Numerical Simulation of the Electrical Double Layer Based on the Poisson-Boltzmann Models for AC Electroosmosis Flows*. Grenoble, France. Accessed: Dec. 17, 2020. [Online]. Available: https://www.academia.edu/1964782/Numerical_Simulation_of_the_Electrical_Double_Layer_Based_on_the_Poisson_Boltzmann_Models_for_AC_Electroosmosis_Flows

[30] W. Franks, I. Schenker, P. Schmutz, and A. Hierlemann, "Impedance characterization and modeling of electrodes for biomedical applications," *IEEE Trans. Biomed. Eng.*, vol. 52, no. 7, pp. 1295–1302, Jul. 2005, doi: 10.1109/TBME.2005.847523.

[31] M. Khademi and D. P. J. Barz, "Structure of the electrical double layer revisited: Electrode capacitance in aqueous solutions," *Langmuir*, vol. 36, no. 16, pp. 4250–4260, Apr. 2020, doi: 10.1021/acs.langmuir.0c00024.

[32] E. Barsoukov and J. R. Macdonald, *Impedance Spectroscopy: Theory, Experiment, and Applications*. Hoboken, NJ, USA: Wiley, 2018.

[33] A. J. Bard and L. R. Faulkner. *Electrochemical Methods: Fundamentals and Applications*. Accessed: Jan. 25, 2016. [Online]. Available: http://eu.wiley.com/WileyCDA/WileyTitle/productCd-0471043729.html

[34] A. Hassibi, R. Navid, R. W. Dutton, and T. H. Lee, "Comprehensive study of noise processes in electrode electrolyte interfaces," *J. Appl. Phys.*, vol. 96, no. 2, pp. 1074–1082, Jul. 2004, doi: 10.1063/1.1755429.

[35] R. Merletti, A. Botter, A. Troiano, E. Merlo, and M. A. Minetto, "Technology and instrumentation for detection and conditioning of the surface electromyographic signal: State of the art," *Clin. Biomech.*, vol. 24, pp. 122–134, Feb. 2009, doi: 10.1016/j.clinbiomech.2008.08.006.

[36] A. Akinin, A. Paul, J. Wang, A. Buccino, and G. Cauwenberghs, "Biopotential measurements and electrodes," in *Neural Engineering*, B. He, Ed. Cham, Switzerland: Springer, 2020, pp. 65–96, doi: 10.1007/978-3-030-43395-6_2.

[37] E. T. McAdams, A. Lackermeier, J. A. McLaughlin, D. Macken, and J. Jossinet, "The linear and non-linear electrical properties of the electrode-electrolyte interface," *Biosensor Bioelectron.*, vol. 10, nos. 1–2, pp. 67–74, 1995, doi: 10.1016/0956-5663(95)96795-Z.

[38] A. S. Bondarenko and G. A. Ragoisha, *Progress in Chemometrics Research*, A. L. Pomerantsev, Ed. New York: Nova Science Publishers, 2005, pp. 89–102. [Online]. Available: http://www.abc.chemistry.bsu.by/vi/analyser/

[39] J. R. Macdonald. *LEVM/LEVMW—Version 8.13 Program*. Accessed: Apr. 9, 2021. [Online]. Available: https://jrossmacdonald.com/levmlevmw/

[40] B. Howell, S. Naik, and W. M. Grill, "Influences of interpolation error, electrode geometry, and the electrode–tissue interface on models of electric fields produced by deep brain stimulation," *IEEE Trans. Biomed. Eng.*, vol. 61, no. 2, pp. 297–307, Feb. 2014, doi: 10.1109/TBME.2013.2292025.

[41] P. Pham, S. Roux, F. Matonti, F. Dupont, V. Agache, and F. Chavane, "Post-implantation impedance spectroscopy of subretinal microelectrode arrays, OCT imaging and numerical simulation: Towards a more precise neuroprosthesis monitoring tool," *J. Neural Eng.*, vol. 10, no. 4, May 2013, Art. no. 046002, doi: 10.1088/1741-2560/10/4/046002.

[42] A. S. Stojiljković, D. Ž. Sužnjević, and S. N. Blagojević, "Open-circuit potential of a pt electrode immersed in different aqueous solutions," *Reaction Kinetics, Mech. Catal.*, vol. 123, no. 1, pp. 165–175, Feb. 2018, doi: 10.1007/s11144-017-1330-8.

[43] Y. Wang *et al.*, "Activation effect of electrochemical cycling on gold nanoparticles towards the hydrogen evolution reaction in sulfuric acid," *Electrochim. Acta*, vol. 209, pp. 440–447, Aug. 2016, doi: 10.1016/j.electacta.2016.05.095.

[44] P. Kassanos, F. Seichepine, and G.-Z. Yang, "Characterization and modeling of a flexible tetrapolar bioimpedance sensor and measurements of intestinal tissues," in *Proc. IEEE 19th Int. Conf. Bioinf. Bioeng. (BIBE)*, Oct. 2019, pp. 686–690, doi: 10.1109/BIBE.2019.00129.

[45] P. Kassanos, F. Seichepine, and G.-Z. Yang, "A comparison of front-end amplifiers for tetrapolar bioimpedance measurements," *IEEE Trans. Instrum. Meas.*, vol. 70, pp. 1–14, 2021, doi: 10.1109/TIM.2020.3015605.

[46] H. Wang and L. Pilon, "Physical interpretation of cyclic voltammetry for measuring electric double layer capacitances," *Electrochim. Acta*, vol. 64, pp. 130–139, Mar. 2012, doi: 10.1016/j.electacta.2011.12.118.

[47] D. M. Morales and M. Risch, "Seven steps to reliable cyclic voltammetry measurements for the determination of double layer capacitance," *J. Phys., Energy*, Jun. 2021, Art. no. 034013, doi: 10.1088/2515-7655/abee33.

[48] N. Elgrishi, K. J. Rountree, B. D. McCarthy, E. S. Rountree, T. T. Eisenhart, and J. L. Dempsey, "A practical Beginner's guide to cyclic voltammetry," *J. Chem. Educ.*, vol. 95, no. 2, pp. 197–206, Feb. 2018, doi: 10.1021/acs.jchemed.7b00361.

[49] P. Kassanos, F. Seichepine, D. Wales, and G.-Z. Yang, "Towards a flexible/stretchable multiparametric sensing device for surgical and wearable applications," in *Proc. IEEE Biomed. Circuits Syst. Conf. (BioCAS)*, Oct. 2019, pp. 1–4.

[50] X. Yang and G. Zhang, "Simulating the structure and effect of the electrical double layer at nanometre electrodes," *Nanotechnology*, vol. 18, no. 33, Jul. 2007, Art. no. 335201, doi: 10.1088/0957-4484/18/33/335201.

[51] X. Yang and G. Zhang, "The effect of an electrical double layer on the voltammetric performance of nanoscale interdigitated electrodes: A simulation study," *Nanotechnology*, vol. 19, no. 46, Oct. 2008, Art. no. 465504, doi: 10.1088/0957-4484/19/46/465504.

[52] E. Gongadze, S. Petersen, U. Beck, and U. van Rienen, "Classical models of the interface between an electrode and an electrolyte," presented at the Comsol Conf. 2009. Accessed: Dec. 19, 2020. [Online]. Available: https://www.comsol.com/paper/classical-models-of-the-interface-between-an-electrode-and-an-electrolyte-6594

[53] S.-L. Wu, M. E. Orazem, B. Tribollet, and V. Vivier, "The influence of coupled Faradaic and charging currents on impedance spectroscopy," *Electrochim. Acta*, vol. 131, pp. 3–12, Jun. 2014, doi: 10.1016/j.electacta.2014.01.120.

[54] D. R. Cantrell, S. Inayat, A. Taflove, R. S. Ruoff, and J. B. Troy, "Incorporation of the electrode-electrolyte interface into finite-element models of metal microelectrodes," *J. Neural Eng.*, vol. 5, pp. 54–67, Mar. 2007, doi: 10.1088/1741-2560/5/1/006.

[55] C. Moulin *et al.*, "A new 3-D finite-element model based on thin-film approximation for microelectrode array recording of extracellular action potential," *IEEE Trans. Biomed. Eng.*, vol. 55, no. 2, pp. 683–692, Feb. 2008, doi: 10.1109/TBME.2007.903522.

[56] Y.-Q. Zhao, A. Demosthenous, and R. H. Bayford, "A CMOS instrumentation amplifier for wideband bioimpedance spectroscopy systems," in *Proc. IEEE Int. Symp. Circuits Syst.*, May 2006, p. 4, doi: 10.1109/ISCAS.2006.1693774.

[57] S. Grimnes and Ø. G. Martinsen, "Sources of error in tetrapolar impedance measurements on biomaterials and other ionic conductors," *J. Phys. D, Appl. Phys.*, vol. 40, no. 1, pp. 9–14, Jan. 2007, doi: 10.1088/0022-3727/40/1/S02.

[58] A. Wang, D. Jung, J. Park, G. Junek, and H. Wang, "Electrode–electrolyte interface impedance characterization of ultra-miniaturized microelectrode arrays over materials and geometries for sub-cellular and cellular sensing and stimulation," *IEEE Trans. Nanobiosci.*, vol. 18, no. 2, pp. 248–252, Apr. 2019, doi: 10.1109/TNB.2019.2905509.

[59] W. C. Stacey *et al.*, "Potential for unreliable interpretation of EEG recorded with microelectrodes," *Epilepsia*, vol. 54, no. 8, pp. 1391–1401, Aug. 2013, doi: 10.1111/epi.12202.

[60] X. Liu, A. Demosthenous, and N. Donaldson, "Platinum electrode noise in the ENG spectrum," *Med. Biol. Eng. Comput.*, vol. 46, no. 10, pp. 997–1003, Oct. 2008, doi: 10.1007/s11517-008-0386-z.

[61] J. Kilby, K. Prasad, and G. Mawston, "Multi-channel surface electromyography electrodes: A review," *IEEE Sensors J.*, vol. 16, no. 14, pp. 5510–5519, Jul. 2016, doi: 10.1109/JSEN.2016.2569072.

[62] D. Buxi *et al.*, "Correlation between electrode-tissue impedance and motion artifact in biopotential recordings," *IEEE Sensors J.*, vol. 12, no. 12, pp. 3373–3383, Dec. 2012, doi: 10.1109/JSEN.2012.2221163.

[63] Y.-F. Rui, J.-Q. Liu, B. Yang, K.-Y. Li, and C.-S. Yang, "Parylene-based implantable platinum-black coated wire microelectrode for orbicularis oculi muscle electrical stimulation," *Biomed. Microdevices*, vol. 14, no. 2, pp. 367–373, Apr. 2012, doi: 10.1007/s10544-011-9613-8.

[64] G. Gabriel, R. Gómez-Martínez, and R. Villa, "Single-walled carbon nanotubes deposited on surface electrodes to improve interface impedance," *Physiolog. Meas.*, vol. 29, no. 6, pp. S203–S212, Jun. 2008, doi: 10.1088/0967-3334/29/6/S18.

[65] S. A. Desai, J. Rolston, L. Guo, and S. Potter, "Improving impedance of implantable microwire multi-electrode arrays by ultrasonic electroplating of durable platinum black," *Frontiers Neuroengineering*, vol. 3, p. 5, May 2010, doi: 10.3389/fneng.2010.00005.

[66] M. Schuettler *et al.*, "Cytotoxicity of platinum black," in *Proc. 10th Annu. Conf. Int. Funct. Elect. Stimulation Soc. (IFESS)*, Montreal, QC, Canada, Jul. 2005, pp. 343–345.

[67] L. J. Breckenridge *et al.*, "Advantages of using microfabricated extracellular electrodes for *in vitro* neuronal recording," *J. Neurosci. Res.*, vol. 42, no. 2, pp. 266–276, Oct. 1995, doi: 10.1002/jnr.490420215.

[68] Y. J. Lee, H.-J. Kim, S. H. Do, J. Y. Kang, and S. H. Lee, "Characterization of nerve-cuff electrode interface for biocompatible and chronic stimulating application," *Sens. Actuators B, Chem.*, vol. 237, pp. 924–934, Dec. 2016, doi: 10.1016/j.snb.2016.06.169.

[69] X. T. Cui and D. D. Zhou, "Poly (3,4-ethylenedioxythiophene) for chronic neural stimulation," *IEEE Trans. Neural Syst. Rehabil. Eng.*, vol. 15, no. 4, pp. 502–508, Dec. 2007, doi: 10.1109/TNSRE.2007.909811.

[70] A. Bozkurt and A. Lal, "Low-cost flexible printed circuit technology based microelectrode array for extracellular stimulation of the invertebrate locomotory system," *Sens. Actuators A, Phys.*, vol. 169, no. 1, pp. 89–97, Sep. 2011, doi: 10.1016/j.sna.2011.05.015.

[71] V. Woods *et al.*, "A low-cost, 61-channel μECoG array for use in rodents," in *Proc. 7th Int. IEEE/EMBS Conf. Neural Eng. (NER)*, Apr. 2015, pp. 573–576, doi: 10.1109/NER.2015.7146687.

[72] A. R. Boccaccini, J. Cho, J. A. Roether, B. J. C. Thomas, E. J. Minay, and M. S. P. Shaffer, "Electrophoretic deposition of carbon nanotubes," *Carbon*, vol. 44, no. 15, pp. 3149–3160, Dec. 2006, doi: 10.1016/j.carbon.2006.06.021.

[73] S. Minnikanti, P. Skeath, and N. Peixoto, "Electrochemical characterization of multi-walled carbon nanotube coated electrodes for biological applications," *Carbon*, vol. 47, no. 3, pp. 884–893, Mar. 2009, doi: 10.1016/j.carbon.2008.11.045.

[74] B. J. C. Thomas, A. R. Boccaccini, and M. S. P. Shaffer, "Multi-walled carbon nanotube coatings using electrophoretic deposition (EPD)," *J. Amer. Ceram. Soc.*, vol. 88, no. 4, pp. 980–982, Apr. 2005, doi: 10.1111/j.1551-2916.2005.00155.x.

[75] E. Castagnola *et al.*, "PEDOT-CNT-coated low-impedance, ultra-flexible, and brain-conformable micro-ECoG arrays," *IEEE Trans. Neural Syst. Rehabil. Eng.*, vol. 23, no. 3, pp. 342–350, May 2015, doi: 10.1109/TNSRE.2014.2342880.

[76] R. Gerwig *et al.*, "PEDOT–CNT composite microelectrodes for recording and electrostimulation applications: Fabrication, morphology, and electrical properties," *Frontiers Neuroeng.*, vol. 5, p. 8, May 2012, doi: 10.3389/fneng.2012.00008.

[77] T. D. Y. Kozai *et al.*, "Chronic *in vivo* evaluation of PEDOT/CNT for stable neural recordings," *IEEE Trans. Biomed. Eng.*, vol. 63, no. 1, pp. 111–119, Jan. 2016, doi: 10.1109/TBME.2015.2445713.

[78] M. Abu-Saude and B. I. Morshed, "Characterization of a novel polypyrrole (PPy) conductive polymer coated patterned vertical CNT (pvCNT) dry ECG electrode," *Chemosensors*, vol. 6, no. 3, p. 3, Sep. 2018, doi: 10.3390/chemosensors6030027.

[79] A. Ruiz-Vargas, A. Ivorra, and J. W. Arkwright, "Monitoring the effect of contact pressure on bioimpedance measurements," in *Proc. 40th Annu. Int. Conf. IEEE Eng. Med. Biol. Soc. (EMBC)*, Jul. 2018, pp. 4949–4952, doi: 10.1109/EMBC.2018.8513173.

[80] D. B. Geselowitz, "An application of electrocardiographic lead theory to impedance plethysmography," *IEEE Trans. Biomed. Eng.*, vol. BME-18, no. 1, pp. 38–41, Jan. 1971, doi: 10.1109/TBME.1971.4502787.

[81] J. Lehr, "A vector derivation useful in impedance plethysmographic field calculations," *IEEE Trans. Biomed. Eng.*, vol. BME-19, no. 2, pp. 156–157, Mar. 1972, doi: 10.1109/TBME.1972.324058.

[82] J. R. Mortarelli, "A generalization of the Geselowitz relationship useful in impedance plethysmographic field calculations," *IEEE Trans. Biomed. Eng.*, vol. BME-27, no. 11, pp. 665–667, Nov. 1980, doi: 10.1109/TBME.1980.326677.

[83] S. M. Radke and E. C. Alocilja, "Design and fabrication of a microimpedance biosensor for bacterial detection," *IEEE Sensors J.*, vol. 4, no. 4, pp. 434–440, Aug. 2004, doi: 10.1109/JSEN.2004.830300.

[84] P. Van Gerwen *et al.*, "Nanoscaled interdigitated electrode arrays for biochemical sensors," *Sens. Actuators B, Chem.*, vol. 49, no. 1, pp. 73–80, 1998, doi: 10.1016/S0925-4005(98)00128-2.

[85] P. Kassanos, A. Demosthenous, and R. H. Bayford, "Optimization of bipolar and tetrapolar impedance biosensors," in *Proc. IEEE Int. Symp. Circuits Syst.*, May 2010, pp. 1512–1515, doi: 10.1109/ISCAS.2010.5537373.

[86] P. Kassanos, R. H. Bayford, and A. Demosthenous, "Electric field characteristics of bipolar impedance sensors," in *Proc. World Congr. Med. Phys. Biomed. Eng.*, Munich, Germany, vol. 25/8, O. Dössel and W. C. Schlegel, Eds. Berlin, Germany: Springer, Sep. 2009, doi: 10.1007/978-3-642-03887-7_79.

[87] P. Kassanos, "Modelling, design and validation of tetrapolar impedance biosensors for lab-on-a-chip applications," Doctoral thesis, Dept. Electron. Elect. Eng., Univ. College London, London, U.K., 2012. Accessed: Dec. 8, 2020. [Online]. Available: https://discovery.ucl.ac.uk/id/eprint/1348484/

[88] P. Kassanos, A. Demosthenous, and R. H. Bayford, "Comparison of tetrapolar injection-measurement techniques for coplanar affinity-based impedimetric immunosensors," in *Proc. IEEE Biomed. Circuits Syst. Conf.*, Nov. 2008, pp. 317–320, doi: 10.1109/BIOCAS.2008.4696938.

[89] P. Kassanos, A. Demosthenous, and R. H. Bayford, "Towards an optimized design for tetrapolar affinity-based impedimetric immunosensors for lab-on-a-chip applications," in *Proc. IEEE Biomed. Circuits Syst. Conf.*, Nov. 2008, pp. 141–144, doi: 10.1109/BIOCAS.2008.4696894.

[90] B. H. Brown, A. J. Wilson, and P. Bertemes-Filho, "Bipolar and tetrapolar transfer impedance measurements from volume conductor," *Electron. Lett.*, vol. 36, no. 25, pp. 2060–2062, Dec. 2000, doi: 10.1049/el:20001439.

[91] A. Guimera, A. Ivorra, G. Gabriel, and R. Villa, "Non-invasive assessment of corneal endothelial permeability by means of electrical impedance measurements," *Med. Eng. Phys.*, vol. 32, no. 10, pp. 1107–1115, Dec. 2010, doi: 10.1016/j.medengphy.2010.07.016.

[92] A. C. Ivorra, *Contributions to the Measurement of Electrical Impedance for Living Tissue Ischemia Injury Monitoring*. Barcelona, Spain: Universitat Politécnica de Catalunya, 2005. Accessed: Oct. 18, 2016. [Online]. Available: http://www.openthesis.org/documents/Contributions-to-measurement-electrical-impedance-576025.html

[93] S. S. Gevorgian, T. Martinsson, P. L. J. Linner, and E. L. Kollberg, "CAD models for multilayered substrate interdigital capacitors," *IEEE Trans. Microw. Theory Techn.*, vol. 44, no. 6, pp. 896–904, Jun. 1996, doi: 10.1109/22.506449.

[94] T. Sun, H. Morgan, and N. G. Green, "Analytical solutions of AC electrokinetics in interdigitated electrode arrays: Electric field, dielectrophoretic and traveling-wave dielectrophoretic forces," *Phys. Rev. E, Stat. Phys. Plasmas Fluids Relat. Interdiscip. Top.*, vol. 76, no. 4, Oct. 2007, Art. no. 046610, doi: 10.1103/PhysRevE.76.046610.

[95] B. Timmer, W. Sparreboom, W. Olthuis, P. Bergveld, and A. van den Berg, "Optimization of an electrolyte conductivity detector for measuring low ion concentrations," *Lab Chip*, vol. 2, no. 2, pp. 121–124, May 2002, doi: 10.1039/B201225A.

[96] W. Olthuis, W. Streekstra, and P. Bergveld, "Theoretical and experimental determination of cell constants of planar-interdigitated electrolyte conductivity sensors," *Sens. Actuators B, Chem.*, vol. 24, nos. 1–3, pp. 252–256, 1995, doi: 10.1016/0925-4005(95)85053-8.

[97] P. Jacobs, A. Varlan, and W. Sansen, "Design optimisation of planar electrolytic conductivity sensors," *Med. Biol. Eng. Comput.*, vol. 33, no. 6, pp. 802–810, Nov. 1995, doi: 10.1007/BF02523012.

[98] R. Schinzinger and P. A. A. Laura, *Conformal Mapping: Methods and Applications*. Chelmsford, MA, USA: Courier Corporation, 2012.

[99] T. A. Driscoll. (Jun. 5, 2019). *Schwarz-Christoffel Toolbox for MATLAB*. Toby Driscoll. Accessed: Mar. 29, 2021. [Online]. Available: https://tobydriscoll.net/project/sc-toolbox/

[100] P. Bertemes-Filho, B. H. Brown, R. H. Smallwood, and A. J. Wilson, "Stand-off electrode (SoE): A new method for improving the sensitivity distribution of a tetrapolar probe," *Physiolog. Meas.*, vol. 24, no. 2, pp. 517–525, Apr. 2003, doi: 10.1088/0967-3334/24/2/362.

[101] K. Pesti, H. Koiv, and M. Min, "Simulation of the sensitivity distribution of four-electrode impedance sensing on radial artery," in *Proc. IEEE Sensors Appl. Symp. (SAS)*, Mar. 2019, pp. 1–6, doi: 10.1109/SAS.2019.8705976.

[102] S. Cho and H. Thielecke, "Design of electrode array for impedance measurement of lesions in arteries," *Physiolog. Meas.*, vol. 26, no. 2, pp. S19–S26, Mar. 2005, doi: 10.1088/0967-3334/26/2/002.

[103] J. Wtorek *et al.*, "Monitoring of myocardium state during off-pump coronary artery by-pass grafting," *Physiolog. Meas.*, vol. 29, no. 6, pp. S393–S405, Jun. 2008, doi: 10.1088/0967-3334/29/6/S33.

[104] J. Wtorek, A. Bujnowski, A. Polinski, and A. Nowakowski, "A six-ring probe for monitoring conductivity changes," *Physiolog. Meas.*, vol. 26, no. 2, pp. S69–S79, Mar. 2005, doi: 10.1088/0967-3334/26/2/007.

[105] Y. Su, "Modeling and characteristic study of thin film based biosensor based on COMSOL," *Math. Problems Eng.*, vol. 2014, pp. 1–6, Apr. 2014, doi: 10.1155/2014/581063.

[106] C. Canali *et al.*, "Bioimpedance monitoring of 3D cell culturing—Complementary electrode configurations for enhanced spatial sensitivity," *Biosens. Bioelectron.*, vol. 63, pp. 72–79, Jan. 2015, doi: 10.1016/j.bios.2014.07.020.

[107] T. Grysiński and Z. Moroń, "Planar sensors for local conductivity measurements in biological objects—Design, modelling, sensitivity maps," *Sens. Actuators B, Chem.*, vol. 158, no. 1, pp. 190–198, Nov. 2011, doi: 10.1016/j.snb.2011.06.003.

[108] M. F. Suesserman and F. A. Spelman, "Quantitative in vivo measurements of inner ear tissue resistivities. I. *In vitro* characterization," *IEEE Trans. Biomed. Eng.*, vol. 40, no. 10, pp. 1032–1047, Oct. 1993, doi: 10.1109/10.247802.

[109] P. Steendijk, G. Mur, E. T. van der Velde, and J. Baan, "The four-electrode resistivity technique in anisotropic media: Theoretical analysis and application on myocardial tissue *in vivo*," *IEEE Trans. Biomed. Eng.*, vol. 40, no. 11, pp. 1138–1148, Nov. 1993, doi: 10.1109/10.245632.

[110] C. Canali *et al.*, "An impedance method for spatial sensing of 3D cell constructs—Towards applications in tissue engineering," *Analyst*, vol. 140, no. 17, pp. 6079–6088, 2015, doi: 10.1039/C5AN00987A.

[111] K. Pesti, M. Metshein, P. Annus, H. Koiv, and M. Min, "Electrode placement strategies for the measurement of radial artery bioimpedance: Simulations and experiments," *IEEE Trans. Instrum. Meas.*, vol. 70, pp. 1–10, 2021, doi: 10.1109/TIM.2020.3011784.

[112] N. Islam, K. S.-E. Rabbani, and A. Wilson, "The sensitivity of focused electrical impedance measurements," *Physiolog. Meas.*, vol. 31, no. 8, pp. S97–S109, Jul. 2010, doi: 10.1088/0967-3334/31/8/S08.

[113] K. S. Rabbani, M. Sarker, M. H. R. Akond, and T. Akter, "Focused impedance measurement (FIM): A new technique with improved zone localization," *Ann. New York Acad. Sci.*, vol. 873, no. 1, pp. 408–420, Apr. 1999, doi: 10.1111/j.1749-6632.1999.tb09490.x.

[114] S. P. Ahmed, M. A. Kadir, G. D. A. Quaderi, R. Rahman, and K. S. E. Rabbani, "Improved understanding of the sensitivity of linear tetrapolar impedance measurement (TPIM) and 8-electrode focused impedance method (FIM) in a volume conductor," *Bangladesh J. Med. Phys.*, vol. 8, no. 1, pp. 22–31, Sep. 2017, doi: 10.3329/bjmp.v8i1.33931.

[115] K. S. Rabbani, "Focused impedance method: Basics and applications," in *Bioimpedance in Biomedical Applications and Research*, F. Simini and P. Bertemes-Filho, Eds. Cham, Switzerland: Springer, 2018, pp. 137–185, doi: 10.1007/978-3-319-74388-2_9.

[116] K. S. Rabbani and M. A. S. Karal, "A new four-electrode focused impedance measurement (FIM) system for physiological study," *Ann. Biomed. Eng.*, vol. 36, no. 6, pp. 1072–1077, Jun. 2008, doi: 10.1007/s10439-008-9470-7.

[117] F. J. Pettersen, H. Ferdous, H. Kalvøy, Ø. G. Martinsen, and J. O. Høgetveit, "Comparison of four different FIM configurations—A simulation study," *Physiolog. Meas.*, vol. 35, no. 6, pp. 1067–1082, May 2014, doi: 10.1088/0967-3334/35/6/1067.

[118] J. D. Wiley and J. G. Webster, "Analysis and control of the current distribution under circular dispersive electrodes," *IEEE Trans. Biomed. Eng.*, vol. BME-29, no. 5, pp. 381–385, May 1982, doi: 10.1109/TBME.1982.324910.

[119] K. M. Overmyer, J. A. Pearce, and D. P. DeWitt, "Measurements of temperature distributions at electro-surgical dispersive electrode sites," *J. Biomech. Eng.*, vol. 101, no. 1, pp. 66–72, Feb. 1979, doi: 10.1115/1.3426227.

[120] S. Tungjitkusolmun, E. J. Woo, H. Cao, J.-Z. Tsai, V. R. Vorperian, and J. G. Webster, "Finite element analyses of uniform current density electrodes for radio-frequency cardiac ablation," *IEEE Trans. Biomed. Eng.*, vol. 47, no. 1, pp. 32–40, Jan. 2000, doi: 10.1109/10.817617.

[121] J. T. Rubinstein, F. A. Spelman, M. Soma, and M. F. Suesserman, "Current density profiles of surface mounted and recessed electrodes for neural prostheses," *IEEE Trans. Biomed. Eng.*, vol. BME-34, no. 11, pp. 864–875, Nov. 1987, doi: 10.1109/TBME.1987.326007.

[122] M. F. Suesserman, F. A. Spelman, and J. T. Rubinstein, "*In vitro* measurement and characterization of current density profiles produced by nonrecessed, simple recessed, and radially varying recessed stimulating electrodes," *IEEE Trans. Biomed. Eng.*, vol. 38, no. 5, pp. 401–408, May 1991, doi: 10.1109/10.81558.

[123] A. C. West and J. Newman, "Current distributions on recessed electrodes," *J. Electrochem. Soc.*, vol. 138, no. 6, p. 1620, Jun. 1991, doi: 10.1149/1.2085844.

[124] D. A. Ksienski, "A minimum profile uniform current density electrode," *IEEE Trans. Biomed. Eng.*, vol. 39, no. 7, pp. 682–692, Jul. 1992, doi: 10.1109/10.142643.

[125] J. D. Weiland, D. J. Anderson, C. C. Pogatchnik, and J. J. Boogaard, "Recessed electrodes formed by laser ablation of parylene coated, micromachined silicon probes," in *Proc. 19th Annu. Int. Conf. IEEE Eng. Med. Biol. Soc. Magnificent Milestones Emerg. Opportunities Med. Eng.*, Oct. 1997, pp. 2273–2276, doi: 10.1109/IEMBS.1997.758815.

[126] A. Kacanovska, Z. Rong, M. Schmidt, P. S. J. Russell, and P. Vadgama, "Bio-sensing using recessed gold-filled capillary amperometric electrodes," *Anal. Bioanal. Chem.*, vol. 398, no. 4, pp. 1687–1694, Oct. 2010, doi: 10.1007/s00216-010-3891-5.

[127] R. A. Linsenmeier and C. M. Yancey, "Improved fabrication of double-barreled recessed cathode O_2 microelectrodes," *J. Appl. Physiol.*, vol. 63, no. 6, pp. 2554–2557, Dec. 1987, doi: 10.1152/jappl.1987.63.6.2554.

[128] G. Schneiderman and T. K. Goldstick, "Oxygen electrode design criteria and performance characteristics: Recessed cathode," *J. Appl. Physiol.*, vol. 45, no. 1, pp. 145–154, Jul. 1978, doi: 10.1152/jappl.1978.45.1.145.

[129] T.-S. Lim, J.-H. Lee, and I. Papautsky, "Effect of recess dimensions on performance of the needle-type dissolved oxygen microelectrode sensor," *Sens. Actuators B, Chem.*, vol. 141, no. 1, pp. 50–57, Aug. 2009, doi: 10.1016/j.snb.2009.05.041.

[130] C. K. Giardina, E. S. Krause, K. Koka, and D. C. Fitzpatrick, "Impedance measures during *in vitro* cochlear implantation predict array positioning," *IEEE Trans. Biomed. Eng.*, vol. 65, no. 2, pp. 327–335, Feb. 2018, doi: 10.1109/TBME.2017.2764881.

[131] E. Saunders *et al.*, "Threshold, comfortable level and impedance changes as a function of electrode-modiolar distance," *Ear Hearing*, vol. 23, no. 1, p. 28S, Feb. 2002.

[132] C.-T. Tan *et al.*, "Real-time measurement of electrode impedance during intracochlear electrode insertion," *Laryngoscope*, vol. 123, no. 4, pp. 1028–1032, Apr. 2013, doi: 10.1002/lary.23714.

[133] S. Anastasova, P. Kassanos, and G.-Z. Yang, "Multi-parametric rigid and flexible, low-cost, disposable sensing platforms for biomedical applications," *Biosens, Bioelectron.*, vol. 102, pp. 668–675, Apr. 2018, doi: 10.1016/j.bios.2017.10.038.

[134] P. Kassanos, S. Anastasova, and G.-Z. Yang, "A low-cost amperometric glucose sensor based on PCB technology," in *Proc. IEEE Sensors*, Oct. 2018, pp. 1–4, doi: 10.1109/ICSENS.2018.8589804.

[135] M. Berthelot, G.-Z. Yang, and B. Lo, "A self-calibrated tissue viability sensor for free flap monitoring," *IEEE J. Biomed. Health Informat.*, vol. 22, no. 1, pp. 5–14, Jan. 2018, doi: 10.1109/JBHI.2017.2773998.

[136] X. Huang, W.-H. Yeo, Y. Liu, and J. A. Rogers, "Epidermal differential impedance sensor for conformal skin hydration monitoring," *Biointerphases*, vol. 7, no. 1, p. 52, Dec. 2012, doi: 10.1007/s13758-012-0052-8.

[137] J. A. Rogers, T. Someya, and Y. Huang, "Materials and mechanics for stretchable electronics," *Science*, vol. 327, no. 5973, pp. 1603–1607, Mar. 2010, doi: 10.1126/science.1182383.

[138] A. J. Bandodkar *et al.*, "Battery-free, skin-interfaced microfluidic/electronic systems for simultaneous electrochemical, colorimetric, and volumetric analysis of sweat," *Sci. Adv.*, vol. 5, no. 1, Jan. 2019, Art. no. eaav3294, doi: 10.1126/sciadv.aav3294.

[139] D.-H. Kim *et al.*, "Epidermal electronics," *Science*, vol. 333, no. 6044, pp. 838–843, 2011, doi: 10.1126/science.1206157.

[140] M. Hu, P. Kassanos, M. Keshavarz, E. Yeatman, and B. Lo, "Electrical and mechanical characterization of carbon-based elastomeric composites for printed sensors and electronics," in *Proc. IEEE Int. Conf. Flexible Printable Sensors Syst. (FLEPS)*, Jun. 2021, pp. 1–4.

[141] M. Tavakoli *et al.*, "Carbon doped PDMS: Conductance stability over time and implications for additive manufacturing of stretchable electronics," *J. Micromech. Microeng.*, vol. 27, no. 3, 2017, Art. no. 035010, doi: 10.1088/1361-6439/aa5ab1.

[142] M. D. Dickey, "Stretchable and soft electronics using liquid metals," *Adv. Mater.*, vol. 29, no. 27, Jul. 2017, Art. no. 1606425, doi: 10.1002/adma.201606425.

[143] F. Xu and Y. Zhu, "Highly conductive and stretchable silver nanowire conductors," *Adv. Mater.*, vol. 24, no. 37, pp. 5117–5122, 2012, doi: 10.1002/adma.201201886.

[144] A. Larmagnac, S. Eggenberger, H. Janossy, and J. Vörös, "Stretchable electronics based on ag-PDMS composites," *Sci. Rep.*, vol. 4, no. 1, pp. 1–7, Dec. 2014, doi: 10.1038/srep07254.

[145] X. Niu, S. Peng, L. Liu, W. Wen, and P. Sheng, "Characterizing and patterning of PDMS-based conducting composites," *Adv. Mater.*, vol. 19, no. 18, pp. 2682–2686, 2007, doi: 10.1002/adma.200602515.

[146] S. Park *et al.*, "Silicones for stretchable and durable soft devices: Beyond Sylgard-184," *ACS Appl Mater. Interfaces*, vol. 10, pp. 11261–11268, Apr. 2018, doi: 10.1021/acsami.7b18394.

[147] S. H. Jeong, S. Zhang, K. Hjort, J. Hilborn, and Z. Wu, "PDMS-based elastomer tuned soft, stretchable, and sticky for epidermal electronics," *Adv. Mater.*, vol. 28, pp. 5830–5836, May 2016, doi: 10.1002/adma.201505372.

[148] H. Chen *et al.*, "Super tough and self-healable poly(dimethylsiloxane) elastomer via hydrogen bonding association and its applications as triboelectric nanogenerators," *ACS Appl. Mater. Interface*, vol. 12, no. 28, pp. 31975–31983, Jul. 2020, doi: 10.1021/acsami.0c08213.

[149] R. Bernasconi, D. Meroni, A. Aliverti, and L. Magagnin, "Fabrication of a bioimpedance sensor via inkjet printing and selective metallization," *IEEE Sensors J.*, vol. 20, no. 23, pp. 14024–14031, Dec. 2020, doi: 10.1109/JSEN.2020.3007619.

[150] D. Mojena-Medina, M. Hubl, M. Bäuscher, J. L. Jorcano, H.-D. Ngo, and P. Acedo, "Real-time impedance monitoring of epithelial cultures with inkjet-printed interdigitated-electrode sensors," *Sensors*, vol. 20, no. 19, p. 5711, Oct. 2020, doi: 10.3390/s20195711.

[151] A. Kekonen *et al.*, "Bioimpedance method for monitoring venous ulcers: Clinical proof-of-concept study," *Biosens. Bioelectron.*, vol. 178, Apr. 2021, Art. no. 112974, doi: 10.1016/j.bios.2021.112974.

[152] A. D. Valentine *et al.*, "Hybrid 3D printing of soft electronics," *Adv. Mater.*, vol. 29, no. 40, Jun. 2017, Art. no. 1703817, doi: 10.1002/ADMA.201703817.

[153] J. T. Muth *et al.*, "Embedded 3D printing of strain sensors within highly stretchable elastomers," *Adv. Mater.*, vol. 26, no. 36, pp. 6307–6312, 2014, doi: 10.1002/adma.201400334.

[154] B. Herren, M. C. Saha, M. C. Altan, and Y. Liu, "Development of ultrastretchable and skin attachable nanocomposites for human motion monitoring via embedded 3D printing," *Compos. B, Eng.*, vol. 200, Nov. 2020, Art. no. 108224, doi: 10.1016/j.compositesb.2020.108224.

[155] R. N. Esfahani *et al.*, "Light based synthesis of metallic nanoparticles on surface-modified 3D printed substrates for high performance electronic systems," *Additive Manuf.*, vol. 34, Aug. 2020, Art. no. 101367, doi: 10.1016/j.addma.2020.101367.

[156] S. Emran, K. Laitinen, R. Lappalainen, and S. Myllymaa, "Novel 3D printing-based probe for impedance spectroscopic examination of oral mucosa: Design and preliminary testing with phantom models," *J. Med. Eng. Technol.*, vol. 44, no. 8, pp. 517–526, Nov. 2020, doi: 10.1080/03091902.2020.1831633.

[157] R. Rahimi *et al.*, "Highly stretchable and sensitive unidirectional strain sensor via laser carbonization," *ACS Appl. Mater. Interfaces*, vol. 7, no. 8, pp. 4463–4470, Mar. 2015, doi: 10.1021/am509087u.

[158] J. Lin *et al.*, "Laser-induced porous graphene films from commercial polymers," *Nature Commun.*, vol. 5, p. 5714, Dec. 2014, doi: 10.1038/ncomms6714.

[159] P. Kassanos, G.-Z. Yang, and E. Yeatman, "An interdigital strain sensor through laser carbonization of PI and PDMS transfer," in *Proc. IEEE Int. Conf. Flexible Printable Sensors Syst. (FLEPS)*, Jun. 2021, pp. 1–4.

[160] S. Yang *et al.*, "'Cut-and-paste' manufacture of multiparametric epidermal sensor systems," *Adv. Mater.*, vol. 27, no. 41, pp. 6423–6430, Nov. 2015, doi: 10.1002/adma.201502386.

[161] T. Ha *et al.*, "A chest-laminated ultrathin and stretchable E-tattoo for the measurement of electrocardiogram, seismocardiogram, and cardiac time intervals," *Adv. Sci.*, vol. 6, no. 14, Jul. 2019, Art. no. 1900290, doi: 10.1002/advs.201900290.

[162] P. Kassanos, B. G. Rosa, M. Keshavarz, and G.-Z. Yang, "From wearables to implantables-clinical drive and technical challenges," in *Wearable Sensors*, 2nd ed, E. Sazonov, Ed. Oxford, U.K.: Academic, 2021, pp. 29–84, doi: 10.1016/B978-0-12-819246-7.00002-4.

[163] S.-W. Hwang *et al.*, "A physically transient form of silicon electronics," *Science*, vol. 337, no. 6102, pp. 1640–1644, Sep. 2012, doi: 10.1126/science.1226325.

[164] P. Kassanos, S. Anastasova, and G.-Z. Yang, "Towards low-cost cell culturing platforms with integrated sensing capabilities," in *Proc. IEEE Biomed. Circuits Syst. Conf. (BioCAS)*, Oct. 2018, pp. 1–4, doi: 10.1109/BIOCAS.2018.8584789.

[165] P. Kassanos, F. Seichepine, M. Keshavarz, and G.-Z. Yang, "Towards a flexible wrist-worn thermotherapy and thermoregulation device," in *Proc. IEEE 19th Int. Conf. Bioinf. Bioeng. (BIBE)*, Oct. 2019, pp. 644–648, doi: 10.1109/BIBE.2019.00121.

[166] P. Kassanos, F. Seichepine, I. Kassanos, and G.-Z. Yang, "Development and characterization of a PCB-based microfluidic YChannel," in *Proc. 42nd Annu. Int. Conf. IEEE Eng. Med. Biol. Soc. (EMBC)*, Jul. 2020, pp. 5037–5040, doi: 10.1109/EMBC44109.2020.9176657.

[167] B. Taji, S. Shirmohammadi, V. Groza, and I. Batkin, "Impact of skin-electrode interface on electrocardiogram measurements using conductive textile electrodes," *IEEE Trans. Instrum. Meas.*, vol. 63, no. 6, pp. 1412–1422, Jun. 2014, doi: 10.1109/TIM.2013.2289072.

[168] G. Acar, O. Ozturk, A. J. Golparvar, T. A. Elboshra, K. Böhringer, and M. K. Yapici, "Wearable and flexible textile electrodes for biopotential signal monitoring: A review," *Electronics*, vol. 8, no. 5, p. 479, Apr. 2019, doi: 10.3390/electronics8050479.

[169] A. Achilli, A. Bonfiglio, and D. Pani, "Design and characterization of screen-printed textile electrodes for ECG monitoring," *IEEE Sensors J.*, vol. 18, no. 10, pp. 4097–4107, May 2018, doi: 10.1109/JSEN.2018.2819202.

[170] A. Ankhili, X. Tao, C. Cochrane, V. Koncar, D. Coulon, and J.-M. Tarlet, "Comparative study on conductive knitted fabric electrodes for long-term electrocardiography monitoring: Silver-plated and PEDOT:PSS coated fabrics," *Sensors*, vol. 18, no. 11, p. 3890, Nov. 2018, doi: 10.3390/s18113890.

[171] L. Zhang, M. Fairbanks, and T. L. Andrew, "Rugged textile electrodes for wearable devices obtained by vapor coating off-the-shelf, plain-woven fabrics," *Adv. Funct. Mater.*, vol. 27, no. 24, Jun. 2017, Art. no. 1700415, doi: 10.1002/adfm.201700415.

[172] P. A. Haddad, A. Servati, S. Soltanian, P. Servati, and F. Ko, "Roll-to-roll electrochemical fabrication of non-polarizable silver/silver chloride-coated nylon yarn for biological signal monitoring," *Textile Res. J.*, vol. 89, no. 17, pp. 3591–3600, Sep. 2019, doi: 10.1177/0040517518817060.

[173] M. Jose, M. Lemmens, S. Bormans, R. Thoelen, and W. Deferme, "Fully printed, stretchable and wearable bioimpedance sensor on textiles for tomography," *Flexible Printed Electron.*, vol. 6, no. 1, Feb. 2021, Art. no. 015010, doi: 10.1088/2058-8585/abe51b.

[174] I. del Agua *et al.*, "DVS-crosslinked PEDOT:PSS free-standing and textile electrodes toward wearable health monitoring," *Adv. Mater. Technol.*, vol. 3, no. 10, Jan. 2018, Art. no. 1700322, doi: 10.1002/admt.201700322.

[175] A. B. Nigusse, B. Malengier, D. A. Mengistie, G. B. Tseghai, and L. Van Langenhove, "Development of washable silver printed textile electrodes for long-term ECG monitoring," *Sensors*, vol. 20, no. 21, p. 6233, Oct. 2020, doi: 10.3390/s20216233.

[176] C. Wang *et al.*, "Intrinsically stretchable and conductive textile by a scalable process for elastic wearable electronics," *ACS Appl. Mater. Interface*, vol. 9, no. 15, pp. 13331–13338, Apr. 2017, doi: 10.1021/acsami.7b02985.

[177] N. Neshatvar, P. Langlois, R. Bayford, and A. Demosthenous, "Analog integrated current drivers for bioimpedance applications: A review," *Sensors*, vol. 19, no. 4, p. 756, Feb. 2019, doi: 10.3390/s19040756.

[178] P. Kassanos, H. Ip, and G.-Z. Yang, "Ultra-low power application-specific integrated circuits for sensing," in *Implantable Sensors and Systems: From Theory to Practice*. Cambridge, U.K.: Springer, 2018, pp. 281–437, doi: 10.1007/978-3-319-69748-2_5.

[179] P. Bertemes-Filho, V. C. Vincence, M. M. Santos, and I. X. Zanatta, "Low power current sources for bioimpedance measurements: A comparison between Howland and OTA-based CMOS circuits," *J. Electr. Bioimpedance*, vol. 3, no. 1, pp. 66–73, Oct. 2012, doi: 10.5617/jeb.380.

[180] A. S. Tucker, R. M. Fox, and R. J. Sadleir, "Biocompatible, high precision, wideband, improved Howland current source with lead-lag compensation," *IEEE Trans. Biomed. Circuits Syst.*, vol. 7, no. 1, pp. 63–70, Feb. 2013, doi: 10.1109/TBCAS.2012.2199114.

[181] P. Kassanos, I. F. Triantis, and A. Demosthenous, "A CMOS magnitude/phase measurement chip for impedance spectroscopy," *IEEE Sensors J.*, vol. 13, no. 6, pp. 2229–2236, Jun. 2013, doi: 10.1109/JSEN.2013.2251628.

[182] M. Usman, M. Leone, A. K. Gupta, and W. Xue, "Fabrication and analysis of wearable bioimpedance analyzers on paper and plastic substrates," *IEEE Sensors Lett.*, vol. 4, no. 3, Mar. 2020, Art. no. 6000304, doi: 10.1109/lsens.2020.2977232.

[183] S. Rodriguez, S. Ollmar, M. Waqar, and A. Rusu, "A batteryless sensor ASIC for implantable bio-impedance applications," *IEEE Trans. Biomed. Circuits Syst.*, vol. 10, no. 3, pp. 533–544, Jun. 2016, doi: 10.1109/TBCAS.2015.2456242.

[184] L. Yan, J. Bae, S. Lee, T. Roh, K. Song, and H.-J. Yoo, "A 3.9 mW 25-electrode reconfigured sensor for wearable cardiac monitoring system," *IEEE J. Solid-State Circuits*, vol. 46, no. 1, pp. 353–364, Jan. 2011, doi: 10.1109/JSSC.2010.2074350.

[185] B. Sanchez, G. Vandersteen, R. Bragos, and J. Schoukens, "Basics of broadband impedance spectroscopy measurements using periodic excitations," *Meas. Sci. Technol.*, vol. 23, no. 10, Oct. 2012, Art. no. 105501, doi: 10.1088/0957-0233/23/10/105501.

[186] B. Sanchez, X. Fernandez, S. Reig, and R. Bragos, "An FPGA-based frequency response analyzer for multisine and stepped sine measurements on stationary and time-varying impedance," *Meas. Sci. Technol.*, vol. 25, no. 1, Jan. 2014, Art. no. 015501, doi: 10.1088/0957-0233/25/1/015501.

[187] L. Lo Presti and G. Cardamone, "A direct digital frequency synthesizer using an IIR filter implemented with a DSP microprocessor," in *Proc. IEEE Int. Conf. Acoust., Speech Signal Process. (ICASSP)*, Apr. 1994, pp. III/201–III/204, doi: 10.1109/ICASSP.1994.390055.

[188] A. I. Abu-El-Haija, M. M. Al-Ibrahim, and M. A. Al-Jarrah, "Recursive digital sine wave oscillators using the TMS32010 DSP," in *Proc. Conf. 10th Anniversary IMTC Adv. Technol. I M. IEEE Instrum. Meas. Technolgy Conf.*, May 1994, pp. 792–796, doi: 10.1109/IMTC.1994.351886.

[189] S.-K. Hong and D.-W. Jee, "A 0.052 mm^2, <0.4% THD, sinusoidal current generator for bio-impedance measurement using a recursive digital oscillator and current-domain FIR filter," *IEEE Trans. Circuits Syst. II, Exp. Briefs*, vol. 66, no. 6, pp. 894–898, Jun. 2019, doi: 10.1109/TCSII.2018.2870833.

[190] C. Yang and A. J. Mason, "Fully integrated seven-order frequency-range quadrature sinusoid signal generator," *IEEE Trans. Instrum. Meas.*, vol. 58, no. 10, pp. 3481–3489, Oct. 2009, doi: 10.1109/TIM.2009.2018001.

[191] B. Linares-Barranco, T. Serrano-Gotarredona, J. Ramos-Martos, J. Ceballos-Caceres, J. M. Mora, and A. Linares-Barranco, "A precise 90 deg; quadrature OTA-C oscillator tunable in the 50-130-MHz range," *IEEE Trans. Circuits Syst. I, Reg. Papers*, vol. 51, no. 4, pp. 649–663, Apr. 2004, doi: 10.1109/TCSI.2004.823673.

[192] P. Kassanos and I. F. Triantis, "A CMOS multi-sine signal generator for multi-frequency bioimpedance measurements," in *Proc. IEEE Int. Symp. Circuits Syst. (ISCAS)*, Jun. 2014, pp. 249–252, doi: 10.1109/ISCAS.2014.6865112.

[193] A. Yufera, A. Rueda, J. M. Munoz, R. Doldan, G. Leger, and E. O. Rodriguez-Villegas, "A tissue impedance measurement chip for myocardial ischemia detection," *IEEE Trans. Circuits Syst. I, Reg. Papers*, vol. 52, no. 12, pp. 2620–2628, Dec. 2005, doi: 10.1109/TCSI.2005.857542.

[194] C.-L. Wei, Y.-W. Wang, and B.-D. Liu, "Wide-range filter-based sinusoidal wave synthesizer for electrochemical impedance spectroscopy measurements," *IEEE Trans. Biomed. Circuits Syst.*, vol. 8, no. 3, pp. 442–450, Jun. 2014, doi: 10.1109/TBCAS.2013.2274100.

[195] V. Sirtoli, K. Morcelles, J. Gomez, and P. Bertemes-Filho, "Design and evaluation of an electrical bioimpedance device based on DIBS for myography during isotonic exercises," *J. Low Power Electron. Appl.*, vol. 8, no. 4, p. 50, Dec. 2018, doi: 10.3390/jlpea8040050.

[196] P. Kassanos, L. Constantinou, I. F. Triantis, and A. Demosthenous, "An integrated analog readout for multi-frequency bioimpedance measurements," *IEEE Sensors J.*, vol. 14, no. 8, pp. 2792–2800, Aug. 2014, doi: 10.1109/JSEN.2014.2315963.

[197] N. Neshatvar, P. Langlois, and A. Demosthenous, "A non-linear feedback current driver with automatic phase compensation for bioimpedance applications," *IEEE Trans. Circuits Syst. II, Exp. Briefs*, vol. 65, no. 10, pp. 1340–1344, Oct. 2018, doi: 10.1109/TCSII.2018.2856377.

[198] P. Kassanos and G.-Z. Yang, "A CMOS programmable phase shifter for compensating synchronous detection bioimpedance systems," in *Proc. 24th IEEE Int. Conf. Electron., Circuits Syst. (ICECS)*, Dec. 2017, pp. 218–221, doi: 10.1109/ICECS.2017.8292091.

[199] F. Seoane, R. Macías, R. Bragós, and K. Lindecrantz, "Simple voltage-controlled current source for wideband electrical bioimpedance spectroscopy: Circuit dependences and limitations," *Meas. Sci. Technol.*, vol. 22, no. 11, Nov. 2011, Art. no. 115801, doi: 10.1088/0957-0233/22/11/115801.

[200] P. Bertemes-Filho, B. H. Brown, and A. J. Wilson, "A comparison of modified Howland circuits as current generators with current mirror type circuits," *Physiolog. Meas.*, vol. 21, no. 1, pp. 1–6, Feb. 2000, doi: 10.1088/0967-3334/21/1/301.

[201] L. Constantinou, R. Bayford, and A. Demosthenous, "A wideband low-distortion CMOS current driver for tissue impedance analysis," *IEEE Trans. Circuits Syst. II, Exp. Briefs*, vol. 62, no. 2, pp. 154–158, Feb. 2015, doi: 10.1109/TCSII.2014.2387632.

[202] H. Hong, M. Rahal, A. Demosthenous, and R. H. Bayford, "Comparison of a new integrated current source with the modified Howland circuit for EIT applications," *Physiol. Meas.*, vol. 30, no. 10, p. 999, 2009, doi: 10.1088/0967-3334/30/10/001.

[203] S.-J. Kweon, J.-H. Park, S. Shin, S.-S. Yoo, and H.-J. Yoo, "A reconfigurable time-to-digital converter based on time stretcher and chain-delay-line for electrical bioimpedance spectroscopy," in *Proc. IEEE 60th Int. Midwest Symp. Circuits Syst. (MWSCAS)*, Aug. 2017, pp. 1037–1040, doi: 10.1109/MWSCAS.2017.8053104.

[204] T. A. Chen, W. J. Wu, C. L. Wei, R. B. Darling, and B. D. Liu, "Novel 10-bit impedance-to-digital converter for electrochemical impedance spectroscopy measurements," *IEEE Trans. Biomed. Circuits Syst.*, vol. 11, no. 2, pp. 370–379, Apr. 2017, doi: 10.1109/TBCAS.2016.2592511.
[205] H. Huang and S. Palermo, "A TDC-based front-end for rapid impedance spectroscopy," in *Proc. IEEE 56th Int. Midwest Symp. Circuits Syst. (MWSCAS)*, Aug. 2013, pp. 169–172, doi: 10.1109/MWSCAS.2013.6674612.
[206] S. Shin, S.-J. Kweon, J.-H. Park, Y.-C. Choi, and H.-J. Yoo, "An efficient, wide range time-to-digital converter using cascaded time-interpolation stages for electrical impedance spectroscopy," in *Proc. IEEE Asia Pacific Conf. Circuits Syst. (APCCAS)*, Oct. 2016, pp. 425–428, doi: 10.1109/APCCAS.2016.7803993.
[207] Y. Yang, J. Wang, G. Yu, F. Niu, and P. He, "Design and preliminary evaluation of a portable device for the measurement of bioimpedance spectroscopy," *Physiol. Meas.*, vol. 27, no. 12, p. 1293, 2006, doi: 10.1088/0967-3334/27/12/004.
[208] R. Pallas-Areny and J. G. Webster, "Bioelectric impedance measurements using synchronous sampling," *IEEE Trans. Biomed. Eng.*, vol. 40, no. 8, pp. 824–829, Aug. 1993, doi: 10.1109/10.238468.
[209] H. Ko, T. Lee, J.-H. Kim, J.-A. Park, and J. P. Kim, "Ultralow-power bioimpedance IC with intermediate frequency shifting chopper," *IEEE Trans. Circuits Syst. II, Exp. Briefs*, vol. 63, no. 3, pp. 259–263, Mar. 2016, doi: 10.1109/TCSII.2015.2483258.
[210] G. Huertas, A. Maldonado, A. Yúfera, A. Rueda, and J. L. Huertas, "The bio-oscillator: A circuit for cell-culture assays," *IEEE Trans. Circuits Syst. II, Exp. Briefs*, vol. 62, no. 2, pp. 164–168, Feb. 2015, doi: 10.1109/TCSII.2014.2386233.
[211] P. Pérez *et al.*, "Sensing cell-culture assays with low-cost circuitry," *Sci. Rep.*, vol. 8, no. 1, pp. 1–11, Jun. 2018, doi: 10.1038/s41598-018-27295-3.
[212] A. Yúfera and A. Rueda, "Design of a CMOS closed-loop system with applications to bio-impedance measurements," *Microelectron. J.*, vol. 41, no. 4, pp. 231–239, Apr. 2010, doi: 10.1016/j.mejo.2010.02.006.
[213] Y. Liu, X. Qiao, G. Li, and L. Lin, "An improved device for bioimpedance deviation measurements based on 4-electrode half bridge," *Rev. Sci. Instrum.*, vol. 87, no. 10, Oct. 2016, Art. no. 105107, doi: 10.1063/1.4963658.
[214] N. Li, H. Xu, W. Wang, Z. Zhou, G. Qiao, and D. D.-U. Li, "A high-speed bioelectrical impedance spectroscopy system based on the digital auto-balancing bridge method," *Meas. Sci. Technol.*, vol. 24, no. 6, May 2013, Art. no. 065701, doi: 10.1088/0957-0233/24/6/065701.
[215] J. He, M. Wang, X. Li, G. Li, and L. Lin, "Pulse wave detection method based on the bio-impedance of the wrist," *Rev. Sci. Instrum.*, vol. 87, no. 5, May 2016, Art. no. 055001, doi: 10.1063/1.4947514.
[216] J. C. Baeg, H. Wi, T. In Oh, A. McEwan, and E. Je Woo, "An amplitude-to-time conversion technique suitable for multichannel data acquisition and bioimpedance imaging," *IEEE Trans. Biomed. Circuits Syst.*, vol. 7, no. 3, pp. 349–354, Jun. 2013, doi: 10.1109/TBCAS.2012.2212437.
[217] Y. Wu, D. Jiang, M. Habibollahi, N. Almarri, and A. Demosthenous, "Time stamp—A novel time-to-digital demodulation method for bioimpedance implant applications," *IEEE Trans. Biomed. Circuits Syst.*, vol. 14, no. 5, pp. 997–1007, Oct. 2020, doi: 10.1109/TBCAS.2020.3012057.
[218] N. Ivanisevic, S. Rodriguez, and A. Rusu, "Impedance spectroscopy based on linear system identification," *IEEE Trans. Biomed. Circuits Syst.*, vol. 13, no. 2, pp. 396–402, Apr. 2019, doi: 10.1109/TBCAS.2019.2900584.
[219] A. Sanchez-Gonzalez, N. Medrano, B. Calvo, and P. A. Martinez, "A multichannel FRA-based impedance spectrometry analyzer based on a low-cost multicore microcontroller," *Electronics*, vol. 8, no. 1, p. 38, Jan. 2019, doi: 10.3390/electronics8010038.
[220] R. Munjal, F. Wendler, and O. Kanoun, "Embedded wideband measurement system for fast impedance spectroscopy using undersampling," *IEEE Trans. Instrum. Meas.*, vol. 69, no. 6, pp. 3461–3469, Jun. 2020, doi: 10.1109/TIM.2019.2932177.
[221] N. Neshatvar, L. Regnacq, D. Jiang, Y. Wu, and A. Demosthenous, "Monitoring myocardial edema tissue with electrical impedance spectroscopy," in *Proc. IEEE Int. Symp. Circuits Syst. (ISCAS)*, Oct. 2020, pp. 1–4, doi: 10.1109/ISCAS45731.2020.9180610.
[222] P. Sysel and P. Rajmic, "Goertzel algorithm generalized to non-integer multiples of fundamental frequency," *Eurasip J. Adv. Signal Process.*, vol. 2012, no. 1, p. 56, Mar. 2012, doi: 10.1186/1687-6180-2012-56.
[223] L. Regnacq, Y. Wu, N. Neshatvar, D. Jiang, and A. Demosthenous, "A Goertzel filter-based system for fast simultaneous multi-frequency EIS," *IEEE Trans. Circuits Syst. II, Exp. Briefs*, vol. 68, no. 9, pp. 3133–3137, Sep. 2021, doi: 10.1109/TCSII.2021.3092069.
[224] F. Noveletto, P. Bertemes-Filho, and D. Dutra, "Analog front-end for the integrated circuit AD5933 used in electrical bioimpedance measurements," in *Proc. II Latin Amer. Conf. Bioimpedance*. Singapore, 2016, pp. 48–51, doi: 10.1007/978-981-287-928-8_13.
[225] C. Margo, J. Katrib, M. Nadi, and A. Rouane, "A four-electrode low frequency impedance spectroscopy measurement system using the AD5933 measurement chip," *Physiol. Meas.*, vol. 34, no. 4, p. 391, 2013, doi: 10.1088/0967-3334/34/4/391.
[226] F. Seoane, J. Ferreira, J. J. Sanchéz, and R. Bragós, "An analog front-end enables electrical impedance spectroscopy system on-chip for biomedical applications," *Physiolog. Meas.*, vol. 29, no. 6, pp. S267–S278, Jun. 2008, doi: 10.1088/0967-3334/29/6/S23.
[227] S. Dahlmanns, A. Wenzel, S. Leonhardt, and D. Teichmann, "Hardware setup for tetrapolar bioimpedance spectroscopy in bandages," in *Proc. 17th Int. Conf. Electr. Bioimpedance*. Singapore, 2020, pp. 18–24, doi: 10.1007/978-981-13-3498-6_3.
[228] B. Sanchez, A. Praveen, E. Bartolome, K. Soundarapandian, and R. Bragos, "Minimal implementation of an AFE4300-based spectrometer for electrical impedance spectroscopy measurements," *J. Phys., Conf. Ser.*, vol. 434, Apr. 2013, Art. no. 012014, doi: 10.1088/1742-6596/434/1/012014.

Panagiotis Kassanos (Senior Member, IEEE) was born in Athens, Greece, in 1983. He received the M.Eng. and Ph.D. degrees in electronic and electrical engineering from University College London (UCL), London, U.K., in 2006 and 2012, respectively.

From 2010 to 2011, he held a Postdoctoral EPSRC Ph.D. + Research Fellowship, and from 2011 to 2013, he was a Research Associate with the Analog and Biomedical Electronics Group, Department of Electronic and Electrical Engineering, UCL. Since 2014, he has been a Research Associate with The Hamlyn Centre, Institute of Global Health Innovation, Imperial College London, London. His current research interests include analog and mixed-signal integrated circuits for biomedical, sensor and signal processing applications, electrochemical sensors, embedded systems and instrumentation, microfluidics, sensor design and fabrication, flexible/stretchable electronics, low-cost additive fabrication techniques, and Raman spectroscopy for biosensing.

Dr. Kassanos is a member of the IEEE Circuits and Systems (CASS), Solid-State Circuits (SSCS), Instrumentation and Measurement (IMS), and Engineering in Medicine and Biology (EMBS) societies, a Topic Editor of *Sensors* (MDPI), and a Review Editor of *Frontiers in Electronics*: Wearable Electronics Section. He is a member of the Hellenic Society of Biomedical Technology and an active reviewer in many journals and conferences.